Universität Hamburg
DER FORSCHUNG | DER LEHRE | DER BILDUNG

Master's Thesis

Adiabatically Approximated Monopole Crystals

Ananta Effendie
Matr.-Nr.: 7144486
Submitted on the 30.11.2025
First Supervisor: Prof. Dr. Gudrid Moortgat-Pick
Second Supervisor: PD Dr. Ralf Hofmann

Abstract

According to an argument by Louis de Broglie which provides the basis for the formulation of wave mechanics of quantum objects by Schrödinger and Dirac, an electron is supposed to be treated as an emergent, thermodynamic phenomenon. A fundamental theory modeling spin-1/2 fermions in this way is provided by Yang-Mills thermodynamics. In it, the electron is described as a blob: a quantum mechanically and thermodynamically stable finite-volume droplet displaying the three phases of SU(2) Yang-Mills thermodynamics. Under extreme external conditions (number density and temperature), such extended systems are hypothesized to fuse into a large system with characteristic properties like evaporation time, transition time from an initially charged to a neutral system, and oscillatory excitations. The charge of a single electron is provided by an electric-magnetically dually interpreted BPS monopole with a radius of a size similar to the Compton wavelength and originating from the dissociation of a large-holonomy caloron in the creation of an electron-positron pair. This monopole is immersed into the deconfining-phase bulk of the blob of Bohr radius size. This thesis aims to define the principal behavior of low-particle number fused-electron droplets, as observable in a Penning trap using high-voltage and standard magnetic field strengths. For a first approximation, the size of such fused electron blobs is taken to be proportional to the Bohr radius a_0 and scaling with $N^{\frac{1}{3}}$. Given how these timescales develop with the particle numbers, it's expected that at macroscopic particle numbers, the processes defining the timescales can be regarded as independent of one another, hence justifying their adiabatic approximation. It's also expected that at particle numbers above Avogadro's number, timescales that are unobservable at particle numbers directly investigated in this thesis become observable, as the initially very brief evaporation time is approximated to increase fast enough to grow larger than the remaining timescales investigated here. Beyond naive extrapolations for the growth of the evaporation time, at larger particle numbers, there are far fewer electron-positron pairs at the fused droplet boundary, that can take part in the evaporation process.

Zusammenfassung

Gemäß einer Argumentation von Louis de Broglie, die die Basis für die Formulierung der Wellenmechanik von Quantenobjekten durch Schrödinger und Dirac bildet, müsste ein Elektron als ein emergentes thermodynamisches Phänomen betrachtet werden. Eine Theorie, die Spin-1/2-Fermionen auf diese Weise modelliert, ist die Yang-Mills-Thermodynamik. Das Elektron wird darin als ein quantenmechanisch und thermodynamisch stabiles System mit begrenztem Volumen, das die drei Phasen der SU(2)-Yang-Mills-Thermodynamik beinhält, modelliert. Dieses System wird als *Blob* bezeichnet. Unter extrem hoher Teilchendichte und Temperatur wird angenommen, dass solche ausgedehnten Systeme zu einem größeren System mit charakteristischen Eigenschaften wie Verdampfungszeit, Übergangszeit von einem elektrisch geladenen zu einem neutralen System und oszillatorischen Anregungen verschmelzen. Die Ladung eines einzelnen Elektrons ist in einem elektrisch-magnetisch dual interpretierten BPS-Monopol mit Compton-Wellenlängenradius im Blob lokalisiert, der aus der Dissoziation eines Kalorons mit großer Holonomie bei der Bildung eines Elektron-Positron-Paares entsteht. Diese Arbeit zielt darauf ab, das prinzipielle Verhalten von Ensembles verschmolzener Elektronen mit niedriger Teilchenzahl zu definieren, wie es in einer Penningfalle unter Verwendung von Hochspannung und Standardmagnetfeldstärke beobachtet werden kann. In erster Näherung wird die Größe solcher verschmolzener Elektronentröpchen als proportional zum Bohr radius a_0 und skalierend mit $N^{\frac{1}{3}}$ angenommen. Angesichts der Entwicklung dieser Zeitskalen mit den Teilchenzahlen ist zu erwarten, dass die Prozesse, die die Zeitskalen definieren, bei makroskopischen Teilchenzahlen als unabhängig voneinander betrachtet werden können, was ihre adiabatische Näherung rechtfertigt. Es wird außerdem erwartet, dass bei Teilchenzahlen oberhalb der Avogadro-Konstante Zeitskalen beobachtbar werden, die bei den in dieser Arbeit direkt untersuchten Teilchenzahlen nicht beobachtbar sind, da die anfänglich sehr kurze Verdampfungszeit voraussichtlich schnell genug ansteigt, um die übrigen hier untersuchten Zeitskalen zu überschreiten. Über naive Extrapolationen für das Wachstum der Verdampfungszeit hinaus gibt es bei höheren Teilchenzahlen weitaus weniger Elektron-Positron-Paare an der Grenze des verschmolzenen Blobs, die zur Verdampfung beitragen können.

Contents

1

Introduction

The standard model description of the electron, while one of the most fundamental and commonly used definitions in physics, is at the root of several open problems in modern physics, and hence seems to be incomplete. Furthermore, the standard model describes the electron and its electroweak interactions using two dimensionless fit-parameters. The Weinberg angle θ_W, for example, has been determined empirically, but there is no theoretical reasoning as to how its value of approximately 30° emerges from physical properties of the electron. Similarly, despite its central role in understanding one of the fundamental forces of the standard model, the fine-structure constant $\alpha = \frac{1}{137}$, is a fit parameter without any theoretical derivation. As such, some characteristics of the electron should be expected to not have been captured by the standard model description, and as a consequence, several attempts to gain a deeper understanding of the electron outside the standard model have emerged.

1.1. Electrons as Emergent Thermodynamic Phenomena

The concept of matter waves for quantum objects as formulated by de Broglie is widely applied across disciplines in physics and forms the basis for quantum physics as a strictly quantitative science, though it includes a theoretical detail that is often overlooked in the description of electrons. It describes the electron as an emergent thermodynamic phenomenon by defining an internal heat. The description follows directly from the observation that when heat is imparted onto an object, and that object's kinetic energy is not changed by this, then its mass has to be altered instead, as a mathematical necessity ([**11**], Chapter II, section 7).

A shortened version of de Broglie's argument begins with the well-known descriptions of quantum objects as plane-wave functions and the relativistic mass-energy relation, where

the particle is considered an extended object. At rest the electron is described as an extended object with a clock frequency ν_0 and uniform oscillation amplitude Φ.

While de Broglie did not further describe the source of the oscillation, its inclusion would later prove to be in line with the description of quantum particles as described by solutions of the Schrödinger equation, which tends to include a periodic component $e^{-\frac{iE_n t}{\hbar}}$, where the (quantized) energy E_n is considered to be fully expressible through a wave frequency $E_n = \hbar\nu$. In this consideration however, de Broglie only presupposes this clock-frequency and relates it to the electron's mass through what would be later be considered its ground state energy.

At this point, the theory is not quantized, so this defines a theoretical minimum for the rest energy of the electron on a continuous spectrum:

$$\Phi = a_0 \sin(2\pi\nu_0 t_0), \tag{1.1}$$

$$m_0 c^2 = h\nu_0. \tag{1.2}$$

The frequency ν_0 alone determines the quantum oscillation energy, which is set equal to the rest energy. In this particular definition, the propagation characteristics of the de Broglie matter wave are defined through their change under a Lorentz boost. When a Lorentz boost is applied in the z-direction, the system undergoes the typical time-dilation in line with special relativity, and the spatially flat oscillation is transformed into a wave propagating along the z-direction

$$\beta = \frac{v}{c} \Rightarrow t_0 = \frac{t - \frac{\beta}{c} z}{\sqrt{1-\beta^2}}. \tag{1.3}$$

As the effectively uniform wave of the particle at rest is moved through space by the Lorentz boost, the wave distribution experiences a contraction of space and the clock frequency is shifted as

$$\nu = \frac{\nu_0}{\sqrt{1-\beta^2}}. \tag{1.4}$$

Further, the boosted electron gains a phase-velocity $v_p = \frac{c}{\beta}$ as it is now a propagating wave. The introduction of a phase velocity also enables a definition for the wavelength for this

propagating wave. This is the common conception of the electron as a matter wave:

$$\lambda = \frac{v_p}{\nu} = \frac{c\sqrt{1-\beta^2}}{\nu_0 \beta}. \tag{1.5}$$

The momentum of the moving electron $p = m_0 \frac{v}{\sqrt{1-\beta}}$ is generated by the Lorentz boost via the propagation velocity v. The rest-mass energy of the electron $m_0 c^2 = h\nu_0$ can be used to relate the momentum with the de Broglie-wavelength λ:

$$\frac{p}{h} = \frac{m_0 v}{h\sqrt{1-\beta^2}} \tag{1.6}$$

$$= \frac{h\nu_0 v}{c^2 h\sqrt{1-\beta^2}} \tag{1.7}$$

$$= \frac{\nu_0}{\sqrt{1-\beta^2}} \frac{v}{c^2} \tag{1.8}$$

$$= \frac{\nu_0 \beta}{c\sqrt{1-\beta^2}} = \lambda^{-1}. \tag{1.9}$$

Temperature's effect on the wavelength of an isolated particle utilizes the constancy of entropy over a closed thermodynamic system. In thermodynamics, entropy of a macroscopic state is proportional to the logarithm of the number of complexions that can realize that state, so it's expressed through a number. As a consequence, the entropy is relativistically invariant. It's considered the fundamental invariant of thermodynamics. For a body with initial proper mass M_0, temperature T_0, and a velocity $v = \beta c$, observed from a Galilean reference system, in which a heat source provides heat Q to the object, while the body is expected to keep its velocity. Its energy is expected to increase as a result of the heat. To conserve the total energy of the particle under the change of its internal heat, some work A needs to act on the object. Given the transformation law of the frequency $\nu = \frac{\nu_0}{\sqrt{1-\beta^2}}$, and the energy formula (Equation 1.11), the proper mass must transform accordingly as $M = \frac{M_0}{\sqrt{1-\frac{v^2}{c^2}}}$. The flux in kinetic energy must be equal to the internal heat, modified by A:

$$E_{kin} = \frac{Mc^2}{\sqrt{1-\beta^2}} = \frac{(M_0 + \Delta M)c^2}{\sqrt{1-\beta^2}}, \tag{1.10}$$

$$\frac{\Delta M c^2}{\sqrt{1-\beta^2}} = Q + A. \tag{1.11}$$

A force F needs to act on the body to impart A. The derivative of the momentum with respect to time is equal to this force, as well as the fraction $\frac{A}{v}$. In Equation 1.13, the particle's velocity is assumed constant, so the only quantity that varies with time is the proper mass.

$$\frac{(M_0 + \Delta M)v}{\sqrt{1-\beta^2}} - \frac{M_0 v}{\sqrt{1-\beta^2}} = \int F dt = \frac{1}{v}\int F v dt = \frac{A}{v}, \tag{1.12}$$

$$\Rightarrow A = \int F v dt = \frac{\Delta M}{\sqrt{1-\beta^2}} v^2. \tag{1.13}$$

The external work acting on the particle can be expressed exclusively using the temperature,

$$Q + A = \frac{\Delta M}{\sqrt{1-\beta^2}} c^2, \tag{1.14}$$

$$\frac{\Delta M}{\sqrt{1-\beta^2}} = \frac{A}{v^2}, \tag{1.15}$$

$$\Rightarrow Q + A = A\frac{c^2}{v^2}, \tag{1.16}$$

$$\Rightarrow Q = \left(\frac{c^2}{v^2} - 1\right) A = \frac{1-\beta^2}{\beta^2} A. \tag{1.17}$$

Because the geometry of the object is invariant with respect to the heat-input from the reference system, and assuming, without loss of generality, that the change of heat does not change its motion, it must instead facilitate the change of the object's proper mass, so that $\frac{Q_0}{c^2} = \Delta M$, where Q_0 is the heat imparted to the object from the reference system. Expressing the change of proper mass through the total heat of the object defines the behavior of the its internal heat under the Lorentz Boost

$$\frac{Q_0}{c^2} = \Delta M = \frac{1}{\sqrt{1-\beta^2}} \frac{Q}{c^2}, \tag{1.18}$$

$$\Rightarrow Q_0 = \frac{Q}{\sqrt{1-\beta^2}}, \tag{1.19}$$

$$\Rightarrow Q = \sqrt{1-\beta^2} Q_0. \tag{1.20}$$

Given the definition of the change in entropy dS as the differential of heat δQ over the system

temperature T, this relation, along with the invariance of entropy, implies that the temperature transforms according to $T = T_0\sqrt{1-\beta^2}$, the same way as the heat. Notably, de Broglie's construction also applies this to isolated particles, though this concept is contingent on a relation from relativistic thermodynamics, which states that given a variable proper mass, the internal heat differential is balanced by the differential of the Lagrangian $\delta Q = -\delta_M \mathcal{L}$. The notion of an *internal heat* of the electron is incompatible with the point-particle character of an elementary particle. Because the electron is now considered to have a temperature T as an isolated particle, its thermal energy must be related to its rest mass energy and has to transform like the rest mass energy does under the Lorentz boost $kT = m_0c^2\sqrt{1-\beta^2}$. Since the rest mass energy is also equal to $h\nu$, this thermal energy has the same relativistic covariance as the temperature does.

The implication of this change in temperature under Lorentz boosts coincides with the intuition for temperatures for ensembles under Lorentz boosts. If a thermodynamic ensemble is boosted in the z-direction, all its particles gain a bias toward the z-direction. This reduces the entropy of the particles in an external reference system, and as a result the ensemble is less thermalized than it would be at rest. Because entropy is a fundamental invariant of thermodynamics, this must also be true in the boosted rest system.

The thermodynamics of the isolated electron implies an entropy, which derives from the idea of a fluctuating proper mass M, and the flux of total entropy being contingent only on the proper mass. The variable component of entropy is considered to be a very small part of the full entropy of a single particle. Using the expression for the change of entropy from thermodynamics $dS = \frac{\delta Q}{T}$, the entropy fluctuation with respect to the proper mass allows for a first order proper mass approximation of the Lagrangian. The Lagrangian is obtained from the relation of the internal heat and the external work in Equation 1.17

$$A = \frac{\Delta M_0}{\sqrt{1-\beta^2}}v^2 = \frac{\beta^2}{1-\beta^2}Q, \tag{1.21}$$

and the definition of classical mechanics for the Lagrangian, using the energy $W = \sum p_i\dot{q}_i - \mathcal{L}$ where p_i and $\dot{q}_i$ are the generalized coordinates. Because for the object in question, the velocity had been set as constant, $\dot{q}_i$ are also constant. Because the change in momentum originates in the change of the work acting on the object, $dA = \sum \dot{q}_i dp_i = \sum \dot{p}_i dq_i$, so the energy differential is made up of the sum of A and Q

$$dW = \sum_i \dot{q}_i dp_i - d\mathcal{L} \tag{1.22}$$

$$= A - d\mathcal{L}, \tag{1.23}$$

$$\Rightarrow \Delta W = A - \Delta\mathcal{L} \tag{1.24}$$

$$= A + Q. \tag{1.25}$$

This implies that $\Delta\mathcal{L} = Q$. Assuming only those effects that change M factor into $\Delta\mathcal{L}$ for this process, Equation 1.21 implies

$$\frac{\Delta M_0}{\sqrt{1-\beta^2}} v^2 = -\frac{\beta^2}{1-\beta^2}\Delta\mathcal{L}, \tag{1.26}$$

$$\Rightarrow \Delta\mathcal{L} = -\frac{v^2 \Delta M_0 \sqrt{1-\beta^2}}{\beta^2}, \tag{1.27}$$

$$= -c^2 \Delta M_0 \sqrt{1-\beta^2}. \tag{1.28}$$

For this purpose, further terms beyond the first order don't rely on M and can be omitted. Fluctuation of entropy from a single particle is defined to correlate with heat dissipation, which sets the sign. This defines the behavior of a singular particle's entropy

$$\delta_M S = \delta_M (S_0 + S(M)) = -\frac{\delta Q}{T} = \frac{\delta_{M_0}\mathcal{L}}{T}, \tag{1.29}$$

$$\Rightarrow \delta S(M) = -\frac{Mc^2\sqrt{1-\beta^2}}{T} = -\frac{Mc^2\sqrt{1-\beta^2}}{\frac{m_0 c^2\sqrt{1-\beta^2}}{k}} \tag{1.30}$$

$$= -k\frac{\delta_M M}{m_0}, \tag{1.31}$$

$$\Rightarrow S = S_0 - k\frac{M}{m_0}. \tag{1.32}$$

This, along with the energy equation $kT = h\nu_c$, constitute the fundamental formulas of the thermodynamics of the isolated particle, which can be applied in all Galilean reference systems [**11**]. The relativistic effect of the thermodynamics of a single particle is not accounted for within the standard model of particle physics.

1.2. The Electron as a Soliton Solution in Quantum Mechanics

In quantum mechanics the electron is typically described by the probability amplitude of the wave function that solves the Schrödinger equation (or Dirac equation for spin-1/2 particles). In general, these solutions describe localized wave packets that disperse as they propagate. They can be superimposed to construct solitonic wave functions. Solitons often consist of a high-frequency excitation in space, with an overall, larger wavelength envelope. When such solitons interact, they can experience a phase shift, but remain otherwise unchanged. In this way, they fit the macroscopic description of localized particles with some spatial geometry while retaining the quantum particle's wave characteristics.

A different approach is described through a classical theory adjusting for the 4/3-problem directly [**12**]. The discrepancy between Maxwellian electrodynamics and the classical interpretation of the elementary character of the electron is known as the *4/3 problem*. In it, a sharp distinction is made between the dynamics of the electron, and its particle/field interaction. Special relativity sees particle mass increasing with velocity. Its formalism treats the 4-momentum of a field distribution as Lorentz-covariant, though this formalism can't describe the process by which electrons move in a stationary three-dimensional Euclidean reference system through the effects of electric fields alone. An analytic equilibrium condition requires that the first variation of the potential energy integral V has to vanish for all valid spatial variations. This is described in full in [**17**]. The instability of the solutions for the rest particle equation of the classical electron, even affects how the electron's field behaves under constant motion as a consequence.

To see this, first, the reference system is chosen arbitrarily. Continuous spatial translation and rotation symmetry assumes that this must be possible to describe the mechanics of point particles. In the field description of the electron, its energy-momentum distribution transforms along with the Lorentz boost as it moves at some speed $\vec{v} = c\vec{\beta}$.

Assume an electron moving in a reference system Σ with pre-transformation coordinates $x_0 = (ct_0, \vec{r}_0)$ in the electron's rest frame Σ_0. Transforming to Σ and using the abbreviation taken from special relativity $\gamma = \frac{1}{\sqrt{1-\beta^2}}$, the coordinates transform with $\vec{\beta}$

$$ct_0 = \gamma ct - \gamma\vec{\beta}\vec{r}, \tag{1.33}$$

$$\vec{r}_0 = \gamma\vec{r}_{\parallel} + \vec{r}_{\perp} - \gamma\vec{\beta}ct. \tag{1.34}$$

Instead of the electric field of a point charge e according to Gauss' law, a regularized electric field strength $\vec{E}(0)$ for a resting electron as a homogeneously charged sphere with radius r_0 would not include a discontinuity in the density of an extended charge distribution

$$\vec{E}(0) = \frac{e}{4\pi\varepsilon_0}\frac{\hat{e}_r}{r^2 + r_0^2}. \tag{1.35}$$

Assuming the reference system is at rest, the energy density contributions of an electromagnetic field $\mathcal{E}(\vec{r}) = \frac{\varepsilon_0}{2}(\vec{E}^2(0)+\vec{B}^2(0))$ is finite everywhere. For an electron at rest, the magnetic field contribution vanishes. The exact definition of the energy density is taken directly from the 00-element of the symmetric energy-momentum tensor $\Theta^{\mu\nu} = -\frac{1}{\mu_0}\eta^{\mu\kappa}F_{\kappa\lambda}F^{\nu\lambda} + \frac{1}{4\mu_0}\eta^{\mu\nu}F_{\kappa\lambda}F^{\kappa\lambda}$. The self-energy $E_e(0)$ is a straightforward integral of the energy density over the entire 3-dimensional space

$$E_e(0) = 4\pi\int_0^\infty r^2\mathcal{E}_0(\vec{r})dr \stackrel{!}{=} m_0c^2. \tag{1.36}$$

Under Lorentz-transformation, the fields composing the field strength tensor $F^{\mu\nu}$ transform as:

$$\vec{E}(\vec{\beta}) = \frac{\vec{\beta}(\vec{\beta}\vec{E(0)})}{\beta^2} + \gamma(\vec{E}(0) - \frac{\vec{\beta}(\vec{\beta}\vec{E(0)})}{\beta^2}), \tag{1.37}$$

$$c\vec{B}(\vec{\beta}) = \gamma\vec{\beta}\times\vec{E}(0). \tag{1.38}$$

To obtain the total energy of a moving classical electron, the energy density needs to be transformed from Σ_0 to Σ. The motion will induce non-zero magnetic-field contributions to the energy density. The behavior under that transformation can be determined by enumerating the contributions of each field component. The parallel component of the electric field contributes with exactly one count of the energy density of the electron at rest. The orthogonal electric field components contribute with $\frac{\gamma^2}{3}$. The parallel contribution of the magnetic field vanishes, and the two orthogonal magnetic field components contribute with $\frac{\gamma^2\beta^2}{3}$. Due to the spherical symmetry of the field, the electric field components contribute with equal parts to the density, which introduces the factor $\frac{1}{3}$ to the integrand of the total energy. Note σ as the spherical coordinates of Σ ([**12**], section B)

$$E_e(\beta) = \int_\Sigma d^3\sigma \mathcal{E}_{\vec{\beta}}(\vec{r}) \tag{1.39}$$

$$= \int_\Sigma d^3\sigma \frac{\mathcal{E}_0(\vec{r}_0)}{3}(1 + 2\gamma^2 + 0 + 2\gamma^2\beta^2) \tag{1.40}$$

$$\approx \int_\Sigma d^3\sigma \frac{\mathcal{E}_0(\vec{r}_0)}{3}(1 + 2\gamma^2 + 0 + 2(\gamma^2 - 1)) \tag{1.41}$$

$$= \int_\Sigma d^3\sigma \frac{\mathcal{E}_0(\vec{r}_0)}{3}(4\gamma^2 - 1) \tag{1.42}$$

$$= E_e(0)\frac{4\gamma^2 - 1}{3\gamma}. \tag{1.43}$$

This is only correct, given $\gamma = 1$, meaning for the electron at rest, but as its velocity increases, and thus γ increases, the energy tends toward $\frac{4}{3}$ of the classically expected value $\gamma E_e(0)$. Due to the added contribution's constancy under Lorentz indices, it has to be a potential energy contribution. At a high-level inspection, whereas a naive point-particle description sees (isolated) electrons as localized in a small volume with quantized charge and a field extending to infinity, this approach would remove the massive point-particle character of the electron, instead describing them as purely electromagnetic phenomena, through which their dynamics are describable by up to 3 field degrees of freedom.

To address this discrepancy, in [**30**] a model for the electron derived from a 3-dimensional generalization of the Sine-Gordon model, similar to the Wu-Yang description of Dirac monopoles is proposed. These are stable, solitonic solutions of a Lagrangian constructed on a curved background, and extended by a stabilizing potential term.

1.3. Yang-Mills Thermodynamics

In Yang-Mills Thermodynamics, massive spin-1/2 fermions are emergent phenomena whose behavior is primarily determined by their internal temperature. The changes in behavior can be charted across the spectrum of their dimensionless temperature λ. Each particle species has an associated Yang-Mills scale Λ, emerging from its gauge group, by which the specific temperatures can be derived. The conversion between the dimensionless temperature λ and the temperature in eV T is $\lambda = \frac{2\pi T}{\Lambda}$. In this thesis, all values for T are taken with the Yang-Mills scale for electrons $\Lambda_e = 3.6$ keV in mind. The electron itself is described as a vibrating magnetic monopole (interpreted dually as an electric monopole) that carries the electron's charge and mass, enclosed within a thick boundary shell that comprises the bulk of the volume of the electron. This *blob* containing the monopole exists at the self-intersection

point of a thin center vortex loop.

In low energy density environments below $\lambda = 11.57$ ($T = 6.6$ keV), they consist of thin center-vortex loops, with a self-intersection. Other particle species, the electron-neutrinos, for example, are simple loops without any self-intersection. In their ground state, all these center-vortex loops have no self-intersection. When enough energy is invested into such a center-vortex loop, they can gain a self-intersection, which then balloons into a volume experiencing all three phases of Yang-Mills thermodynamics. Both loops of the center-vortex loop remain attached to this volume, and they can orient freely around it. Due to the flow of monopoles within the center-vortex loop, a particle's spin and hence its magnetic characteristics are influenced by their position around the blob volume. The center-vortex loop itself is nearly massless, and only by twisting it until self-intersections occur does an associated particle gain the majority of its mass ([**21**], Section 7, Introduction). The structure of a single self-intersection of a center-vortex loop comprises the volume of the electron blob (Figure 2.1). Monopoles can't exist in confined phase, and as they approach the phase boundary, they experience renormalization of their magnetic coupling by adjacent calorons with small holonomies and Yukawa screening by stable monopoles liberated by the dissociation of adjacent large-holonomy calorons, rendering their charge unobservable from outside the blob ([**21**], Section 5.4).

Between $\lambda_c = 13.87$ ($T_c = 8$ keV) and $\lambda = 11.57 = 0.83\lambda_c$ ($T = 6.6$ keV) lies the preconfined phase, in which the center-vortex loops transition into a dense packing of magnetic (anti-)monopoles, which are collectively described through another complex scalar field. λ_c is considered the *critical temperature*.

The thermal ground state in preconfining phase associates with configurations of massless magnetic monopoles and anti-monopoles. Their dense packing is expressed through a complex scalar field, breaking the remaining U(1) gauge symmetry ([**1**], section 2.2).

At above the critical temperature of $\lambda_c = 13.87$ ($T_c \approx 8$ keV) lies the deconfined phase, in which the particles are described through (anti-)calorons, coarse-grained over a 3-dimensional sphere in singular gauge, with some a topological charge of ±1 at their center [**27**]. (Anti-)calorons are (anti-)self-dual solutions of the fundamental Yang-Mills equation on the Euclidean cylinder the gauge-field configuration which are without pressure or energy density, and hence can't propagate. In this phase, the (anti-)calorons are packed densely enough for the (anti-)caloron peripheries to overlap with neighboring (anti-)caloron centers ([**1**], Section 2.1, [**27**]). The contributions of nontrivial holonomy (anti-)calorons are ignored for a priori ground-state estimates, because they are not stable under one-loop quantum fluctuations [**27**], and their

suppression at large volumes ([**21**], section 5.1.5 and 5.4.2). Their contributions are instead described by effective radiative corrections to the a priori ground-state estimate. The negative ground-state pressure is explained by the BPS magnetic monopoles of the small-holonomy (anti-)calorons attract one another ([**21**], section 4.4.2). The dense packing leads to an adjoint scalar field, which breaks the fundamental SU(2)-gauge symmetry down to U(1). The effects of peripheries overlapping with neighboring caloron centers are described by pure-gauge solutions to the effective Yang-Mills equation. The monopoles and antimonopoles become massless, pointlike and densely packed, creating a condensate with a high conductivity. The conductivity is limited by phase mixing effects.

Within the blob comprising the electron, a mixture of all phases occur within a spatial volume inside a thick boundary shell (Figure 2.1, [**1**]).

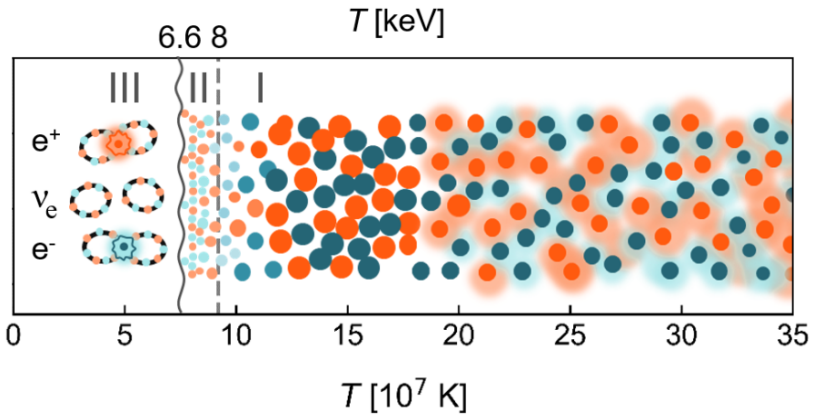

Figure 1.1: *An illustration of the phases for electrons and their neutrinos, using Λ_e in YM-Thermodynamics as seen in [**1**], Figure 1*
At low temperatures of up to 6.6 keV *(left), the massless, metastable soliton solutions in confined phase reduce to thin center vortex loops. The self-intersections cause unstable defects. The ground states of the solitons (degenerate to Z_2) confine fundamental test charges. The mass of the center vortex loops is determined by their holonomy, but due to the screening effects in confined phase, they don't appear as propagating excitations in effective theories.*
In the preconfined phase between 6.6 keV *and* 8 keV *(center), the pressure is negative, and the resulting thermodynamics are ground state dominated [**27**]. The solitons take on the characteristics of point particles, and through their dense packing create a condensate comprised of massless monopoles and antimonopoles. They can be collectively described using a complex scalar field, which breaks the remaining U(1)-gauge symmetry. The overlap of all peripheries between the (anti-)monopoles are described by an effective pure gauge configuration. Electric conductance in this phase is high, compared to the other phases. Beyond a critical temperature of T_c = 8 keV (right), the particles enter deconfining phase, where the ground state pressure is negative. The a priori estimate of the thermal ground state in terms of an inert, adjoint scalar field ϕ is obtained by a spatial coarse-graining over the center of a trivial-holonomy (Harrington-Shepard) caloron and its anticaloron. At trivial-holonomy the (anti-)caloron is stable under one-loop quantum fluctuations.*

Yang-Mills Thermodynamics proposes a model for particles, including, but not limited to the electron, whose behavior changes depending on the energy density in the background. At rest, it posits electrons as a blob of vanishing pressure with a radius of length scales

similar to the Bohr radius, trapping a charged BPS monopole at temperature $T_0 = 7.95$ keV. This spectrum is sketched in Figure 1.1. Its construction allows for derivations of so far unexplained constant definitions of the fine-structure constant, and the Weinberg mixing angle. The bulk thermodynamics of electrons constructed in this way are established by using a mix of two distinct SU(2) gauge theories associated with the cosmic microwave background (CMB) and the electron.

The standard model computes the weak mixing angle θ_W at some 4-momentum transfer, when measured at another 4-momentum transfer. The running of θ_W with four-momentum transfer thus is given by the running of the two couplings of the weak isospin g and the weak hypercharge g'. They define $\cos\theta_W = \frac{g}{\sqrt{g^2+g'^2}}$, $\sin\theta_W = \frac{g'}{\sqrt{g^2+g'^2}}$. These quantities are defined through the gauge-group couplings of $SU(2)_L$ and $U(1)_\gamma$. θ_W must satisfy

$$\begin{bmatrix} \gamma \\ Z^0 \end{bmatrix} = \begin{bmatrix} \cos\theta_W & \sin\theta_W \\ -\sin\theta_W & \cos\theta_W \end{bmatrix} \begin{bmatrix} B^0 \\ W^0 \end{bmatrix}. \tag{1.44}$$

in which γ is the photon field contribution, and Z^0, W^0, B^0 are the Z-, W- and B bosons respectively. The boson field contributions are neutral gauge fields. B^0 is the gauge field of $U(1)_Y$, W^0 the gauge field of cartan(SU(2)), and Z^0 the (massive) mixture of them).

In SU(2) Yang-Mills thermodynamics, θ_W at zero 4-momentum transfer is computable by considering the bulk pressure with the mixing effects for the two applicable gauge groups, and above the critical temperature of the transition into the deconfining phase. To one-loop accuracy, write the bulk pressure as a weighted sum of pressures in deconfining $SU(2)_e$ and $SU(2)_{CMB}$.

$$P_{bulk}(T) = (1 - \sin^2\theta_W(T))P_e(T) + \sin^2\theta_W(T)P_{CMB}(T). \tag{1.45}$$

When assuming that the stabilizing temperature is known, then Equation 1.45 can be set to 0. The mixed gauge charge field-coupling stand in relation directly defined by θ_W, and evaluating the charges at stabilizing temperature then provide a way to determine the value of the sin and cos terms. The relation is determined at the (dimensionless) stabilizing temperature λ_0. Using the ratio $\kappa = \frac{\Lambda_{CMB}}{\Lambda_e}$, the coupling $e(\kappa^{-1}\lambda_0)$ evaluates to about $\sqrt{8}\pi$. The mean radial position is

the normed sum over the probability densities equal to $\frac{3r^2}{4\pi r_0^3}\sin\theta, 0 \leq r \leq r_0, 0 \leq \theta < \pi$. As a consequence, extrapolated to 3 dimensions, the charge coupling carries a factor of $\frac{27}{64} = \left(\frac{3}{4}\right)^3$.

$$q = -\frac{27}{64}\frac{4\pi}{e(\lambda_0)}\cos\theta_W(\lambda_0), \tag{1.46}$$

$$q_{CMB}(\lambda_0)\sin\theta_W(\lambda_0) = \frac{4\pi}{e(\kappa^{-1}\lambda_0)}\sin\theta_W(\lambda_0), \tag{1.47}$$

$$q_e(\lambda_0)\cos\theta_W(\lambda_0) = \frac{4\pi}{e(\lambda_0)}\cos\theta_W(\lambda_0), \tag{1.48}$$

$$q_{CMB}(\lambda_0)\sin\theta_W(\lambda_0) = q_e(\lambda_0)\cos\theta_W(\lambda_0). \tag{1.49}$$

Using $q_{CMB} \approx \sqrt{2}$ and $q_e =$, then $\tan\theta_W(\lambda_0) = \frac{\sin\theta_W}{\cos\theta_W} \approx \frac{\sqrt{8}}{e(\lambda_0)}$. and Equation 1.45 evaluates to

$$0 = P_{bulk}(\lambda_0) \approx (1 - \frac{8\pi^2}{e^2(\lambda_0) + 8\pi^2})P_e(\lambda_0) + \frac{8\pi^2}{e^2(\lambda_0) + 8\pi^2}P_{CMB}(\lambda_0). \tag{1.50}$$

Both λ_0 and the coupling at λ_0 can be determined numerically by appeal to thermodynamical self-consistency of the quasiparticle expressions for pressure, energy density, and the contributions of the thermal ground state. Once these have been identified to $\lambda_0 = 16.3$ and $e(\lambda_0) = 14.88$, the Weinberg angle can be solved for using $\theta_W(\lambda_0) = \arctan(\frac{\sqrt{8}\pi}{e(\lambda_0)})$. The dimensionless stabilizing temperature λ_0 describes the point at which the system exhibits no 4-momentum. At this point, θ_W evaluates to the familiar 30.84°. This is quite close to values of θ_W determined experimentally at finite four-momentum transfer [**1**].

The fine-structure constant is defined as $\alpha = \frac{q^2}{4\pi}$, and using Equation 1.49, a first approximation can be expressed using λ_0 and θ_W. The deviation is due to the missing mixing effects within $SU(2)_e$.

The goal of this thesis is to model the generalization of the quantum-mechanical single-particle soliton. This works toward the conception of the electron as an emergent thermodynamic phenomenon as described by Yang-Mills Thermodynamics. When given a configuration of fused electrons, several characteristic timescales emerge from different aspects of the system, and predictions are suggested by extrapolating to dramatically higher particle numbers than can be explicitly calculated within the scope of this work.

The fusion of electrons is dependent on sufficiently high electron-density and energy den-

sity associated with the stabilizing temperature T_0. These energy densities have become experimentally feasible using an experiment featuring layered parallel nanowire wafers, energetically pumped by high-energy laserpulses [**15**]. The dynamics of the plasma-like monopole-crystal are studied under consideration of contemporary experimental constraints up to the creation and diagnosis of the monopole crystal.

2

The Basic Thermodynamic Construction of Electrons in Yang-Mills Thermodynamics

2.1. Electrons in Yang-Mills Thermodynamics

Electrons in Yang-Mills Thermodynamics are solitonic solutions emerging from SU(2) Yang-Mills thermodynamics. An isolated electron can be thought of as a 3-dimensional spherical volume in space, containing an isolated BPS monopole in its bulk. In general, such blobs are not stable, as the bulk pressure drives the monopoles into the center of the blob. At some stabilizing temperature T_0, the effects of the negative bulk pressure and excitation driving the monopole toward the periphery cancel, and the pressure vanishes. The blob's geometry exhibits the three phases of SU(2) Yang-Mills Thermodynamics. In the bulk's center, the deconfining phase prevails, supporting a finite-size and finite-charge BPS monopole. The full blob formed at the point of self-interaction is a 3-sphere with a radius of about the Bohr radius a_0, while the monopole within it is a particle of finite extent with a radius of the reduced Compton wavelength r_c. This construction would justify how photons of different wavelengths scatter on electrons. It only requires that photons interact with objects of a size similar to their own wavelength. Photons with the wavelength of the Bohr radius shake the entire electron blob and scatter elastically in line with Thomson scattering. At Compton wavelength, the photon instead penetrates the blob and scatters directly on the monopole, and the scattering process has to include the caloron-quantum effects.

For the mixed $SU(2)_{CMB} \times SU(2)_e$, r_c is approximately 88.3 times smaller than the radius of the electron at rest. If it moves into the peripheral region of the blob, near the boundary,

it moves into the preconfining phase. The monopole cannot exist in confining phase. A monopole's mass and charge is screened out as it approaches the boundary shell. The thick boundary shell of the blob is connected to both ends of center-vortex lines (Figure 2.1), which induce the collective magnetic moment, so that the figure-eight figure of the charged monopoles for a particle species in the confined phase emerges.

Due to the small scales of the quantities that are investigated in this thesis, most computations are done in natural units. The results are presented in SI units as well as natural units where appropriate.

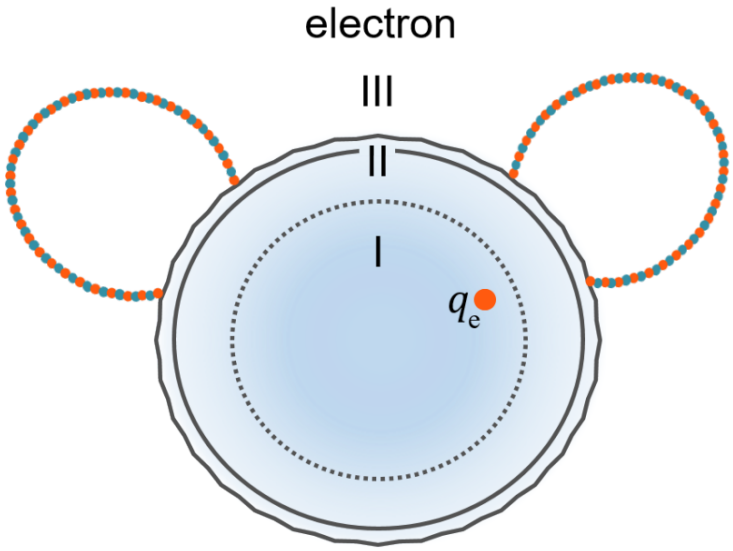

Figure 2.1: *An illustration of the electron as a blob containing a charge-carrying monopole sourced from* **[1]**, *Figure 3 The disparate phases are labeled as the deconfining phase (I), preconfining phase (II), and confining phase (III). The blob of the thick boundary shell for the monopole (red) is located at the self-intersection point of a thin center vortex loop that forms a figure eight. When such a self-intersection occurs, an isolated (anti-)monopole is created, and the blob forms around it. The deconfining phase at the center of the blob is considered to be at stabilizing temperature T_0, so the pressure in the bulk of the blob is vanishing. In fact, the pressure is vanishing, and the conductance is high on the preconfined surface of the blob. The monopole can move freely within the blob. It has a breathing frequency equal to m_e* **[29]**.

The critical temperature is dependent on the mass of the soliton. For a monopole emitted during the dissociation of a maximum holonomy at stabilizing temperature T_0, the electron radius r_0, the coupling is dependent on the dimensionless stabilizing temperature $e(\lambda_{0,e} = 16.3 = 1.18\lambda_{c,e}) = 14.88$. e is the running effective gauge coupling in the deconfined phase as a function of λ.

This coupling, along with the modulus of the (anti-)caloron gauge field component $H_\infty(T_0) = \pi T_0$, fully characterizes the vector mode in the adjoint Higgs model, associated with a

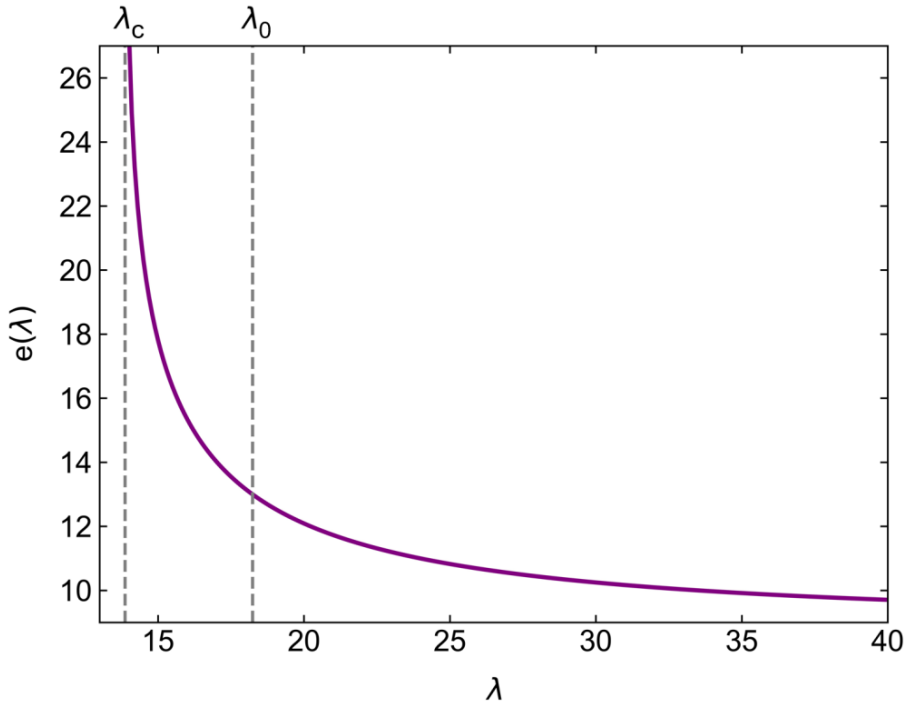

Figure 2.2: *The running coupling $e(\lambda)$ as computed and depicted in [**1**], Figure 2. It marks specifically the critical temperature $\lambda_c = 13.87$ at which the deconfining phase begins, and the stabilizing temperature $\lambda_0 = 18.31$ at which the pressure in deconfining phase vanishes. There is a difference in these values compared to $\lambda_{0,e}$ and $\lambda_{c,e}$ due to mixing effects with cosmic microwave background radiation that the Yang-Mills thermodynamics for electrons experiences.*

nontrivial-holonomy caloron. $m_e = e(\lambda_{0,e})H_\infty(T_0)$ is the mass of the electron's vector mode, and coincides with the lowest-frequency breathing mode of the monopole in $SU(2)_e$ **[22]**. To consider mixing effects of $SU(2)_{CMB}\times SU(2)_e$, this relation is generalized to

$$\frac{m_e}{H_\infty(T_0)} = e(\lambda_0)\cos\theta_W + e(\frac{\Lambda_e}{\Lambda_{CMB}}\lambda_0)\sin\theta_W. \tag{2.1}$$

The parameters that are required in this thesis are the coupling at the stabilizing temperature λ_0, and λ_0 itself. When set to the appropriate values, they characterize a stable state of the blob. From now on, they are assumed to be known constants.

$$e(\lambda_0) = 14.88, \tag{2.2}$$
$$T_c = 7.95 \text{ keV}, \tag{2.3}$$
$$T_0 = 1.18 \times T_c = 9.38 \text{ keV}. \tag{2.4}$$

The electric conductance of the blob is a result of the mixing of the three phases. The monopole itself breathes at a circular frequency ω equal to the rest mass of the particle, which generates a characteristic vibration throughout the blob. ω is evaluated in natural units $\hbar\omega = m_0$. For each particle species, there is a different Yang-Mills scale Λ, which stands in relation to the dimensionless temperature as a conversion factor. $\lambda = \frac{2\pi T}{\Lambda}$. The Yang-Mills scales are hierarchically separated between Λ_{CMB} and Λ_e for electrons, Λ_{CMB}, Λ_e and Λ_μ for muons, and so on, as the rest-mass energy for the lepton in question increases. It subsequently introduces more and more mixing effects between the gauge-groups associated with these Yang-Mills scales.

When mixing $SU(2)_e$ and the $SU(2)_{CMB}$ gauge groups, at some dimensionless temperature λ_0 the pressure of the mixed plasma vanishes. At this temperature, the respective $U(1) \in SU(2)$ gauge fields couple to the particle charges as

$$q_{CMB}(\lambda_0)\sin\theta_W(\lambda_0) = \frac{4\pi}{e\left(\frac{\Lambda_e}{\Lambda_{CMB}}\lambda_0\right)}\sin\theta_W(\lambda_0), \tag{2.5}$$

$$q_e(\lambda_0)\cos\theta_W(\lambda_0) = \frac{4\pi}{e(\lambda_0)}\cos\theta_W(\lambda_0). \tag{2.6}$$

Specifically, effective external fields couple to q_{CMB} and thermal gauge fields couple to q_e. The mixed gauge field coupling to each charge with the same strength then sets

$$q_{CMB}(\lambda_0)\sin\theta_W(\lambda_0) = q_e(\lambda_0)\cos\theta_W(\lambda_0). \tag{2.7}$$

which can be used to determine the Weinberg angle θ_W. The stabilizing temperature is extracted from the stability condition for the bulk blob pressure. This identifies with $q_{CMB} \approx \sqrt{2}$, which implies $\tan\theta_W(\lambda_0) = \frac{\sqrt{8}\pi}{e(\lambda_0)}$. The stabilizing temperature, too, needs to be determined from the pressure, by solving a system of equations numerically. Thermodynamically consistent one-loop fluctuations and thermal ground state estimates lead to the evolution equations of λ [**1**]. The running coupling e with respect to λ emerges from the one-loop pressure P and energy density ρ in deconfined phase of SU(2) Yang-Mills theory ([**21**], chapter 5.2.2).

$$P(\lambda) = -\Lambda^4 \left(\frac{2\lambda^4}{(2\pi)^6} [2\bar{P}(0) + 6\bar{P}(2a)] + 2\lambda \right), \tag{2.8}$$

$$\rho(\lambda) = \Lambda^4 \left(\frac{2\lambda^4}{(2\pi)^6} [2\bar{\rho}(0) + 6\bar{\rho}(2a)] + 2\lambda \right). \tag{2.9}$$

where $a = \frac{m}{2T} = 2\pi e \lambda^{-\frac{3}{2}}$ is the dimensionless mass, and

$$\bar{P}(y) = \int_0^\infty dx\ x^2 \log\left(-e^{-\sqrt{x^2+y^2}}\right), \tag{2.10}$$

$$\bar{\rho}(y) = \int_0^\infty dx\ x^2 \frac{\sqrt{x^2+y^2}}{e^{\sqrt{x^2+y^2}} - 1}. \tag{2.11}$$

The Legendre transformation $\rho = T\frac{dP}{dT} - P$ requires at one-loop level that $\partial_m P = 0$ (implying also that $\partial_a P = 0$). This imposes a nontrivial condition on the temperature evolution of e. When evaluating $\partial_a P = 0$, a differential equation emerges for $\partial_a \lambda$. Using $D(y) = \int_0^\infty dx \frac{x^2}{\sqrt{x^2+y^2}} \frac{1}{e^{\sqrt{x^2+y^2}}-1}$,

$$\partial_a \lambda = -\frac{24\lambda^4 a}{(2\pi)^6} \frac{D(2a)}{1 + \frac{24\lambda^3 a^2}{(2\pi)^6} D(2a)}, \tag{2.12}$$

$$\Rightarrow 1 = -\frac{24\lambda^3}{(2\pi)^6} \left(\lambda \frac{da}{d\lambda} + a \right) a D(2a). \tag{2.13}$$

For very small a, $D(2a)$ reduces to some constant, and Equation 2.13 reduces to $1 = -\frac{\lambda^3}{(2\pi)^4} \left(\lambda \frac{da}{d\lambda} + a \right) a$. Solving for a eventually reveals that at λ significantly above critical temperature, $a(\lambda)$ is solved to

$$a(\lambda) = 4\sqrt{2}\pi^2 \lambda^{-\frac{3}{2}} \sqrt{1 - \frac{\lambda}{\lambda_i} \left[1 - \frac{a^2(\lambda_i)\lambda_i^3}{32\pi^4} \right]}. \tag{2.14}$$

by which $a(\lambda)$ has an attractor $a(\lambda) = 4\sqrt{2}\pi^2 \lambda^{-\frac{3}{2}}$ (a value toward which $a(\lambda)$ tends toward with $\lambda \ll \lambda_i, a(\lambda_i) \ll 1$). By this, the running of $e(\lambda)$ close to critical temperature λ_c can be determined to Figure 2.2 [**1**]. It sets $\lambda_0 = 16.3 = 1.18\lambda_{c,e}, e(\lambda_0) = 14.88$, which can be plugged directly into the definition of the Weinberg angle, yielding about 30.84 degrees. The Weinberg angle is then also a function of thermodynamics, determined from the bulk stability of the

mixed plasma and the evolution $e(\lambda)$.

At sufficiently high particle density and temperature, these blobs comprising each electron should merge into a single droplet containing as many (identical) BPS monopoles as there are electrons fused. The terms *blob* and *droplets of deconfined phase and preconfined surface* are functionally identical. In this thesis, the term *blob* is reserved for the case of a single electron as was used in [**1**], while the fused system will be referred to as a *droplet* to conform with the terminology of *plasma droplets*. A droplet of fused electron blobs should act as a system of multiple free particles with the same charge inside a conducting boundary. After fusion, the monopoles in the droplet become subject to Coulomb repulsion. At high enough particle density and temperature, several monopoles can be pressed into the same volume of deconfined phase. As a single monopole within a volume of deconfined phase describes a single electron, that process could be understood as the fusion of several electrons. Yang-Mills thermodynamics expects this at electron number densities n correlating to the Bohr radius as $N \sim \frac{1}{a_0^3}$, and at temperatures in the deconfined phase ($T > T_c 8$ keV) ([**1**], section 6).

2.2. Mirror Charge Method and Droplet Charge

The fused droplet's total charge is determined by the individual monopole charges, and their interaction with the phase boundary. For conducting surfaces, an outside observer with a test charge experiences the combination of the charge's electric field, as well as that of a reflected, but opposite mirror charge due to the spherical conducting boundary. Using the spherical mirror-charge method (Figure 2.3), and the monopole charge q_e, a total droplet radius r_0, and the distance of the monopole to the boundary $\epsilon \leq r_0$, a virtual charge $q'_e = -q_e \frac{r_0}{r_0 - \epsilon}$ is projected to the outside of the droplet as perceived by an outside test charge. Assuming a typically very large distance $o >> r_0$ to the observer charge, and expressing the distances of all charges in these known quantities, before developing over $\frac{1}{o}$ determines the electric potential of the system.

Assuming all monopoles share the same radial coordinate $r_0 - \epsilon$, their distance to the observer charge can be expressed by a generic position function s. Because the cases for $N = 2$ and $N = 3$ are 2-dimensional, while the those with a larger particle number are 3-dimensional, s needs to be defined for both cases. In two dimensions, using polar coordinates,

$$s(o, r, \theta) = \sqrt{o^2 + r^2 - 2or\cos\theta}. \tag{2.15}$$

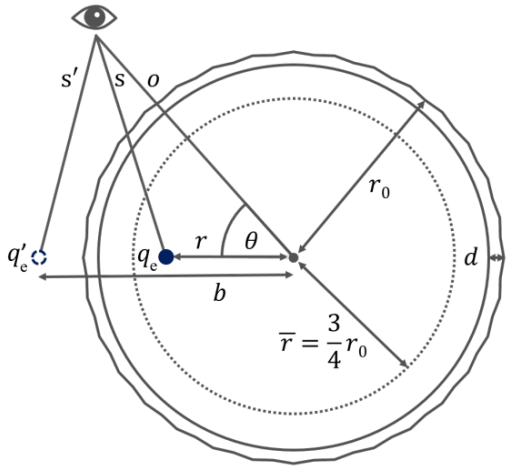

Figure 2.3: *An example of the mirror charge construction in 2 dimensions for a single monopole as performed in* **[1]**, *Figure 4. Using* $b = \frac{r_0^2}{r}$, $s = \sqrt{o^2 + r^2 - 2or\cos\theta}$, $s' = \sqrt{o^2 + \frac{r_0^4}{r^2} - 2ob\cos\theta}$. *Configurations up to* $N = 3$, *are 2-dimensional, and can be described this way. At higher* N, *the configurations are 3-dimensional, and will require a 3-dimensional mirror charge construction. In 3 dimensions* s *and* s' *will gain an additional* $\sin\varphi$ *dependency in the expressions, so that* $s = \sqrt{o^2 + r^2 - 2or\sin\varphi\cos\theta}$ *and* $s' = \sqrt{o^2 + \frac{r_0^4}{r^2} - 2ob\sin\varphi\cos\theta}$. *In this construction, the z-axis is placed onto the connecting line between observer and blob center. In further considerations set* $r = r_0 - \epsilon$.

In three dimensions,

$$s(o, r, \theta, \varphi) = \sqrt{o^2 + r^2 - 2or\sin\varphi\cos\theta}. \tag{2.16}$$

The mirror charge's position is directly defined by the position function of charge it's reflecting. Expressed in the same variable, in 2-dimensions,

$$s'(o, r, \theta) = \sqrt{o^2 + \frac{r_0^4}{r^2} - 2o\frac{r_0^2}{r}\cos\theta}, \tag{2.17}$$

and in three dimensions,

$$s'(o, r, \theta, \varphi) = \sqrt{o^2 + \frac{r_0^4}{r^2} - 2o\frac{r_0^2}{r}\sin\varphi\cos\theta}. \tag{2.18}$$

$$U = \frac{1}{4\pi}\left(\frac{q_e}{s} + \frac{q'_e}{s'}\right) \tag{2.19}$$

$$= \frac{1}{4\pi}\left(\left(\frac{q_e}{\sqrt{o^2 + (r_0 - \epsilon)^2 - 2o(r_0 - \epsilon)\sin\varphi\cos\theta}} - \frac{q_e\frac{r_0}{r_0-\epsilon}}{\sqrt{o^2 + (\frac{r_0^2}{r_0-\epsilon})^2 - 2o\frac{r_0^2}{r_0-\epsilon}\sin\varphi\cos\theta}}\right)\right)$$

$$= U(o, \theta, \varphi). \tag{2.20}$$

Given these (initial) constraints, the potential generated by a single charge in any location throughout the droplet is only dependent on the angles θ, φ which are defined relative to the axis that connects the observer charge and the center of the configuration. The full droplet's charge utilizes the sum of such potentials computed for each monopole in the droplet.

3

Coulomb Repulsion and Metastable Configurations

3.1. Single-Shell Configurations

In [**5**] an approximation of the problem of N particles with equal mass in a central potential is presented. It posits a linear central potential pulling the particles toward the center while they are subject to mutual gravitational attraction. Analogous constructions without a central potential and incorporating Coulomb repulsion instead of mutual gravitational attraction, have metastable solutions that push the particles apart, but keep the relative angles between the particles the same.

In [**5**] the force acting on each particle with index a consists of that of the central potential $\frac{1}{3}\Lambda m_a \vec{r}_a$, and the pairwise gravitational attraction in the configuration $\frac{Gm_a m_b(\vec{r}_b - \vec{r}_a)}{|\vec{r}_a - \vec{r}_b|^3}$. Both G and Λ, chosen according to the type of potential. For an attractive potential, as used in [**5**] section 2.1, they are strictly positive given strictly positive masses. For repulsive potentials, the sign of the potential must be flipped. For stability, the sum of all forces acting on any particle vanishes:

$$\frac{1}{3}\Lambda m_a \vec{r}_a + \sum_{b \neq a} \frac{Gm_a m_b(\vec{r}_b - \vec{r}_a)}{|\vec{r}_a - \vec{r}_b|^3} = 0. \tag{3.1}$$

For convenience, the center of mass of the system is placed into the origin, and the sum of momenta vanishes for a stable configuration $\sum_a m_a \vec{r}_a = 0$. Each of these contributions can be expressed using an arbitrarily chosen particle as a reference point. Doing so, allows the sum

of potentials acting on any particle to be expressed without the dependence on its mass as in

$$M = \sum_a m_a, \tag{3.2}$$

$$m_a \vec{r}_a = \frac{1}{M} \sum_{b \neq a} m_a m_b (\vec{r}_a - \vec{r}_b) + \frac{m_a}{M} \sum_b m_b r_b, \tag{3.3}$$

$$\frac{\Lambda}{3} \vec{r}_a + \sum_{b \neq a} \frac{G m_b (\vec{r}_b - \vec{r}_a)}{|\vec{r}_a - \vec{r}_b|^3} = 0. \tag{3.4}$$

This sets the sum of forces in the system to 0 entirely. The inter-particle distance $r_{ab} = |\vec{r}_a - \vec{r}_b|$ emerges, at which the particles feel no mutual force, and the configuration is stable.

$$\sum \vec{F}_{ab} = 0, \tag{3.5}$$

$$\Rightarrow \vec{F}_{ab} = m_a m_b (\vec{r}_a - \vec{r}_b) \left(\frac{\Lambda}{3M} - \frac{G}{r_{ab}^3} \right), \tag{3.6}$$

$$\Rightarrow r_{ab} = R = \left(\frac{3GM}{\Lambda} \right)^{\frac{1}{3}}. \tag{3.7}$$

For the formation of monopole crystals under Coulomb repulsion, the signs of the contributions in the force are inverted. The resulting force drives the particles apart, toward a maximal separation, while contained by an external potential. This will invert both signs of the terms in the initial potential Equation 3.1 as well, the total of which evaluates to zero. All the extrapolations made using this ansatz will then have identical mathematical bases. This approach, extrapolated to large particle numbers, still eventually leads to the sphere packing problem, but more importantly, the solutions conform to the known configurations that solve the Thomson problem at low particle numbers N. The Thomson problem determines the configuration of N equal point charges constrained to the surface of a unit sphere that has the minimal potential energy [**35**]. For single-shell configurations especially, meaning up to $N = 12$, it's expected that they are solutions to the Thomson problem. As more shells emerge, each shell should solve the Thomson problem in isolation of the remaining particles of the configuration.

For this thesis, the maximal number of particles in single-shell configurations is determined by taking into account the results of the Gregory Newton problem that for equal spheres, wherein one sphere can only be in contact with 12 others at the most ([**5**], section 2.9;

[**23**], [**24**]). Assuming all the charges exist in some positively charged spatial domain Ω, the critical points with respect to r_i of V are solutions to the potential equation (Equation 3.1). To move forward, the potential V needs to be identified explicitly. Straight-forwardly, V is the integral of Equation 3.1, and the integration constant can be set to 0, so that

$$0 = \int d\vec{r}_a \frac{1}{3}\Lambda m_a \vec{r}_a + \sum_{b\neq a} \frac{G m_a m_b (\vec{r}_b - \vec{r}_a)}{|\vec{r}_a - \vec{r}_b|^3} \tag{3.8}$$

$$= \frac{\Lambda}{6}\sum_a m_a \vec{r}_a^2 + \sum_a \sum_{b<a} \frac{G m_a m_b (\vec{r}_b - \vec{r}_a)}{|\vec{r}_a - \vec{r}_b|^3} \frac{1}{\frac{\vec{r}_a - \vec{r}_b}{|\vec{r}_a - \vec{r}_b|^2}} \tag{3.9}$$

$$= \frac{\Lambda}{6}\sum_a m_a \vec{r}_a^2 + \sum_a \sum_{b<a} \frac{G m_a m_b}{|\vec{r}_a - \vec{r}_b|}. \tag{3.10}$$

The resulting summands are homogenous functions in $\vec{r}_a$ named here according to their homogeneous degrees in r_a, so that $V \coloneqq V_{-1} + V_2$

$$V_{-1} \coloneqq \sum_a \sum_{b<a} \frac{G m_a m_b}{|\vec{r}_a - \vec{r}_b|}, \tag{3.11}$$

$$V_2 \coloneqq \frac{\Lambda}{6}\sum_a m_a \vec{r}_a^2. \tag{3.12}$$

V_{-1} is of homogeneous degree -1 and V_2 is of homogeneous degree 2 in $\vec{r}_a$. Euler's theorem of homogeneous functions states that for homogeneous functions $f(x_0, x_1, ...) = \sum_{i=0} \partial_{x_i} f$, and $\partial_{x_i} f = n_i f$ for the homogeneous degree n_i of f in the variable x_i. Applying it to V_{-1} and V_2 for each $\vec{r}_a$, and keeping in mind that $V = const$ as per the stability of the configuration, results in

$$const = V_{-1} + V_2, \tag{3.13}$$

$$\Rightarrow 0 = \partial_{\vec{r}_a}(V_{-1} + V_2), \tag{3.14}$$

$$\Rightarrow 0 = -V_{-1} + 2V_2, \tag{3.15}$$

$$\Rightarrow V_{-1} = 2V_2. \tag{3.16}$$

Since the monopoles inside one droplet are essentially interchangeable, the potential acting on each monopole can be determined analogously to the potential acting on each particle in a one-component plasma. This potential is commonly decomposed into three parts

$V_{OCP} = V_{--} + V_{+-} + V_{++}$, where, V_{--} is the positive mutual electrostatic energy, V_{+-} is the electrostatic potential of the negative charges in the uniformly distributed positive background, and V_{++} is the potential energy of the uniformly positive background. The notation is chosen to fit a one-component-plasma with uniformly negatively charged particles ([**33**], Chapter 2.2). The integrals that show up in each contribution are evaluated to the case where Ω is a ball of radius R.

$$V_{--} \coloneqq V_{-1}, \tag{3.17}$$

$$V_{+-} \coloneqq -GM \sum_a \left(\frac{m_a}{A} \int \frac{d^3\vec{r}}{|\vec{r} - \vec{r}_a|} \right) = -\frac{3GM^2}{2R} + \frac{GM}{2R^3} \sum_a m_a \vec{r}_a^2, \tag{3.18}$$

$$V_{++} \coloneqq \frac{1}{2} GM^2 \left(\frac{1}{A^2} \int \int \frac{d^3\vec{r} d^3\vec{r}'}{|\vec{r} - \vec{r}'|} \right) = \frac{3}{5} \frac{GM^2}{R}. \tag{3.19}$$

The critical points of equilibria of V_{OCP} and V coincide for $\frac{3GM}{\Lambda} = R^3$, though their values are generally different.

To optimize for a stable configuration, the minimal energy of the configuration is approximated. The upper bound for this can be determined through Williamson averages, which identify the separation of two points uniformly distributed in a sphere of a given radius R [**25**]. Williamson's results can be replicated in briefer form as in [**5**], section 2.6, by the use of differential forms. The volume form given two points $\vec{r}_1, \vec{r}_2$ in spherical coordinates about a fixed axis going through the origin O is written

$$\omega = r_1^2 \sin\theta_1 dr_1 \wedge d\theta_1 \wedge d\phi_1 \wedge r_2^2 \sin\theta_2 dr_2 \wedge d\phi_2. \tag{3.20}$$

Let $\overline{O12}$ be a triangle with $\psi = \angle O12$, sides of length r_1, r_2 and r_{12}, and χ the angle of its plane around an axis $\overline{O1}$. The rotation of Equation 3.20 around ψ and χ is

$$\omega = r_1^2 \sin\theta_1 dr_1 \wedge d\theta_1 \wedge d\phi_1 \wedge r_{12}^2 2 \sin\psi dr_{12} \wedge d\psi \wedge d\chi, \tag{3.21}$$

which results in a cosine formula of $r_2^2 = r_1^2 + r_{12}^2 - 2r_1 r_{12} \cos\psi$. Substituting back the initial coordinates for $d\psi$ and computing the integral reduces the volume form to $\omega = 8\pi^2 r_1 r_2 r_{12} dr_1 \wedge dr_2 \wedge dr_{12}$. Setting $r = r_{12}$ and integrating the form over r_1 and r_2, and assuming that points 1 and 2 lie inside a ball of radius R around the origin gives the probability

density $\rho(r)$. This density needs to be normed by the integration's Jacobian determinant and the contribution of R.

$$\rho(r)dr = \left(\frac{3r^2}{R^3} - \frac{9r^3}{4R^4} + \frac{3r^5}{16R^6}\right)dr, \tag{3.22}$$

$$\Rightarrow \langle r \rangle = \int_0^{2R} r\rho(r)dr \tag{3.23}$$

$$= \left[\frac{3r^4}{4R^3} - \frac{9r^5}{20R^4} + \frac{3r^7}{112R^6}\right]_0^{2R} \tag{3.24}$$

$$= \frac{36}{35}R. \tag{3.25}$$

For large N, an upper bound for $\frac{36}{35}R$ that develops with N can be approximated through $\frac{9}{10}N(N-1)^{\frac{2}{3}}$.

A lower bound for the potential energy can be directly taken from the rigorous lower bound for potentials of one-component plasma identified in [**26**]. It can be rewritten in terms of particle number to $\frac{9}{10}N(N^{\frac{2}{3}} - 1)$. Therefore, the minimal energy can be approximated to between $\frac{9}{10}N(N^{\frac{2}{3}} - 1)$ and $\frac{9}{10}N(N-1)^{\frac{2}{3}}$. By the separation probability distribution, the computation for large numbers can be streamlined by not populating the domain with singular points, but rather with triples of points, creating triangles. For lower particle numbers, face-centered cubic structure (FCC) can be assumed due to a conjecture by Harriot and Kepler (proven 2002 by Hales [**6**]), though it's possible for there to be a configuration with the same density, i.e. same energy distribution between particles. Since FCC is a crystalline configuration, its application will result in structures that are hexagonal one way, and square the other. For large N, such configurations will necessarily leave layers of empty space when attempting to fill a spherical volume. While there are an uncountable number of packings with the same density, conveniently, local variations of density smooth out with large enough particle number.

The bounds are approximated using N instead of the radius R of the configuration, because identifying the radius is a nontrivial problem, and for metastable configurations, it is also not a constant quality.

The assumption that solutions that form regular polyhedra fit the criteria to minimize the electric field potential created by the particle charges is not incorrect from the outset, though it seems that they're not necessarily metastable solutions. Most solutions can be

successfully approximated by structures with regular triangles as faces. They are classified as regular deltahedra with exactly as many vertices as they have corners. Up to $N = 12$, this will be almost all of them, and those numbers that don't have a corresponding deltahedron will necessarily include some irregular (square) faces. At higher particle numbers, shells of this structure will become increasingly rare exceptions. In configurations with particle numbers slightly above $N = 12$ a concentric shell structure emerges, wherein particles can be sorted into groups sharing a radial coordinate, that form concentric, usually polyhedral solutions. The distances between each shell are expected to be approximately equidistant.

Regular deltahedron solutions do not exist for all N. In the range from $N = 4$ to 12, the exception is $N = 11$ ([**31**], [**32**]). As a consequence, the edge lengths for the $N = 11$ configuration vary more strongly than those of the other regular deltahedral configurations. For $N = 8$, the regular regular deltahedron configuration's energy doesn't conform to the minimal energy constraints. There exists another configuration whose energy conforms to the minimal energy constraints. It is used instead of the $V = 8$ regular deltahedron.

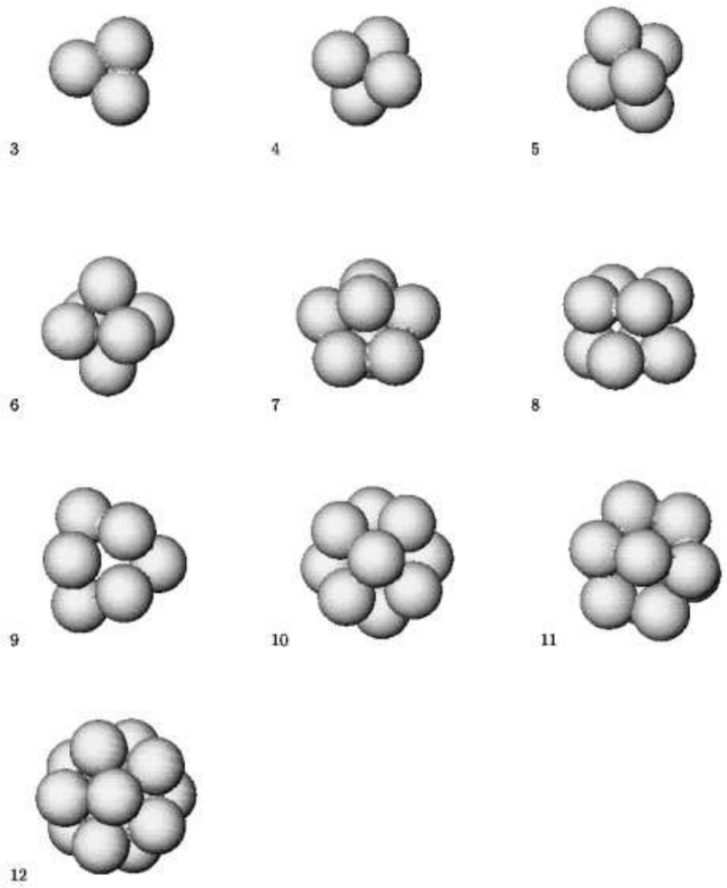

Figure 3.1: *A rendering of stable Configurations for small numbers of identical particles in an attractive central potential as seen in [**5**], Figure 1*
*These configurations are visualisations of the numerical solutions in [**5**] under the restraints of potentials and the conditions for stability emerging from Equation 3.1. For low particle numbers, (meta-)stable configurations are mostly constructed from regular tetrahedra. Up to $N = 12$, all particles can form positions of the same radius away from the configuration center. Not all numbers of particles can occupy a regular tetrahedral configuration. The exceptions in this list are $N = 8$ and $N = 11$. The $N = 8$ case stands out notably because it's the only configuration that contains two square faces. The $N = 11$ case is tetrahedral, but containes vertices with lengths that differ more heavily than would be expected for regular tetrahedra.*

The construction creates a stable configuration with particles whose mass-charge ratio is identical. This is analogous to the configurations comprising *Coulomb Crystals* [**2**], though using BPS monopoles, rather than ions. In inspections of Coulomb Crystals, numerical (and to a lesser extent analytical) derivations of their stable configurations yield regular polyhedra. Through [**7**], we obtain eleven stable configurations with $N \geq 2$ particles up to $N = 12$ as depicted in Figure 3.1, after which a second shell would be required. The entire shell structure is based upon numerically determined *magic numbers* at which they appear especially stable. These magic numbers describe the particle numbers at which a new shell becomes absolutely necessary for the configuration to still fulfill metastability. The second

shell emerges at $N = 13$, and the third at $N = 61$. For higher shells, the magic numbers provide only approximations. According to numerical estimates, new shells emerge at around $N = 147, 309, 565, 1400, 2100, ...$ The exact values don't seem to adhere to a regular sequence. The tables depicted in Figure 3.2 and Figure 3.3 show that this structure remains consistent between identical neutral and charged particles in a central attractive potential and mutual Coulomb repulsion.

R. W. HASSE AND V. V. AVILOV

TABLE I. Structures ($N_M + N_{M-1} + \cdots + N_1$ particles in subshells), rms radii, and energies of N-particle systems.

N	Structure	$R_{\rm rms}$	ε	Γ
2	2	0.6300	0.5953	∞^a
3	3	0.8327	1.0400	∞^a
4	4	0.9721	1.4174	∞^a
5	5	1.0901	1.7820	10^5
6	6	1.1850	2.1065	10^5
7	7	1.2736	2.4321	10^5
8	8	1.3500	2.7331	10^5
9	9	1.4198	3.0238	10^5
10	10	1.4846	3.3058	10^5
11	11	1.5453	3.5822	10^5
12	12	1.6002	3.8407	10^5
13	12+1	1.6535	4.1009	10^5
14	13+1	1.7036	4.3542	10^5
15	14+1	1.7508	4.5972	10^5
16	15+1	1.7956	4.8364	10^5
17	16+1	1.8387	5.0707	10^5
18	17+1	1.8852	5.3010	10^5
19	18+1	1.9197	5.5275	10^5
20	19+1	1.9583	5.7521	10^5
21	20+1	1.9947	5.9705	10^5
22	21+1	2.0311	6.1873	10^5
23	21+2	2.0657	6.4001	10^5
24	22+2	2.0990	6.6090	10^5
25	23+2	2.1318	6.8166	10^5
26	24+2	2.1633	7.0197	10^5
27	24+3	2.1941	7.2206	10^5
28	24+4	2.2241	7.4200	10^5
29	26+3	2.2532	7.6162	10^5
30	27+3	2.2818	7.8098	10^5
31	28+3	2.3098	8.0026	10^5
32	28+4	2.3368	8.1900	10^5
33	29+4	2.3635	8.3788	10^5
34	30+4	2.3895	8.5648	10^5
35	30+5	2.4150	8.7488	10^5
36	30+6	2.4401	8.9307	10^5
37	31+6	2.4646	9.1107	10^5
38	32+6	2.4885	9.2887	10^5
39	33+6	2.5123	9.4676	10^5
40	34+6	2.5356	9.6437	10^5
41	35+6	2.5585	9.8187	10^5
42	35+7	2.5810	9.9921	10^5
43	36+7	2.6031	10.1638	10^5
44	37+7	2.6222	10.3342	10^5
45	38+7	2.6464	10.5041	10^5
46	38+8	2.6667	10.6711	10^5
47	38+9	2.6881	10.8376	10^5
48	39+9	2.7078	11.0029	10^5
54	42+12	2.8254	11.9737	10^5
60	48+12	2.9335	12.9085	10^5
61	48+12+1	2.9511	13.0611	10^5
62	48+13+1	2.9680	13.2135	10^5
63	48+14+1	2.9849	13.3642	10^5
64	48+15+1	3.0017	13.5146	10^5
65	49+15+1	3.0183	13.6644	10^5
66	50+15+1	3.0345	13.8128	10^5
80	58+20+2	3.2479	15.8244	10^5
96	67+25+4	3.4625	17.9833	10^5
100	69+27+4	3.5123	18.5035	10^6
115	78+31+6	3.6876	20.3963	10^5

Figure 3.2: *A table listing the magic number shell structure for Coulomb crystals, as seen in* [**7**]*, Table 1*
Results of an investigation of the structure of Coulomb Crystals, along with the full system size and full system energies. The conception of this object is identical to that of the Monopole Crystal up to its full system parameters. R_{rms} *is the radius in units of the Wigner-Seitz radius* $a_{WS} = (\frac{q^2}{K})^{\frac{1}{2}}$*, where* q *is the particle charge for one of the nuclei, and* K *is derived from the external confining force* $F_i = -Kr_i$ *required to keep the Coulomb Crystal at an equilibrium.* ε *is the total energy per particle in units of* $\frac{q^3}{a_{WS}}$*.* Γ *is the approximate ratio between Coulomb potential and kinetic energy aimed at during the construction of the Coulomb Crystal.*

N	V	V/Bound	Shells	N	V	V/Bound	Shells
1	0.0000	1.000000	01/00/00	51	586.1361	1.001364	10/41/00
2	1.1906	1.126006	02/00/00	52	606.0110	1.001339	10/42/00
3	3.1201	1.069919	03/00/00	53	626.1669	1.001335	10/43/00
4	5.6696	1.036227	04/00/00	54	646.5716	1.001305	10/44/00
5	8.9100	1.029100	05/00/00	55	667.2312	1.001261	12/43/00
6	12.6391	1.016787	06/00/00	56	688.1384	1.001197	12/44/00
7	17.0243	1.016157	07/00/00	57	709.3484	1.001194	12/45/00
8	21.8643	1.012236	08/00/00	58	730.8185	1.001192	01/12/45
9	27.2144	1.009937	09/00/00	59	752.5386	1.001178	01/12/46
10	33.0575	1.008642	10/00/00	60	774.5108	1.001159	12/48/00
11	39.4041	1.008647	11/00/00	61	796.7202	1.001117	01/12/48
12	46.0883	1.006118	12/00/00	62	819.2150	1.001116	01/13/48
13	53.3116	1.006132	01/12/00	63	841.9375	1.001085	01/14/48
14	60.9584	1.006069	01/13/00	64	864.9324	1.001079	01/14/49
15	68.9578	1.005074	01/14/00	65	888.1564	1.001050	01/14/50
16	77.3816	1.004509	01/15/00	66	911.6371	1.001031	01/15/50
17	86.2009	1.004020	01/16/00	67	935.3691	1.001017	01/15/51
18	95.4178	1.003699	01/17/00	68	959.3390	1.000994	01/16/51
19	105.0215	1.003470	01/18/00	69	983.5543	1.000973	01/16/52
20	115.0418	1.003635	01/19/00	70	1008.0264	1.000965	01/16/53
21	125.3808	1.003364	01/20/00	71	1032.7387	1.000955	01/16/54
22	136.1199	1.003403	01/21/00	72	1057.6937	1.000947	01/17/54
23	147.2015	1.003330	02/21/00	73	1082.8858	1.000935	01/17/55
24	158.6157	1.003140	02/22/00	74	1108.3176	1.000925	01/17/56
25	170.4147	1.003193	02/23/00	75	1133.9875	1.000914	01/18/56
26	182.5115	1.002991	02/24/00	76	1159.9000	1.000909	01/18/57
27	194.9551	1.002855	03/24/00	77	1186.0483	1.000903	01/18/58
28	207.7545	1.002841	03/25/00	78	1212.4297	1.000896	01/18/59
29	220.8612	1.002723	04/25/00	79	1239.0530	1.000896	01/18/60
30	234.2757	1.002540	04/26/00	80	1265.9012	1.000888	01/20/59
31	248.0035	1.002339	04/27/00	81	1292.9691	1.000872	01/20/60
32	262.0781	1.002265	04/28/00	82	1320.2933	1.000875	02/20/60
33	276.4994	1.002311	04/29/00	83	1347.8394	1.000871	02/21/60
34	291.1997	1.002238	04/30/00	84	1375.6035	1.000859	02/21/61
35	306.2062	1.002160	05/30/00	85	1403.5980	1.000850	02/21/62
36	321.5036	1.002043	06/30/00	86	1431.8213	1.000841	02/21/63
37	337.0954	1.001909	06/31/00	87	1460.2694	1.000831	02/22/63
38	352.9683	1.001731	06/32/00	88	1488.9476	1.000825	02/22/64
39	369.2331	1.001823	06/33/00	89	1517.8678	1.000830	03/22/64
40	385.7436	1.001779	06/34/00	90	1546.9950	1.000824	03/22/65
41	402.5671	1.001788	06/35/00	91	1576.3474	1.000819	03/23/65
42	419.6643	1.001757	07/35/00	92	1605.9053	1.000803	03/22/67
43	437.0420	1.001710	07/36/00	93	1635.6839	1.000788	03/24/66
44	454.6979	1.001650	08/36/00	94	1665.6841	1.000774	03/24/67
45	472.6332	1.001585	08/37/00	95	1695.9225	1.000770	04/24/67
46	490.8654	1.001556	08/38/00	96	1726.3794	1.000767	04/24/68
47	509.3649	1.001505	09/38/00	97	1757.0511	1.000761	04/25/68
48	528.1383	1.001451	09/39/00	98	1787.9348	1.000753	04/25/69
49	547.1978	1.001420	09/40/00	99	1819.0277	1.000740	04/26/69
50	566.5327	1.001394	09/41/00	100	1850.3349	1.000727	04/26/70

Table 6: For $N \leq 100$ we list the minimum energy V, the ratio of this energy to the lower bound, and the number of points in each shell.
20

Figure 3.3: *A table listing the magic number shell structure for generic particles, as seen in* **[5]***, Table 6*
These are results from the same simulation that yielded Figure 3.1. Expectations for the generic shell structures, to which the monopole crystals for small N are expected to adhere. The shell structure is associated with the simulated minimum energy V associated with the particle number, according to the approximation, and its ratio V/Bound with its lower bound $\frac{9}{10}N(N^{\frac{2}{3}} - 1)$.

The model constructed in this thesis will treat the monopoles as classical objects initially and introduce aspects of their quantum nature as the analysis continues.

3.2. Complexities of the Multi-Shell Configuration

Several approaches identify the configurations associated with any small particle number via purely numerical simulations, aimed at solving either the Tammes problem or the Coulomb surface problem. The Tammes problem aims to find the largest angular diameter between two spheres, each with an equal distance to some reference point, and disallowing overlap [**18**], while the Coulomb surface problem is the search for a stable configuration, at which N particles are at a potential minimum when confined to a single shell [**28**]. An approach allowing for multi-shell configurations would then require the combined solutions of either one of the previous problems, along with the magic-number reference table given by [**5**], as the stability of the shells supercedes the solutions of the Coulomb surface problem. As described by [**8**], the solutions for any particle number are only unique in energy-space, up to collective rotation at which angles between particles do not change. As a result, taking the magic numbers as the indicator for the shell structures, and using symmetry arguments as methods to relate the radii of each shell with those of the others, as well as the relative particle positions, should provide solutions for multi-shell configurations. These solutions are not unique in their energy, and so different configurations may be possible for larger particle numbers. In practice, this is more difficult, and will also create further difficulties when identifying the potential.

Configurations consisting of at least two concentric regular polyhedra will exhibit favored, but unstable potential minima between the polyhedrical shells, as well as the mutually interacting relations between the radial coordinates leading to a state that will generally provide configurations that are not metastable. This combination of factors makes the following computations for higher-particle number configurations significantly more difficult, as the radial motion of the system's relaxation will have to be described by a number of time-dependent radial functions, which are determined entirely by the geometry of the initial configuration, including the rotation of the shells against one another.

The $N = 13$ is the only multi-shell case that retains the uniform magnitude of force exerted on each monopole of the outer shell. The full configuration is identical to that of $N = 12$, with an additional monopole positioned at the center. This introduces a second radius r' to the expression of the potential, although it doesn't show up in the numerically determined expression, seeing as the particle remains stationary at the center, so the relative radius evaluating to a constant 0. Notably, the terms arising from the monopole at the center of the configuration include a portion that cancels the dependence of r' for large distances of the observer. Because of their added complexities, configurations for larger N are not considered in this thesis.

4

Multipole Expansion

4.1. Multipole Geometry in Spherical, Relative Fixed Coordinates

The results of [**5**] explicitly state meta-stability of the crystal configurations. This means that any motion performed by a single monopole in the metastable crystal configuration should imply complementary motion of the other monopoles. For single-shell configurations, all monopoles must be positioned the same radius away from the configuration center, which can be arbitrarily set to the center of the spherical coordinate system, and so the particles' position is described fully by the angular coordinates φ, θ, by simply adding the appropriate angle-offsets for each particle in the configuration.

There is no generic way to obtain the coordinates, as there is no generic, analytic way to identify the positions of the stable configuration. As a consequence, this thesis only uses configurations that are known beforehand. Using the graphics provided in [**5**], and choosing a convenient initial orientation of the configuration, Table 4.1 describes the particle position at a uniform radius r. A sketch of the process is provided in Figure 4.1.

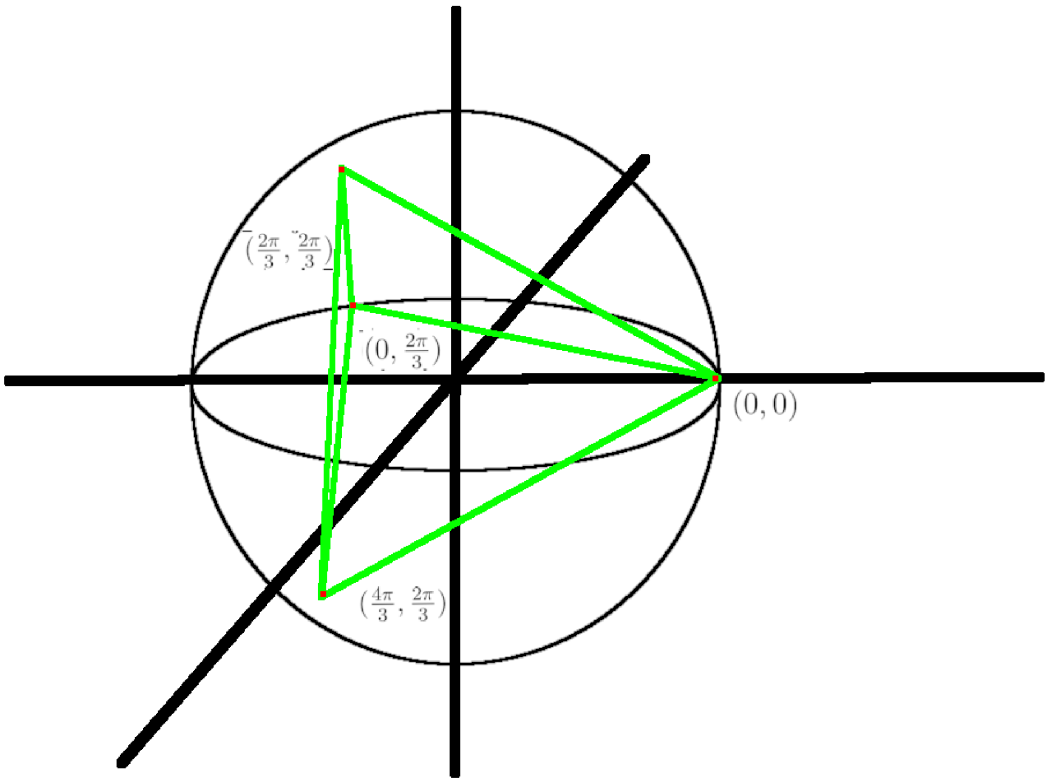

Figure 4.1: *An example visualisation of the coordinates used for $N = 4$. The green tetrahedral outline indicates the triangle-faces used in [**5**]. The monopoles are thought to sit in the corners. The $(\theta = 0, \varphi = 0)$-position is chosen to lie on a convenient axis with the origin, and will be considered the reference particle. The remaining coordiates are written as a constant offset that is maintained, if θ and φ for that reference particle changes, i.e. $(0, \frac{2\pi}{3}) \rightarrow (\theta + 0, \varphi + \frac{2\pi}{3})$. The radial coordinate is identical across all monopoles in the configuration and thus is omitted.*

4.2. Unperturbed Field Potentials of Monopole Crystals

In the fused-electron droplet, there is no external potential acting on the monopoles. The monopoles are only interacting mutually via Coulomb repulsion. As a consequence, there is no set value of the monopole's radial coordinate for which the forces of the monopoles cancel. Instead, the radius is left variable, and given some initial value, chosen sufficiently far enough away from the droplet's periphery. The choice of coordinates is shown in Figure 4.2. In the following, this initial radius $r = r_0 - \epsilon$ is chosen to be a constant third of the full droplet's radius r_0. Having identified the shapes of the monopole-crystals (Figure 3.1), one can use the mirror charge construction to compute the far-field potential. In Table 4.2 each term of the multipole expansion that makes up the potential is separated out.

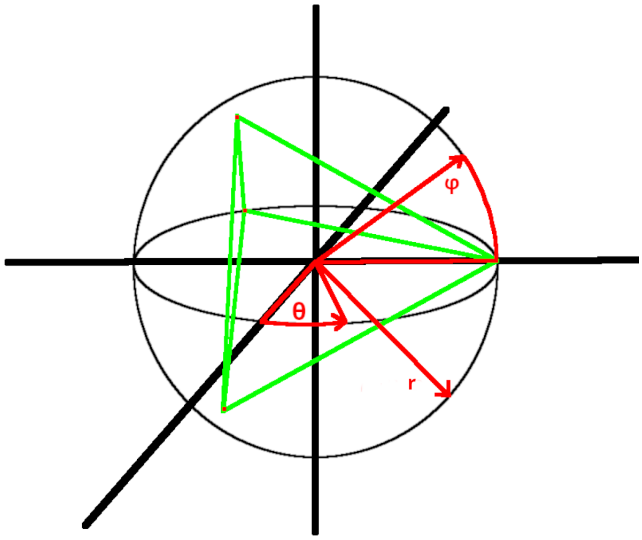

Figure 4.2: *An example visualisation of the coordinates used for the example of $N = 4$. The green tetrahedral outline indicates the triangle-faces used in [5]. The monopoles are thought to sit in the corners. The axes and coordinates are drawn and labeled in red. The radial coordinate is set to a constant value.*

The computation of the far-field charge-potential presupposes knowledge of the location for each particle in the configuration relative to some arbitrarily chosen reference particle within said configuration as is recorded in Table 4.1. This sum of charges and mirror charges, reflected by introduction of a uniform distance of the particles from the droplet radius, is then developed around the distance o of the configuration's center to a test charge necessitated by the mirror charge construction.

The sum is averaged over a full rotation in spherical coordinates, while retaining stiffness of the configuration. For this, the radius is kept at a constant value $r = \frac{r_0}{3}$. The

N	2	3	4	5	6	7	8	9	10	11	12
Pos 1	$(0,0)$	$(0,0)$	$(0,0)$	$(0,0)$	$(0,0)$	$(0,0)$	$\left(0,\frac{\pi}{3}\right)$	$\left(0,\frac{\pi}{4}\right)$	$(0,0)$	$(0,0)$	$(0,0)$
Pos 2	$(0,\pi)$	$\left(0,\frac{2\pi}{3}\right)$	$\left(0,\frac{2\pi}{3}\right)$	$\left(0,\frac{\pi}{2}\right)$	$\left(0,\frac{\pi}{2}\right)$	$\left(0,\frac{\pi}{2}\right)$	$\left(\frac{\pi}{2},\frac{\pi}{3}\right)$	$\left(\pi,\frac{2\pi}{3}\right)$	$\left(\frac{\pi}{2},\frac{2\pi}{3}\right)$	$\left(\frac{\pi}{3},\frac{\pi}{4}\right)$	$\left(\frac{\pi}{5},\frac{2\pi}{3}\right)$
Pos 3		$\left(0,\frac{4\pi}{3}\right)$	$\left(\frac{2\pi}{3},\frac{2\pi}{3}\right)$	$\left(\frac{2\pi}{3},\frac{2\pi}{2}\right)$	$\left(\frac{\pi}{2},\frac{\pi}{2}\right)$	$\left(\frac{2\pi}{5},\frac{\pi}{2}\right)$	$\left(\pi,\frac{\pi}{3}\right)$	$\left(\frac{3\pi}{2},\frac{2\pi}{3}\right)$	$\left(\pi,\frac{2\pi}{3}\right)$	$\left(\pi,\frac{\pi}{4}\right)$	$\left(\frac{3\pi}{5},\frac{2\pi}{3}\right)$
Pos 4			$\left(\frac{4\pi}{3},\frac{2\pi}{3}\right)$	$\left(\frac{4\pi}{3},\frac{\pi}{2}\right)$	$\left(\pi,\frac{\pi}{2}\right)$	$\left(\frac{4\pi}{5},\frac{\pi}{2}\right)$	$\left(\frac{3\pi}{2},\frac{\pi}{3}\right)$	$\left(\frac{\pi}{3},\frac{\pi}{2}\right)$	$\left(\frac{3\pi}{2},\frac{2\pi}{3}\right)$	$\left(\frac{5\pi}{3},\frac{\pi}{4}\right)$	$\left(\pi,\frac{2\pi}{3}\right)$
Pos 5				$(0,\pi)$	$\left(\frac{3\pi}{4},\frac{\pi}{2}\right)$	$\left(\frac{6\pi}{5},\frac{\pi}{2}\right)$	$\left(\frac{\pi}{4},\frac{2\pi}{3}\right)$	$\left(\pi,\frac{\pi}{2}\right)$	$\left(\pi,\frac{2\pi}{3}\right)$	$\left(\frac{2\pi}{3},\frac{\pi}{2}\right)$	$\left(\frac{7\pi}{5},\frac{2\pi}{3}\right)$
Pos 6					$(0,\pi)$	$\left(\frac{8\pi}{5},\frac{\pi}{2}\right)$	$\left(\frac{3\pi}{4},\frac{2\pi}{3}\right)$	$\left(\frac{5\pi}{3},\frac{\pi}{2}\right)$	$\left(\frac{\pi}{4},\frac{4\pi}{3}\right)$	$\left(\frac{4\pi}{3},\frac{\pi}{2}\right)$	$\left(\frac{9\pi}{5},\frac{2\pi}{3}\right)$
Pos 7						$(0,\pi)$	$\left(\frac{5\pi}{4},\frac{2\pi}{3}\right)$	$\left(0,\frac{3\pi}{4}\right)$	$\left(\frac{3\pi}{4},\frac{4\pi}{3}\right)$	$\left(\frac{6\pi}{3},\frac{\pi}{2}\right)$	$\left(0,\frac{4\pi}{3}\right)$
Pos 8							$\left(\frac{7\pi}{4},\frac{2\pi}{3}\right)$	$\left(\frac{2\pi}{3},\frac{3\pi}{4}\right)$	$\left(\frac{5\pi}{4},\frac{4\pi}{3}\right)$	$\left(\frac{\pi}{3},\frac{3\pi}{4}\right)$	$\left(\frac{2\pi}{5},\frac{4\pi}{3}\right)$
Pos 9								$\left(\frac{4\pi}{3},\frac{3\pi}{4}\right)$	$\left(\frac{7\pi}{4},\frac{4\pi}{3}\right)$	$\left(\pi,\frac{3\pi}{4}\right)$	$\left(\frac{4\pi}{5},\frac{4\pi}{3}\right)$
Pos 10									$(0,\pi)$	$\left(\frac{5\pi}{3},\frac{3\pi}{4}\right)$	$\left(\frac{6\pi}{5},\frac{4\pi}{3}\right)$
Pos 11										$(0,\pi)$	$\left(\frac{8\pi}{5},\frac{4\pi}{3}\right)$
Pos 12											$(0,\pi)$

Table 4.1:
The particle positions (φ,θ) for metastable configurations with particle number N, dependent on shared coordinates φ and θ. The exact coordinates are identified empirically and expressed here only through an offset (i.e. $(\alpha,\beta)\to(\varphi+\alpha,\theta+\beta)$), so that the configuration is stiff, and defined up to a shared radial coordinate. Because the radial coordinate is the same for each monopole, it has been omitted in this table. Each column describes the full set of particle coordinates for that particle number.

contribution of the radius in the transformation factor is canceled by the integration constant and derivative. The generalized surface-density for the sphere's surface is $\frac{r^2}{4\pi r^2}\sin\theta = \frac{1}{4\pi}\sin\theta$.

Using the numerically determined position functions s, s' defined in Equation 2.20, the full rotationally averaged potential acting on a test charge is written

$$U(\varphi,\theta,\epsilon,o) = \int d\phi d\theta \,(\frac{q_e}{s_1(\varphi,\theta,\epsilon,o)} + \frac{\frac{q_e r_0}{r_0-\epsilon}}{s_1'(\varphi,\theta,\epsilon,o)} + \frac{q_e}{s_2(\varphi,\theta,\epsilon,o)} + \frac{\frac{q_e r_0}{r_0-\epsilon}}{s_2'(\varphi,\theta,\epsilon,o)} + ...) \times \frac{\sin\theta}{4\pi}. \tag{4.1}$$

The potentials of configurations that form regular tetrahedra are generally of the form

$$U(\epsilon,o) = \frac{q_e}{o}\frac{(r_0(-a + \frac{br_0^4}{(r_0-\epsilon)^2 o^2}) + a(r_0-\epsilon) - \frac{b}{o^2}(r_0-\epsilon)^3)}{c(r_0-\epsilon)} \tag{4.2}$$

$$= \frac{q_e}{o}\left(-\frac{a\epsilon}{c(r_0-\epsilon)}\right) + \frac{q_e}{o^3}\left(\frac{br_0^5}{(r_0-\epsilon)^3} - b(r_0-\epsilon)^2\right). \tag{4.3}$$

up to quadrupole order, where a, b, c are positive integer constants, which differ with the particle number. The origin of their numerical value is not immediately clear from the configuration's construction, and they seem not to have any direct relation to the particle number. The multipole expansion's terms can be separated out by writing the potential as a sum of the form

$$U(R,\epsilon,o) = q_e \sum_{i=1} \frac{1}{o^i}\mathcal{U}_i(R,\epsilon), \tag{4.4}$$

where the exponent of o determines the order of multipole moment $\mathcal{U}_i$. The dimensions of $\mathcal{U}_i$ is [charge][length]$^{i-1}$. The results are recorded in Table 4.2.

N	$\mathcal{U}_1$	$\mathcal{U}_2$	$\mathcal{U}_3$
2	$-\frac{2\epsilon}{4\pi(r_0-\epsilon)}$	0	$-\frac{3\mathcal{R}_5}{16\pi(r_0-\epsilon)^3}$
3	$-\frac{3\epsilon}{4\pi(r_0-\epsilon)}$	0	$-\frac{7\mathcal{R}_5}{64\pi(r_0-\epsilon)^3}$
4	$-\frac{4\epsilon}{4\pi(r_0-\epsilon)}$	0	$-\frac{7\mathcal{R}_5}{64\pi(r_0-\epsilon)^3}$
5	$-\frac{5\epsilon}{4\pi(r_0-\epsilon)}$	0	$-\frac{\mathcal{R}_5}{8\pi(r_0-\epsilon)^3}$
6	$-\frac{6\epsilon}{4\pi(r_0-\epsilon)}$	0	$-\frac{\mathcal{R}_5}{8\pi(r_0-\epsilon)^3}$
7	$-\frac{7\epsilon}{4\pi(r_0-\epsilon)}$	0	$-\frac{\mathcal{R}_5}{8\pi(r_0-\epsilon)^3}$
8	$-\frac{8\epsilon}{4\pi(r_0-\epsilon)}$	0	$-\frac{\mathcal{R}_5}{8\pi(r_0-\epsilon)^3}$
9	$-\frac{9\epsilon}{4\pi(r_0-\epsilon)}$	0	$-\frac{3\mathcal{R}_5}{16\pi(r_0-\epsilon)^3}$
10	$-\frac{10\epsilon}{4\pi(r_0-\epsilon)}$	0	$-\frac{\mathcal{R}_5}{4\pi(r_0-\epsilon)^3}$
11	$-\frac{11\epsilon}{4\pi(r_0-\epsilon)}$	0	$-\frac{5\mathcal{R}_5}{16\pi(r_0-\epsilon)^3}$
12	$-\frac{12\epsilon}{4\pi(r_0-\epsilon)}$	0	$-\frac{9\mathcal{R}_5}{32\pi(r_0-\epsilon)^3}$

Table 4.2: *The multipole moments of the metastable, stiff configuration as a result of a full rotational average, and exclusively dependent on the system's radius r_0, and the distance away from the system boundary ϵ. As should be expected, the angular dependencies are fully integrated out. The potentials notably depend on the full system radius r_0, the distance between particle and system boundary ϵ, the distance to the observer charge and the full observer charge. The orders of $\frac{1}{o^n}$ are omitted.*

Table 4.2 uses the definition $\mathcal{R}_n = -r_0^n + (r_0 - \epsilon)^n$. This is a recurring term. Its inclusion is primarily for legibility, as it reappears frequently in later considerations. Note here, that the dipole contributions vanish for almost all configurations, and the resulting terms carry no dependence of ϕ. The loss of dependency on the polar angle is due to integration, and would have likely been a factor in the dipole field.

Introducing combined $d\theta$- and $d\varphi$-perturbations to one of the particles within the surface of the sphere, will add a perturbation term with dependence of $d\theta$. The $d\varphi$ dependence vanishes in the integration. The results are recorded in Table 4.3. Even for perturbations along the entire sphere surface area, the resulting potentials only show a $d\theta$-dependency. In the quadrupole components, there is a recurring term of the form $\frac{\mathcal{R}_5}{(r_0-\epsilon)^3}$, which is scaled by some numerical factor. The system size r_0 is set to the size of N closely bundled electrons,

N	Monopole	Dipole	Quadrupole
2	$-\frac{2\epsilon}{4\pi(r_0-\epsilon)}$	0	$-\frac{\mathcal{R}_5}{32\pi(r_0-\epsilon)^3}(1+\cos(2d\theta))$
3	$-\frac{3\epsilon}{4\pi(r_0-\epsilon)}$	0	$-\frac{\mathcal{R}_5}{32\pi(r_0-\epsilon)^3}(2+\cos(2d\theta))$
4	$-\frac{4\epsilon}{4\pi(r_0-\epsilon)}$	0	$-\frac{\mathcal{R}_5}{64\pi(r_0-\epsilon)^3}(5+2\cos(2d\theta))$
5	$-\frac{5\epsilon}{4\pi(r_0-\epsilon)}$	0	$-\frac{\mathcal{R}_5}{32\pi(r_0-\epsilon)^3}(3+\cos(2d\theta))$
6	$-\frac{6\epsilon}{4\pi(r_0-\epsilon)}$	0	$-\frac{\mathcal{R}_5}{32\pi(r_0-\epsilon)^3}(3+\cos(2d\theta))$
7	$-\frac{7\epsilon}{4\pi(r_0-\epsilon)}$	0	$-\frac{\mathcal{R}_5}{32\pi(r_0-\epsilon)^3}(3+\cos(2d\theta))$
8	$-\frac{8\epsilon}{4\pi(r_0-\epsilon)}$	0	$-\frac{\mathcal{R}_5}{64\pi(r_0-\epsilon)^3}(9+\cos(2d\theta)+\sqrt{3}\sin(2d\theta))$
9	$-\frac{9\epsilon}{4\pi(r_0-\epsilon)}$	0	$-\frac{\mathcal{R}_5}{32\pi(r_0-\epsilon)^3}(6+\cos(2d\theta))$
10	$-\frac{10\epsilon}{4\pi(r_0-\epsilon)}$	0	$-\frac{\mathcal{R}_5}{32\pi(r_0-\epsilon)^3}(7+\cos(2d\theta))$
11	$-\frac{11\epsilon}{4\pi(r_0-\epsilon)}$	0	$-\frac{\mathcal{R}_5}{32\pi(r_0-\epsilon)^3}(9+\cos(2d\theta))$
12	$-\frac{12\epsilon}{4\pi(r_0-\epsilon)}$	0	$-\frac{\mathcal{R}_5}{32\pi(r_0-\epsilon)^3}(8+\cos(2d\theta))$

Table 4.3: *The field potentials of metastable, stiff configurations in dependence of perturbation of a conveniently chosen particle. In all listed cases, the potential does not differ with the particle experiencing the perturbation.*

roughly approximated to $r_0(N) = N^{\frac{1}{3}}a_0$ with particle number N and Bohr radius a_0. This is feasible, especially in an experimental setup, where the system size would generally be chosen to be larger. Importantly, all tetrahedral configurations share the same behavior under perturbation of a single monopole, which is expressed by an additional term with a $\cos(2d\theta)$-dependency. As such, a relaxation of the perturbation for the tetrahedral configurations all share the same oscillation frequency. Since the non-tetrahedral configuration of $N = 8$ is the only one that also generates a $\sin(2d\theta)$-dependecy, it stands to reason that the oscillation behavior of these cases depend primarily on the configuration's geometry.

4.3. Oscillation Frequencies as a Result of Single-Particle Perturbations

The relaxation of a tetrahedral configuration after the perturbation is uniformly an oscillation around a potential minimum with a spring constant k. Given a test charge Q,

$k(o,N) = q_e Q \dfrac{\mathcal{R}_5}{8\pi(r_0-\epsilon)^5 o^3}$, which can be classically translated into an oscillation frequency $\omega_{osc}(o,N,m) = \sqrt{\dfrac{k(o,N)}{m}}$. The expression for the spring constant is the result of taking the derivative of the potential with respect to $d\theta$, normalized by $(r_0-\epsilon)^2$. If ϵ is expressed as a fraction of r_0, then for cases of similar geometry, the spring constant is the same, as the dependency on the particle number cancels.

$$k = -\frac{q_e Q \mathcal{R}_5}{8\pi(r_0-\epsilon)^5 o^3} \tag{4.5}$$

$$= -\frac{q_e Q}{8\pi o^3}\left(1 - \frac{r_0^5}{(r_0-\epsilon)^5}\right). \tag{4.6}$$

Setting $\epsilon = \frac{2}{3} r_0$ will reduce the fraction on the right side of Equation 4.6 to a dimensionless constant and cancel the r_0-dependency.

$$k = -\frac{q_e Q}{8\pi o^3}\left(1 - \frac{r_0^5}{(r_0 - \frac{2}{3}r_0)^5}\right) \tag{4.7}$$

$$= -\frac{q_e Q}{8\pi o^3}\left(1 - \frac{r_0^5}{(\frac{1}{3}r_0)^5}\right) \tag{4.8}$$

$$= -\frac{q_e Q}{8\pi o^3}\left(1 - \frac{1^5}{(\frac{1}{3})^5}\right) \tag{4.9}$$

$$= -\frac{q_e Q}{8\pi o^3}\left(1 - 3^5\right). \tag{4.10}$$

The choice of ϵ however, is arbitrary, and were it fixed, then the leading-order terms of ω_{osc} would scale with $N^{\frac{1}{6}}$. To realize this, set $r_0 = a_0 N^{\frac{1}{3}}$ explicitly.

$$k = -\frac{q_e Q}{8\pi o^3}\left(1 - \frac{r_0^5}{(r_0-\epsilon)^5}\right), \tag{4.11}$$

$$\omega_{osc,\epsilon=const} = \sqrt{\frac{k}{m}} \tag{4.12}$$

$$= \sqrt{-\frac{q_e Q}{8\pi m o^3}\left(1 - \frac{r_0^5}{(r_0-\epsilon)^5}\right)} \tag{4.13}$$

$$= \sqrt{-\frac{q_e Q}{8\pi m o^3}\left(1 - \frac{a_0^5 N^{\frac{5}{3}}}{(a_0 N^{\frac{1}{3}}-\epsilon)^5}\right)}. \tag{4.14}$$

Expanding ω around $N = 0$ reveals a leading-order term of

$$\omega_{osc,\epsilon=const} = \sqrt{\frac{q_e Q}{8\pi o^3}\frac{5\epsilon N^{\frac{1}{3}}}{a_0 m}}. \tag{4.15}$$

This dependency on N will be taken as the actual scaling behavior for large particle numbers, but for consistency reasons in later chapters, the (initial) distance between monopoles and droplet boundary, ϵ is chosen to be two thirds of r_0 in the computations from here on out.

N	ω_{osc}[eV]	ω_{osc}[Hz]	Oscillation Period τ_{osc}[s]
2	1.169×10^{-8}	2.827×10^{6}	2.223×10^{-6}
3	1.169×10^{-8}	2.827×10^{6}	2.223×10^{-6}
4	1.169×10^{-8}	2.827×10^{6}	2.223×10^{-6}
5	1.169×10^{-8}	2.827×10^{6}	2.223×10^{-6}
6	1.169×10^{-8}	2.827×10^{6}	2.223×10^{-6}
7	1.169×10^{-8}	2.827×10^{6}	2.223×10^{-6}
8	0.827×10^{-8}	1.999×10^{6}	3.143×10^{-6}
9	1.169×10^{-8}	2.827×10^{6}	2.223×10^{-6}
10	1.169×10^{-8}	2.827×10^{6}	2.223×10^{-6}
11	1.169×10^{-8}	2.827×10^{6}	2.223×10^{-6}
12	1.169×10^{-8}	2.827×10^{6}	2.223×10^{-6}

Table 4.4: *The characteristic frequencies of a perturbed monopole relaxing toward its energy minimum. It's assumed that the monopole oscillates independently from the other ones, and the coupling of each particle as an individual oscillator is ignored in this approximation. This characteristic frequency can be converted to a zero-point energy of each particle, which then gives a basis for fermionic quantized energy levels. The irregularity of the $N = 8$ case results in a reduced ω_{osc}.*

Since the resulting oscillation can be approximated as a harmonic oscillation, and because

the system is quantum in nature, there appears to be a contribution of a quantum harmonic oscillator. As the oscillation frequency is knowable as per Table 4.4, so are the quantized oscillation energies. Crucially, this introduces a zero-point oscillation energy $\frac{1}{2}\hbar\omega_{osc}$. This stands in relation to the rest-mass energy contained within the system, easily determined in dimensionless variables as $N \times m_0$. The small ratio of zero-point energy and rest mass energy as seen in the rightmost column of Table 4.5 suggests that, using conventional diagnostics, the zero-point oscillation of a monopole is unlikely to be measured.

N	$\frac{1}{2}\hbar\omega_{osc}$ [eV]	Nm_0 [eV]	$\frac{\frac{1}{2}\hbar\omega_{osc}}{N \times m_0}$
2	5.845×10^{-9}	1.022×10^{7}	5.720×10^{-16}
3	5.845×10^{-9}	1.533×10^{7}	3.813×10^{-16}
4	5.845×10^{-9}	2.044×10^{7}	2.860×10^{-16}
5	5.845×10^{-9}	2.555×10^{7}	2.288×10^{-16}
6	5.845×10^{-9}	3.066×10^{7}	1.907×10^{-16}
7	5.845×10^{-9}	3.577×10^{7}	1.634×10^{-16}
8	4.133×10^{-9}	4.088×10^{7}	1.011×10^{-16}
9	5.845×10^{-9}	4.599×10^{7}	1.271×10^{-16}
10	5.845×10^{-9}	5.110×10^{7}	1.144×10^{-16}
11	5.845×10^{-9}	5.621×10^{7}	1.040×10^{-16}
12	5.845×10^{-9}	6.132×10^{7}	0.953×10^{-16}

Table 4.5: *Ratio of the oscillation energy and the rest-mass energy for each particle number. The deconfining phase zero-point energy introduces a small, but noticeable offset in the expected plasma droplet energy. The $N = 8$ case has a notably smaller zero-point energy offset, likely a product of its irregular geometry and the weaker potential.*

5

Penning Traps

A fused electron droplet is effectively a one-component plasma. To observe this plasma, a capture method is required that doesn't affect the individual charge carriers in the ensemble in unequal ways, thus distorting the configuration. The usual approach involves the use of field traps.

Among quadrupole traps, there are commonly Penning traps and Paul traps. Paul traps are constructed to hold particles steadily in one position, but their construction is heavily dependent on precisely oscillating electric fields, which, due to the natural shortcomings of such constructions will carry significant inaccuracies. This is due to the principles of the Earnshaw theorem (subsection A.5.1), which states that point charges can't be held in equilibrium by their electrostatic interactions alone. Penning traps are built by two hyperboloid electrodes inducing spiral fields, which act like a quadrupole field. This forces the particles into typically small-radius cyclotronic motions, with slow circular magnetron drift motion. The full trajectory resembles a spiral along the surface of a torus. Penning traps hold charged particles in largely stable orbits, but as the trapped monopole crystal is not stationary, the Penning trap's operation is unimpeded by the Earnshaw theorem.

5.1. An Adiabatically Approximated Application of Penning Trap Equations

A few approximations precede the application of the analytic solution for the motion of a metastable monopole crystal in a Penning trap. The monopole crystal's total charge is contingent on the monopole's distance to the phase boundary as a result of the mirror charge construction (Figure 2.3). This change of charge over time will heavily affect the frequency, but for a first approximation, a static average of the charge will suffice. The initial

monopole charge is taken to be that of an electron as defined by Yang-Mills thermodynamics $q = q_e + q'_e = \frac{4\pi}{e}\cos(30°) + \frac{4\pi}{e}\cos(30°)\frac{r_0}{r_0-\epsilon}$ at a third of the droplet's radius [**1**]. If the periods associated with all trap frequencies are significantly larger than the lifetime of the system, this adiabatic approximation is sufficient to make predictions for an observation. Typical decay rates that result exclusively from radiation as a result of the circular acceleration of charged particles in Penning traps are on the time scale of years.

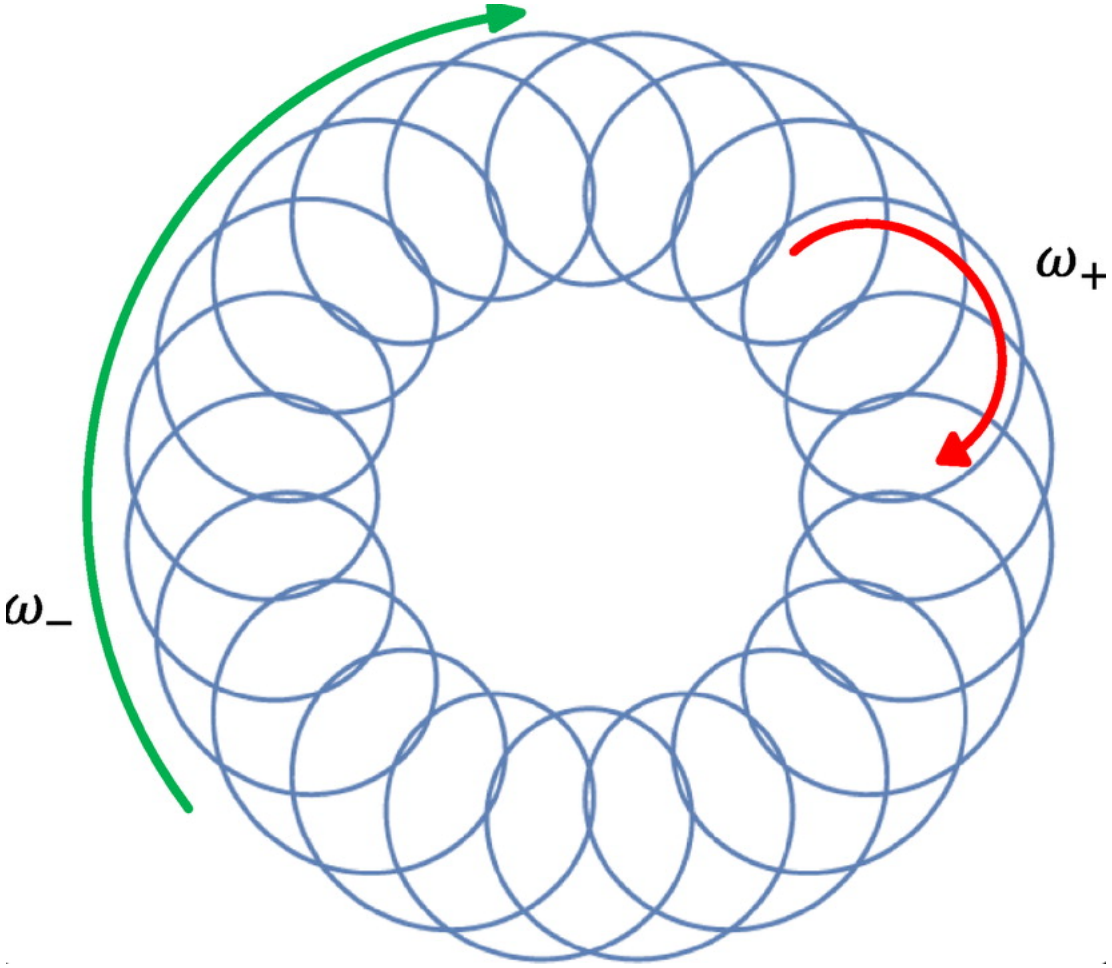

Figure 5.1: *A qualitative visualisation of a single particle's trajectory in a Penning trap as depicted in [**10**], Fig. 1 Typically, the magnetron frequency ω_- is much smaller than the modified cyclotron frequency ω_+, leading to a spiral around the surface of a torus. The cyclotron frequency ω_c is the sum of ω_- and ω_+. The expansion of the radius due to radiative losses are typically small enough so that the impreciseness introduced by the change of trajectory can be ignored. This characteristic is also important for the stiffness expected of the monopole crystals, as they each gain their own trajectory in the Penning trap. For the monopole crystal to reach the trap boundary, it takes about* 2×10^4 s*, which translates to between 5 and 6 hours.*

To create the electric quadrupole potential, the Penning trap typically uses two end-cap electrodes and a ring electrode, equidistant to the other two. The end-cap electrodes may optionally include an opening for the particle injection and diagnostic functions, along the

trap's axis. Due to the construction of the trap, scattering on the center electrode would bounce the particle onto their trapped (closed) trajectory (Figure 5.1). In [**9**] the trap deployed ring-electrodes at a distance of $d_{Penning} = 3$ mm as end-caps. The radius of the electrodes is also chosen to be $R_{Penning} = 3$ mm (Figure 5.2). The potential well created by the Penning trap in this experiment identifies a ratio of voltage and magnetic field strength, that enables the formation of spherical configurations, while the voltage $V_{Penning}$ is variable between 500 V and 10 kV, and the magnetic field strength $B_{Penning}$ is variable between 0.05 T and 0.22 T. We will use similar trap parameters for further approximations, while adhering to the definition of V_0 given in [**9**],

$$V_{Penning} = V_0 = \frac{q_{Penning} B_{Penning}^2 R_{Penning}^2}{8 m_e}, \tag{5.1}$$

$$B_{Penning} = 0.22T \Rightarrow V_0 \approx 6707.52 \text{ V}, \tag{5.2}$$

While outside the original trap's voltage capabilities, this lies comfortably within the range of high-voltage electricity supply. The resulting axial motion becomes that of a simple harmonic

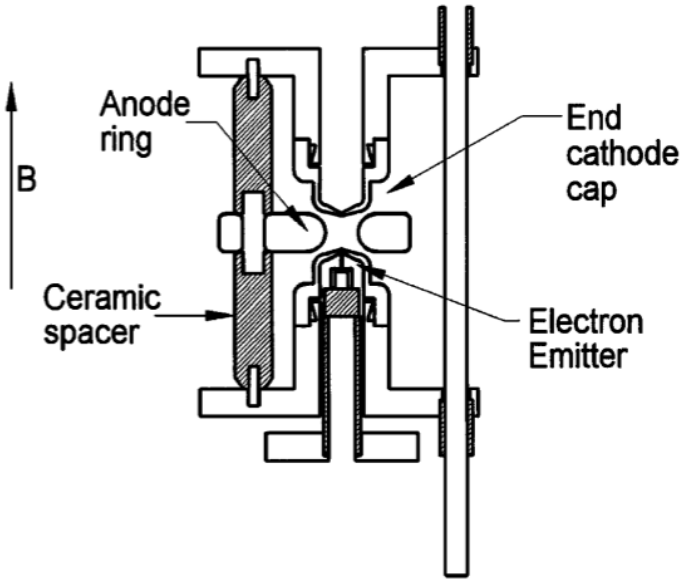

Figure 5.2: *An example schema of a Penning trap in the experiment constructed in [**9**], FIG 1.*
The three electrodes are suspended along the z-axis, and connected by non-conductive spacers. Both of the end cathodes are pierced through the center. A particle emitter is placed near the injection hole in the lower cathode. The hole in the upper electrode enables diagnostics.

oscillation, and the magnetron motion derives easily from the Lorentz force. As the relevant object is the stable configuration of monopoles, it is necessary for the configurations to enter

the Penning trap as they are, and all monopoles to move as a stiff configuration. This, in itself is a non-trivial problem. However, once inserted, each particle of the configuration travels at the same cyclotron frequency around the trap's axis. It travels along two circular trajectory with the damping constant $\gamma_c = \frac{4\omega_c^2}{3m_e}$ modelling the loss of energy due to cyclotron radiation. At this point, the monopole crystal can be effectively viewed as a single point particle. These details are ignored in this thesis, and instead the entire droplet is immediately viewed as a single particle for the purposes of its Penning trap trajectory. The cyclotron frequency ω_c and the axial frequency ω_z are defined through the total charge and mass of the fused electron droplet.

$$\omega_c = \frac{|q_{Penning} \cdot B_{Penning}|}{m_e}, \tag{5.3}$$

$$\omega_z = \sqrt{\frac{q_{Penning}}{m_e d_{Penning}} V_0} \tag{5.4}$$

$$= \sqrt{\frac{q_{Penning}}{m_e d_{Penning}} \frac{q_{Penning} B_{Penning}^2 R_{Penning}^2}{8m_e}}. \tag{5.5}$$

The cyclotron radius of a single particle's motion develops very slowly in comparison to the timescale of the configuration's lifetime. It can be determined by solving the differential equation

$$\rho''(t) = -\omega_c \rho'(t) - \frac{\omega_z^2 \rho(t)}{2} = 0. \tag{5.6}$$

Equation 5.6 is a second order linear ordinary differential equation, and solves to

$$\rho(t) = c_1 e^{-\frac{t}{2}(\sqrt{\omega_c^2 - 2\omega_z^2} + \omega_c)} + c_2 e^{\frac{t}{2}(\sqrt{\omega_c^2 - 2\omega_z^2} - \omega_c)}, \tag{5.7}$$

$$\rho(0) = 0.001 \text{ m}, \tag{5.8}$$

$$\rho'(0) = 0 \frac{\text{m}}{\text{s}}, \tag{5.9}$$

where the coefficients evaluate to $c_2 = 0.001 - c_1$ and $c_1 = \frac{0.001(\sqrt{\omega_c^2 - 2\omega_z^2} - \omega_c)}{2\sqrt{\omega_c^2 - 2\omega_z^2}}$. At short timescales, the cyclotron radius can be assumed to be effectively static.

5.2. Application of Experimental Parameters

For this trap, assume the configuration begins at rest, and the starting position is at $\rho_{Penning}(t = 0) = \frac{R_{Penning}}{3} = 1$ mm. The particle number should scale directly with the occurrences of mass and charge factors in the definitions of the optimal voltage. As a result, all frequencies only depend on the ratio between the two, which cancels the particle number contribution [**10**]. This is a convenient trait for the observation of the monopole crystal's motion. Using the above parameters, the cyclotron frequency is about $\omega_c = 2.710 \times 10^{10}$ Hz, and axial frequency is about $\omega_z = 5.248 \times 10^8$ Hz. This translates into oscillation periods of $\tau_{c,Penning} = 2.319 \times 10^{-10}$ s and $\tau_{z,Penning} = 1.197 \times 10^{-8}$ s. This can be verified through Listing A.10. Through Figure 5.3, it can be verified that the change in the cyclotron radius is negligible at the timescales considered throughout this thesis.

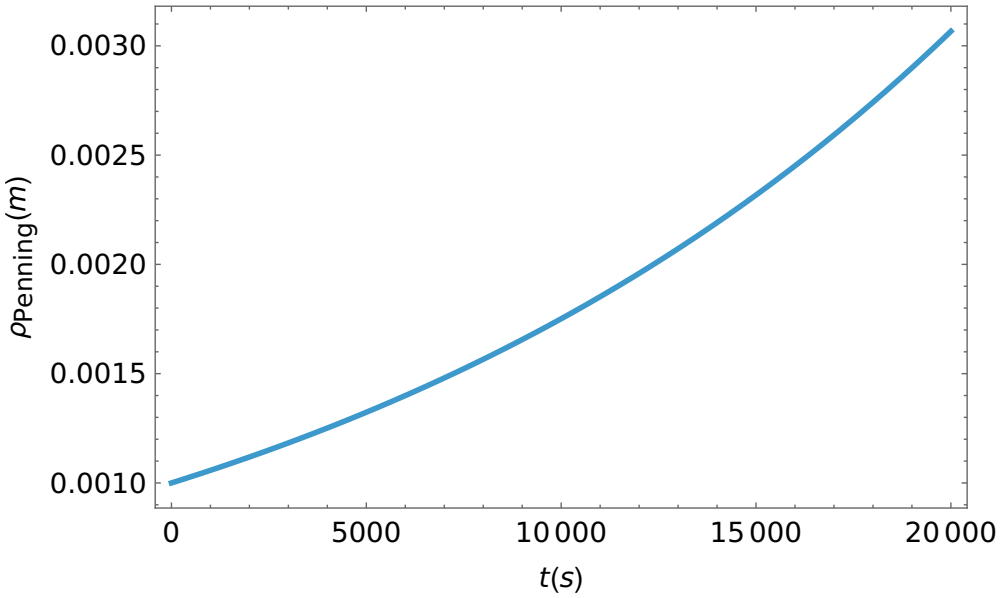

Figure 5.3: *The development of the cyclotron-radius in meters (y-axis), over seconds (x-axis) of a configuration with particle charges and masses of a single particle with the charge-mass ratio of an electron in a Penning trap. The curve is extracted from the analytic solution of the radial equation of motion for particles in a Penning trap given the parameters* $B_{Penning} = 0.22$ T, $V_0 = 6707.52$ V, $R_{Penning} = 3$ mm, *assuming the initial particle radius is equal to* $\frac{1}{3}R_{Penning}$, *and mapped over 100 seconds. The radius after this time is still far from reaching the trap's edges.*

6

Collective Radial Motion

6.1. Neutralisation Time

Assuming the monopoles' initial positions are uniformly at $r(t = 0) = \frac{1}{3}r_0$, they each experience the same outward acting force as a consequence of the mutual Coulomb potential. This force can be derived directly from the potentials measured by the observer particle (Table 4.4), used to obtain an expression for the change of the distance between monopole and system boundary ϵ, and with it, the neutralisation time. The closer the monopoles approach the droplet's boundary, their charges would be observed as decreasing (Figure 6.2). As the monopoles cross the phase boundary, it transitions into the surrounding condensate. At macroscopic timescales, the condensate must be neutrally charged, and conserve mass (or rather, energy). This posits that as the monopoles cross into the condensate, their mass and charge are screened out, which is supported by the way the gauge coupling diverges. The normalization relates charge with the inverse gauge coupling $e(\lambda)$, which diverges at low temperatures as can be seen in Figure 2.2.

To model the neutralisation of the droplet as the monopoles are pressed into its periphery, the Coulomb repulsion acting on the monopole is isolated as the sole contribution to the radial motion. The radial coordinate r is represented by the distance between particle and the edge of the droplet $\epsilon = r_0 - r$. The resulting differential equation is solved numerically, and the first (and, by construction of the potential, only) position at which $\epsilon = 0$ is identified (Table 6.1). There, the monopole reaches the phase boundary (Figure 6.1).

$$F(\epsilon) = -\nabla U = -\partial_\epsilon U, \tag{6.1}$$

$$F(\epsilon) = m \times \ddot{\epsilon}, \tag{6.2}$$

$$\Rightarrow \ddot{\epsilon} = \frac{F(\epsilon)}{m} = \frac{-\partial_\epsilon U}{m}. \tag{6.3}$$

Solving the differential equation will yield an expression for the motion of $\epsilon(t)$, which can be

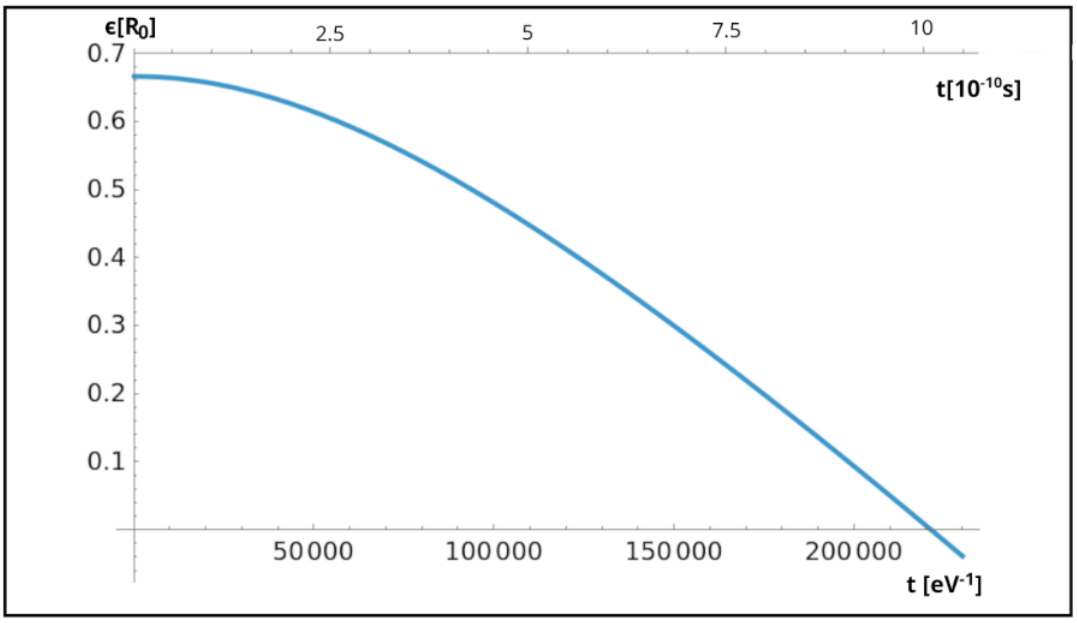

Figure 6.1: *The development of the particle distance from the boundary ϵ in units of r_0 on the x-axis against the time in eV^{-1} on the y-axis. The second y-axis gives τ_{ne} in seconds. After hitting $\epsilon = 0$, the monopole's mass and charge are screened out as they cross into the confined phase. As such, the radial development is expected to change qualitatively beyond $\epsilon = 0$, as fundamentally, they do not experience the force exerted by the Coulomb potential anymore. The dynamics beyond $\epsilon = 0$ are better modeled through a different, statistical approach.*

inserted back into the potential for the mirror charge construction. Because the total charge of the droplet is determined through the mirror-charge method, the force acting on the observer charge decreases as the monopoles approach the phase boundary. This is easily confirmed by determining the total charge of a charge and mirror charge pair:

N	Neutralisation Time $\tau_{ne}[\mathrm{eV}^{-1}]$	Neutralisation Time $\tau_{ne}[\mathrm{s}]$
2	221402	9.156×10^{-10}
3	193413	7.999×10^{-10}
4	175727	7.267×10^{-10}
5	163130	6.746×10^{-10}
6	153512	6.349×10^{-10}
7	145823	6.031×10^{-10}
8	139475	5.768×10^{-10}
9	134105	5.546×10^{-10}
10	129477	5.355×10^{-10}
11	125428	5.187×10^{-10}
12	121842	5.039×10^{-10}

Table 6.1: *The neutralisation time τ_{ne} of each monopole crystal in isolation, determined by Coulomb repulsion pushing the monopoles into the droplet's preconfined boundary. Generally the neutralisation times decrease with increasing particle numbers.*

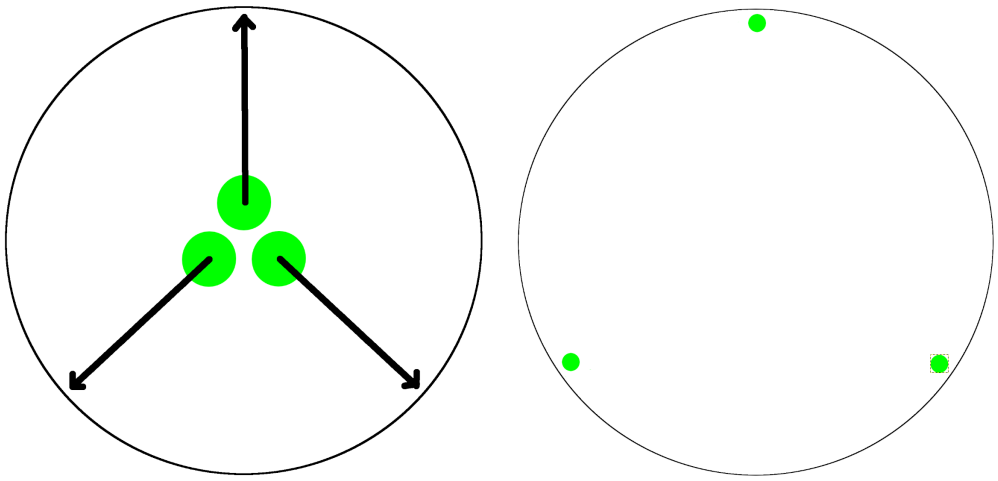

Figure 6.2: *A visualisation of the neutralisation process for $N = 3$. The green spheres represent the monopoles, all with equal charge. The size of the sphere represents the charge magnitude, although it's not to scale. The arrows indicate the force and the direction it acts toward. The closer the monopoles move toward the phase boundary, the smaller the charge contributions observable from outside the droplet becomes.*

$$\lim_{\epsilon\to 0} U = \lim_{\epsilon\to 0} \frac{q_e}{\sqrt{\frac{1}{o^2} + (r_0-\epsilon)^2 - \frac{2}{o}(r_0-\epsilon)\sin\varphi\cos\theta}} - \frac{q_e \frac{r_0}{r_0-\epsilon}}{\sqrt{\frac{1}{o^2} + \left(\frac{r_0^2}{r_0-\epsilon}\right)^2 - \frac{2}{o}\frac{r_0^2}{r_0-\epsilon}\sin\varphi\cos\theta}} \tag{6.4}$$

$$\overset{\epsilon\to 0}{=} \frac{q_e}{\sqrt{\frac{1}{o^2} + r_0^2 - \frac{2}{o}r_0\sin\varphi\cos\theta}} - \frac{q_e \frac{r_0}{r_0}}{\sqrt{\frac{1}{o^2} + \left(\frac{r_0^2}{r_0}\right)^2 - \frac{2}{o}\frac{r_0^2}{r_0}\sin\varphi\cos\theta}} \tag{6.5}$$

$$= \frac{q_e}{\sqrt{\frac{1}{o^2} + r_0^2 - \frac{2}{o}r_0\sin\varphi\cos\theta}} - \frac{q_e}{\sqrt{\frac{1}{o^2} + r_0^2 - \frac{2}{o}r_0\sin\varphi\cos\theta}} \tag{6.6}$$

$$= 0. \tag{6.7}$$

Due to this, the development of charge as the monopoles transition into the condensate is a continuous one. Since the monopoles are decoupled in confined phase, their charge doesn't become observable again after crossing through the preconfining boundary and into confined phase.

6.2. Mirror Charge Neutralisation at Plasma Phase Boundary

Having identified the radial motion as a function of time, this, along with the parameters chosen for the Penning trap in chapter 5, can be used in Equation 2.20 for the mirror charge construction in section 2.2 to determine the time-dependent development of the system's total charge. Due to the small timescales of the process triggering underflow errors in numerical computation when handling exponential functions, polynomial approximations have been used for the radial function instead (Table 6.2). From these polynomials the behavior of the droplet's total charge over time is determined (Figure 6.3).

Another sensible approximation would be choosing a function of the form $\gamma - e^{-\alpha x+\beta}$ where α, β and γ are some coefficients, however, without applying unfounded assumptions, finding a fit for this function is computationally problematic, while only providing minimal qualitative improvement in root accuracy, which at the timescales in question will likely be within the error margins of any proposed experiment. When ϵ is switched out for its time-dependent analog $\epsilon(t)$, the full charge development can be determined by inserting it back into the full potential obtained from the multipole expansion in Table 4.2.

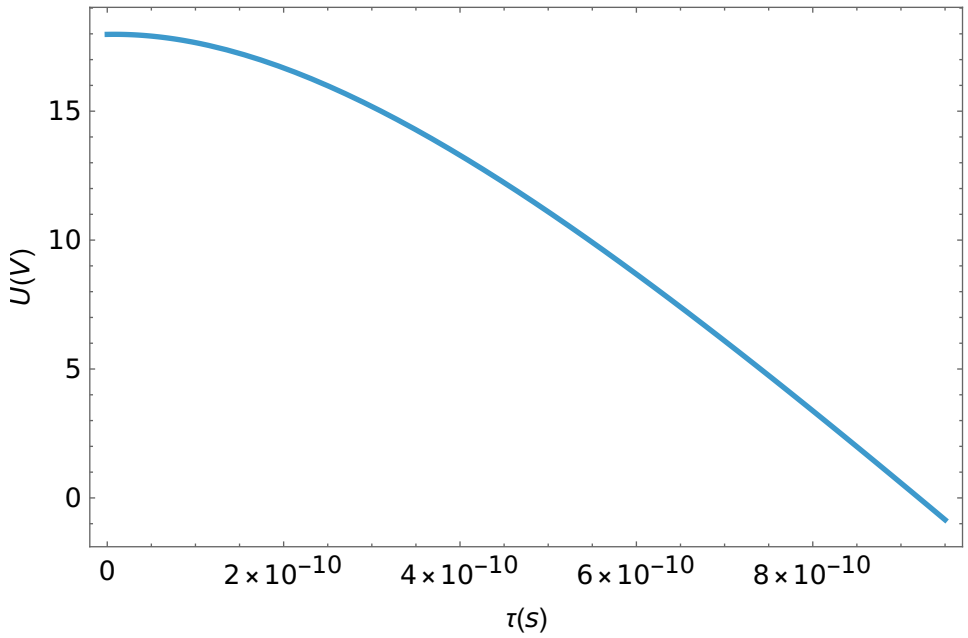

Figure 6.3: *The electric potential of the monopole crystal in the Penning trap with respect to time in eV^{-1} as measured by the Penning trap's electrode. This graph belongs to the $N = 2$ case.*

The assumption can be made that for sufficiently large N, the fused droplet behaves adiabatically in the Penning trap, as its lifetime decreases with increasing particle numbers, while the Penning trap oscillations are determined by the fields of the trap. At macroscopic particle

N	$\epsilon(t[\mathrm{eV}^{-1}])$
2	$\frac{2}{3} + 1.054 \times 10^{-7} t - 2.659 \times 10^{-11} t^2$ $+8.586 \times 10^{-17} t^3 - 1.621 \times 10^{-22} t^4 + 1.429 \times 10^{-28} t^5$
3	$\frac{2}{3} + 7.679 \times 10^{-8} t - 3.331 \times 10^{-11} t^2$ $+1.072 \times 10^{-16} t^3 - 1.489 \times 10^{-22} t^4 + 5.238 \times 10^{-30} t^5$
4	$\frac{2}{3} + 9.663 \times 10^{-8} t - 4.144 \times 10^{-11} t^2$ $+1.583 \times 10^{-16} t^3 - 3.233 \times 10^{-22} t^4 + 2.667 \times 10^{-28} t^5$
5	$\frac{2}{3} - 2.807 \times 10^{-7} t - 2.872 \times 10^{-11} t^2$ $-1.619 \times 10^{-16} t^3 + 2.336 \times 10^{-21} t^4 - 7.109 \times 10^{-27} t^5$
6	$\frac{2}{3} + 5.897 \times 10^{-8} t - 5.187 \times 10^{-11} t^2$ $+1.976 \times 10^{-16} t^3 - 2.599 \times 10^{-22} t^4 - 2.673 \times 10^{-27} t^5$
7	$\frac{2}{3} + 5.448 \times 10^{-8} t - 5.696 \times 10^{-11} t^2$ $+2.166 \times 10^{-16} t^3 - 2.003 \times 10^{-22} t^4 - 6.906 \times 10^{-28} t^5$
8	$\frac{2}{3} + 5.059 \times 10^{-7} t - 7.293 \times 10^{-11} t^2$ $+3.825 \times 10^{-16} t^3 - 1.165 \times 10^{-21} t^4 + 1.596 \times 10^{-27} t^5$
9	$\frac{2}{3} + 9.153 \times 10^{-8} t - 6.883 \times 10^{-11} t^2$ $+3.115 \times 10^{-16} t^3 - 5.837 \times 10^{-22} t^4 - 6.472 \times 10^{-29} t^5$
10	$\frac{2}{3} + 5.450 \times 10^{-7} t - 8.462 \times 10^{-11} t^2$ $+4.781 \times 10^{-16} t^3 - 1.569 \times 10^{-21} t^4 + 2.315 \times 10^{-27} t^5$
11	$\frac{2}{3} - 4.520 \times 10^{-8} t - 5.596 \times 10^{-11} t^2$ $+8.088 \times 10^{-17} t^3 + 1.447 \times 10^{-21} t^4 - 6.693 \times 10^{-27} t^5$
12	$\frac{2}{3} + 9.950 \times 10^{-8} t - 8.366 \times 10^{-11} t^2$ $+4.252 \times 10^{-16} t^3 - 9.661 \times 10^{-22} t^4 + 2.923 \times 10^{-28} t^5$

Table 6.2:
A polynomial interpolation for the evolution of ϵ for each monopole crystal, describing the motion of the monopoles as they are driven toward the droplet's periphery.

numbers, τ_{ne} will have dropped orders of magnitude below the periods for any oscillations that the droplet experiences in the Penning trap, and the mass/charge ratio of the particles within it. As the mass of the monopoles doesn't change when the charge drops, the trajectory of the monopole crystal in the Penning trap is expected to change over time. As the charge decreases, ω_c decreases proportionally to it, and ω_z decreases proportionally to its square root. However, assuming an adiabatic approximation in which $\tau_{ne} \ll \omega_c, \omega_z$, this effect can be ignored.

7

Characteristic Blob Frequencies of Monopole Crystals

7.1. Blob Evaporation Time

A plasma droplet is expected to radiate particles, depending on its constituents. Its behavior is analogous to the evaporation of a liquid droplet. The evaporation time τ_{evap} for a droplet of charged leptons is given primarily by the droplet radius r_0 and the particle current J_H that describes the number of particles radiated off the droplet's surface in some timespan. Since the monopole crystal exists as a product of fused electrons, it stands to reason that the droplet's lifetime as dictated by plasma-physics should stand in relation to the other relevant timescales. In an ideal scenario, this evaporation time τ_{evap} is orders of magnitude larger than the neutralisation time. The particle current through the droplet's surface is a sum of J_0 for the photon contribution and J_1 for the electron neutrino contribution of the radiation. The evaporation time τ_{evap} constitutes effectively a different form of lifetime for the fused electron droplet in the Penning trap, though observations of τ_{ne} would of course point toward a novel neutralisation process and are thus more interesting. The neutralisation process would only be observable, if $\tau_{ne} \geq \tau_{evap}$. The formulas for computation of the breathing frequency are sourced from [**13**]. Because the radiation process only occurs outward from the preconfined boundary, into the confined phase surroundings, the formulas are evaluated at Hagedorn temperature, at which the transition toward the confined phase occurs.

$$r(t) = r_0 - \frac{J(T_H)}{\rho_H} t, \tag{7.1}$$

$$\rho_H = 4\pi\Lambda^3 T_H, \tag{7.2}$$

$$J_l(T_H) = M_l \int_0^\infty dp \frac{1}{2\pi^2} p^3 n_{m_l}(p, T_H), \tag{7.3}$$

$$J(T) = J_0(T) + J_1(T). \tag{7.4}$$

Solving for t, given $r(t) = 0$ gives the time τ_{evap} at which the plasma droplet is exactly evaporated.In the expression for the particle current, the coefficient M_l is dependent on the particle species and is a product of its spin- and charge degeneracy. The current is integrated over the modulus on the spatial on-shell momentum p. As the droplet consists only of electrons, it only radiates off neutrinos and photons during the evaporation process. M_l is 2 for neutrinos and photons. The particle current uses the appropriate distribution function $n_{m_l}(p, T_H)$, which is either Fermi-statistics $n_{F,m_l}(p, T_H) = \frac{1}{\exp\left(\frac{\sqrt{p^2+m_l^2}}{T_H}\right)+1}$ for electron-neutrinos, or Bose-statistics $n_{B,m_l}(p, T_H) = \frac{1}{\exp\left(\frac{p}{T_H}\right)-1}$ for photons.

$$0 = r_0 - \frac{J(T_H)}{\rho_H} \tau_{evap}, \tag{7.5}$$

$$\Rightarrow \tau_{evap} = r_0 \frac{\rho_H}{J(T_H)}. \tag{7.6}$$

N	$r_0[m]$	Evaporation Time $\tau_{evap}(T_H)$[s]
2	2.702×10^{-10}	2.165×10^{-19}
3	3.093×10^{-10}	2.478×10^{-19}
4	3.404×10^{-10}	2.727×10^{-19}
5	3.667×10^{-10}	2.938×10^{-19}
6	3.897×10^{-10}	3.122×10^{-19}
7	4.102×10^{-10}	3.286×10^{-19}
8	4.289×10^{-10}	3.436×10^{-19}
9	4.461×10^{-10}	3.574×10^{-19}
10	4.620×10^{-10}	3.701×10^{-19}
11	4.769×10^{-10}	3.821×10^{-19}
12	4.910×10^{-10}	3.933×10^{-19}

Table 7.1: *Evaporation times for typical one-component electron plasma droplets of the expected size of the fused electron droplets at Hagedorn temperature.*

According to Table 7.1, at Hagedorn temperature, the evaporation time of the plasma droplet is expected to be significantly lower than the neutralisation time τ_{ne}.

7.2. Plasma Breathing Frequency

The radii of plasma droplets are not generally stable, even without the consideration of plasma evaporation. Rather, they oscillate around some mean value. This *plasma breathing* phenomenon is due to the ensemble pressure, charge, and particle contributions. The roughest thermodynamic approximation for a fused electron plasma should take into account the distortion of the temperature that the oscillation introduces. The oscillation is spherically symmetric and does not shift the location of the droplet. The plasma breathing frequency for Yang-Mills one-component plasma droplets with homogeneous energy densities and pressures at temperatures close to its Hagedorn temperature is identified in [**14**]. This frequency is a quantity determined by the normalized plasma-ball radius $\bar{r}_0 = r_0\Lambda$.

$$\Omega_0 = \frac{\pi c_s \Lambda}{\bar{r}_0}. \tag{7.7}$$

It uses c_s as a longitudinal sound velocity, which can be obtained by relating the density and pressure with the (dimensionless) temperature, and can be treated as constant. Density and pressure are assumed constant over the droplet's radius and temperature. Λ is the Yang-Mills scale of the constituents forming the plasma, and hence also a constant. When dividing out Λ, the system size r_0 can be used directly as defined in section 2.2, and the constants can be shortened into a flat constant of 1.506 ([**14**], Eq. 20).

$$\Omega_0 = \frac{1.506}{r_0}. \tag{7.8}$$

This lowest mode of plasma breathing has frequencies of the timescale 10^{18} Hz (Table 7.2). Ω_0 is considered the dominant plasma breathing mode. Higher order modes tend to have

N	$\Omega_0[\mathrm{eV}^{-1}]$	$\Omega_0[\mathrm{Hz}]$	τ_{Ω_0}
2	2.800×10^4	6.771×10^{18}	9.280×10^{-19}
3	2.447×10^4	5.915×10^{18}	1.062×10^{-18}
4	2.223×10^4	5.374×10^{18}	1.169×10^{-18}
5	2.064×10^4	4.989×10^{18}	1.259×10^{-18}
6	1.942×10^4	4.695×10^{18}	1.338×10^{-18}
7	1.845×10^4	4.460×10^{18}	1.409×10^{-18}
8	1.764×10^4	4.266×10^{18}	1.473×10^{-18}
9	1.696×10^4	4.101×10^{18}	1.532×10^{-18}
10	1.638×10^4	3.960×10^{18}	1.587×10^{-18}
11	1.587×10^4	3.836×10^{18}	1.638×10^{-18}
12	1.541×10^4	3.726×10^{18}	1.686×10^{-18}

Table 7.2: *A rough estimate of the radially symmetric oscillation of the monopole crystals as a Yang-Mills plasma ball. The assertions for the droplet's temperature, pressure and density can be assumed true, once the monopoles have enough space for their later collective radial motion and the droplet's charge neutralisation. These values are determined for their initial, maximal radius.*

higher frequencies and lower amplitudes and their effects are ignored in the scope of this thesis. The amplitudes have been ignored in this consideration. The resulting oscillation period is of a similar timescale as the evaporation time τ_{evap}. The breathing frequency Ω_0 decreases with $N^{-\frac{1}{3}}$, so even though at these small particle numbers, the oscillation period is several orders of magnitude shorter than the neutralisation time τ_{ne}, their values might intersect at macroscopic N.

7.3. Frequency Comparison

Having gathered several frequencies and prospective lifetimes, one should compare these quantities. It formally confirms for which N the adiabatic approximation is a valid approach, and it also serves to characterize the behavior of the system for further examination, such as higher order radially symmetric oscillations. A brief overview of these timescales is provided in Table 7.3.

All oscillation frequencies are several orders of magnitude larger than either neutralisation time or evaporation time. The Penning trap's oscillation periods are dictated by the ratio of

Timescale Type	Timescale[s]	N-dependence
Monopole Oscillation Period τ_{osc}	10^{-6}	$N^{-\frac{1}{6}}$
Neutralisation Time τ_{ne}	10^{-10}	Decreasing Irregularly
Plasma Blob Evaporation Time τ_{evap}	10^{-19}	$N^{\frac{1}{3}}$
Lowest Order Breathing Period τ_{Ω_0}	10^{-18}	$N^{-\frac{1}{3}}$
Penning trap Cyclotron Period $\tau_{c,Penning}$	10^{-10}	None
Penning trap Axial Period $\tau_{z,Penning}$	10^{-8}	None
Penning trap Lifetime $\tau_{Penning}$	10^{4}	None

Table 7.3: *A comparison of the timescales that characterize monopole crystals, along with their scaling behavior with the particle number N.*

charge and mass, which does not change with particle number. There is a concrete upper limit of particles at which the adiabatic approximation is valid for the spatial confinement given by the Penning trap. The Penning trap frequency can instead be increased by applying stronger external fields. Both the cyclotron frequency and the axial frequency increase linearly with the external magnetic field. Up to $N = 12$, the Penning trap frequencies are of similar timescales as the neutralisation time, so assuming oscillation periods significantly larger than the neutralisation time, the system can be approximated adiabatically.

Whether the lowest order oscillations interact meaningfully with the neutralisation time depends also on the amplitude of the oscillation, which can be assumed small in comparison to the full droplet at macroscopic scales.

The droplet's evaporation time τ_{evap} is several orders of magnitude shorter than the neutralisation time τ_{ne}. The shorter of the two sets the system's de-facto lifetime in the Penning trap. For small N, this would be τ_{eva}. However, the approximate droplet's evaporation time increases with $N^{\frac{1}{3}}$. Assuming the neutralisation time stays at similar timescales (it actually decreases, but not according to any mathematical law that is apparent from the twelve data-points that were determined in this thesis), τ_{evap} is projected to cross over with the neutralisation time τ_{ne} at 10^{27} particles. This is larger than Avogadro's number at about 10^{23}, which would constitute a macroscopic ensemble, but it would be about the number of electrons that could fit inside a litre at cold temperatures $\left(\frac{0.001\ \mathrm{m}^3}{a_0^3} \approx 6.748 \times 10^{27}\right)$. Beyond this, at large N, τ_{evap} should increase even beyond the dependency of $N^{\frac{1}{3}}$, because only the particles on the surface of the droplet can contribute to the neutrino- and photon-radiation, so the vast majority of particles in the droplet won't contribute to the current $J(T_H)$.

The monopole oscillation is likely invisible to a process lasting one neutralisation time period, due to its long oscillation period. The droplet's radius could be assumed effectively

constant. It does decrease slower than the lifetimes, though at larger N, this might change. For Avogadro's number, τ_{osc} would be at a timescale of about 10^{-10}, which is still longer than the evaporation time at about 10^{-11}. The particle numbers would have to be much larger than Avogadro's number to observe this oscillation properly.

8

Discussion

8.1. Laser-Pumping Nanowires into High Particle Density Plasma

The requirements for achieving electron fusion, and thus the formation of the monopole crystals, are a high temperature and particle density. These requirements translate into an external energy density of $\frac{T_c}{\frac{4}{3}\pi a_0^3}$.

$$\frac{T_c}{\frac{4}{3}\pi a_0^3} = \frac{8 \text{ keV}}{\frac{4}{3}\pi(4.268 \times 10^{-5} \text{ eV}^{-1})^3} = 2.457 \times 10^{16} \frac{\text{J}}{\text{m}^3}. \tag{8.1}$$

In a laboratory setting, energy densities of 10^{16}J m^{-3} are difficult to achieve. However, a research team has designed a reliable method to generate energy densities of at least 10^{16}J m^{-3} = 10^{10}J cm^{-3} with some uniformity, and is projected to reach the required energy densities [**15**]. In concept, their experiment utilizes parallel grown nanowires consisting of metals with notably different absorption spectra, grown closely together on a wafer. The metal chosen on the top layer of the nanowires has a higher energy spectrum than the one on the bottom layer. The wafer then receives high frequency laser-pulses to excite the top layer of material. Due to the tight grouping, and the geometry of the nanowires, after excitation particles are radiated back into the wafer, potentially reexciting both layers of the neighboring nanowires. As a result, the energy pumped into the system is effectively trapped for times longer than is required by the laser to introduce it, which elevates the energy density into a state akin to a cold and uniform plasma. As the nanowires heat up, they expand to increase the medium particle density, and further reducing the space through which radiated photons can escape.

It's expected in numerical simulations of the process that metals with a higher energy

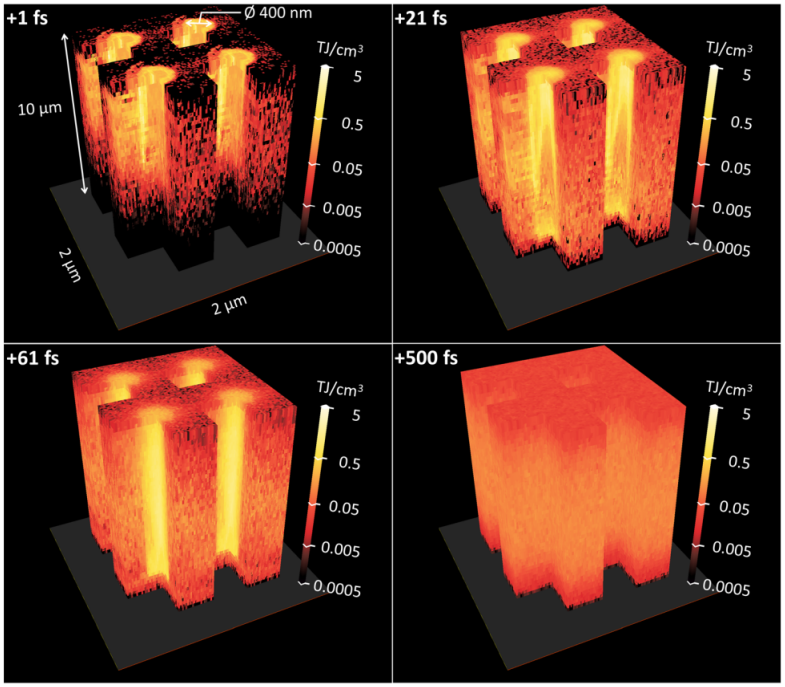

Figure 8.1: *A PIC simulation for gold nanowires of* 400 nm *under excitation of* 400 nm *laser-pulses as presented in [***15***]. The elapsed time after laser-pumping is displayed in each image. As time goes on, the energy density rises, until it's about uniform across the volume of the wafer.*

radiation spectrum will generate higher energy densities (Figure 8.1). Similarly, a higher pulse frequency can also increase the final energy density. The laser's spotsize will most immediately influence the particle number of the plasma. While the proposed simulations don't yet achieve energy densities as high as 10^{10}J cm^{-3}, they may do so with ultra-high frequency lasers and different materials.

An experimental setup placing such a nanowire wafer within a Penning trap could potentially create a monopole crystal with Avogadro numbers of particles, for which the approximated time-scales could be observed, most notable being perhaps the neutralisation time.

Proposals exist to generate extremely high contrast laser-pulses by frequency doubling the system energy with MeV x-ray laser sources. When using gold isotopes for the nanowires, emissions between 9.5 keV and 11 keV are expected, which would provide sufficient energy to fuse the emitted electrons into the hypothesized fused-electron droplet.

8.2. The N=13 Case

As a first look at multi-shell configurations, the $N = 13$ case can be computed with relatively little changes to the single-shell approach. As briefly discussed in section 4.2, the $N = 13$ configuration simply places an additional particle at the center of the $N = 12$ configuration, and after application of the mirror-charge method, a potential emerges. This results in a second "shell" with radius $r' = r_0 - \epsilon' = 0$ and consisting of a single particle. To help Mathematica along with the computation, the position functions were simplified using this new radius. In the following, ϵ will refer to the distance of the outer shell to the droplet's periphery.

$$\frac{1}{s} = \frac{1}{\sqrt{o^2 + r'^2 - 2or'\cos\theta}} \overset{r'=0}{=} \frac{1}{o}, \tag{8.2}$$

$$\frac{1}{s'} = \frac{1}{\sqrt{o^2 + (\frac{r_0^2}{r'})^2 - 2o\frac{r_0^2}{r'}\cos\theta}} \overset{r'=0}{=} 0. \tag{8.3}$$

After performing the multipole expansion and taking the rotational average,

$$U_{13}(\epsilon, o) = \frac{1}{o}\left(13 - 12\frac{r_0}{r_0 - \epsilon}\right) + \frac{1}{o^3}\frac{9\mathcal{R}_5}{32\pi(r_0 - \epsilon)^3}. \tag{8.4}$$

The results of the perturbation will now depend on which monopole experiences it. The central particle will behave differently from those in the outermost shell. A perturbation in the outer shell will behave as

$$\begin{aligned} U_{13,\,pert}(\epsilon, o, d\theta) = \frac{1}{o}&\left(13 - 12\frac{r_0}{r_0 - \epsilon}\right) \\ &+ \frac{1}{32\pi o^3}\left(\frac{\mathcal{R}_5}{(r_0 - \epsilon)^3} + \frac{\mathcal{R}_5}{(r_0 - \epsilon)^3}\cos 2d\theta\right). \end{aligned} \tag{8.5}$$

Just like before, the important part is the component containing the $d\theta$ contribution, which is isolated to part of the quadrupole moment $\frac{\mathcal{R}_5 \cos 2d\theta}{32\pi(r_0 - \epsilon)^3 o^3}$, which via derivation determines the oscillating monopole's spring constant to $k = \frac{q_e q_{Penning}\mathcal{R}_5 \cos 2d\theta}{8\pi(r_0 - \epsilon)^5 o^3}$. Its characteristic frequency is determined analogously to section 4.3 and evaluates again to 1.169×10^{-8} eV or 2.827×10^6 Hz. It translates into a period of 2.223×10^{-6} s. The results don't differ notably to

those of the single-shell configurations recorded in Table 4.4. The ratio of zero-point energy to rest mass energy evaluates to 8.799×10^{-17}.

The center monopole's position function has no angular components, so any meaning displacement first requires a radial component. For reasons discussed in section 4.2, this would likely quickly destabilize the configuration and not result in a harmonic oscillation. Assuming a stiff shell, and rewriting the position for the center particle to

$$\frac{1}{s} = \frac{1}{\sqrt{o^2 + dr^2 - 2dro\sin(\phi + d\phi)\cos(\theta + d\theta)}}, \tag{8.6}$$

$$\frac{1}{s'} = \frac{1}{\sqrt{o^2 + \left(\frac{r_0^2}{dr}\right)^2 - \frac{2or_0^2}{dr}\sin(\phi + d\phi), \cos(\theta + d\theta)}}, \tag{8.7}$$

and the perturbed potential evaluates to

$$\begin{aligned} U_{13,\,pert}(\epsilon, o, d\theta, dr) = \frac{1}{4\pi o}\left(13 - 12\frac{r_0}{r_0 - \epsilon} - \frac{r_0}{dr}\right) \\ - \frac{1}{32\pi o^3}\left(\frac{9\mathcal{R}_5}{(r_0 - \epsilon)^3} + dr^2 + \frac{r_0^5}{dr^3} + \frac{dr^5 - r_0^5}{dr^3}\cos 2d\theta\right). \end{aligned} \tag{8.8}$$

The geometry only pushes the outer shell into the droplet's periphery through Coulomb-repulsion. As such, there is no complete neutralisation time at which the droplet is predicted to lose its charge completely, but a charge drop-off up to a single electron charge would still be expected. In fact, once multiple shells are involved in a configuration, each shell will have a neutralisation time of its own. After a shell has neutralized, the configuration's N effectively shrinks. This is a continuous process, so the neutralization time of the next-largest shell depends primarily on the initial speed it's moving.

Due to the speed the particles have accumulated by the time the outer shell neutralizes, and the different initial radii, determining the full neutralisation times is non-trivial. At the time at which a shell neutralizes, the remaining configuration's potential changes fundamentally. The assumption that the potential acting on all particles of the configuration be equal can't be applied to these cases anymore. In the $N = 13$ case, it happens to be fairly easy to determine which component of the potential affects the outer shell, and which component affects the central particle by comparing the dependencies on their respective radii. The neutralisation time ends up predictably shorter, than that of the $N = 12$ case. It evaluates

to 123479 eV^{-1} = 5.107×10^{-10} s. This is a relatively large jump in comparison to the ones recorded in Table 6.1. The droplet's evaporation time, and lowest order breathing-frequency evaluate to 4.040×10^{-19} s and 3.628×10^{18} Hz respectively.

If the monopole in the center is shifted by both dr and $d\theta$, given a surrounding stiff configuration, the spring constant looks different (Figure 8.2). It obviously depends on $d\theta$, and on dr, and the derivative taken results in $\frac{1}{o^3}\left(\frac{3r_0^5}{2dr^4} + dr\right)$, which needs to be divided by the Jacobian determinant $r_0 - dr$. The majority of the values for the spring constant are of the order of magnitude of 10^{-7} eV^3, when letting dr take on values between 0 and r_0. The reasonable values for dr have an upper bound of ϵ, but as the spring constant isn't dependent on ϵ, dr is set between 0 and r_0.

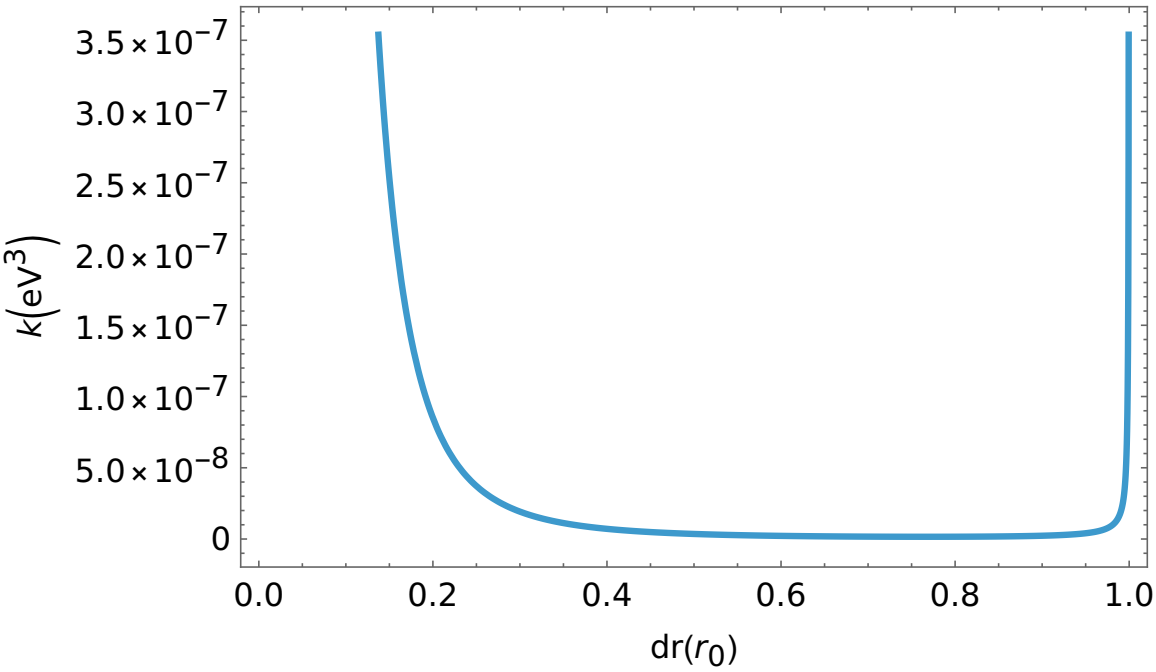

Figure 8.2: *The development of k for a monopole in the center offset by dr and dθ.*

9

Summary & Conclusion

In this thesis, the characteristic timescales and their behaviors of small N fused-electron droplets above Hagedorn temperature were determined and compared given parameters for an observer that matches the setup of a laboratory standard Penning trap. As discussed in section 7.3, the timescales of the Penning traps are independent of N. Three of the timescales describe different lifetimes for the charged droplet. These are the time for which the droplet remains in the Penning trap $\tau_{Penning}$, the time that plasma droplets of this type evaporate τ_{evap}, and the monopoles' neutralization time τ_{ne}. While $\tau_{Penning}$ is many orders of magnitude larger than the other two, which of the latter ones sets the de-facto lifetime of the droplet as a charged object is determined at least partially by N. Including further effects not considered in this thesis in an approximation for τ_{ne} and τ_{evap}, at macroscopic N, τ_{ne} is expected to be smaller than τ_{evap}. In an experiment, an observation of a discharging fused electron droplet would provide insights in line with Yang-Mills Thermodynamics.

The dynamics of the fused electron droplet are derived from geometric consideration for stable configurations detailed in chapter 3, but are based primarily in classical electro-dynamics. For larger N, the stable configurations will themselves be results of computationally expensive simulations, and provide usually non-unique solutions. The qualitative behavior of the monopoles in the droplet is expected to remain as it was described in this thesis for small N, especially the configurations approach face-centered cubic solutions. At large N, the quantitative behavior for the discharge process is expected to grow more complicated, as complications addressed in section 8.2 mount. The most important result of an experiment would be the observation of this process. The complications might introduce jerk to the electric potential of the monopole crystal as plotted in Figure 6.3.

The difference of the timescales identified in the processes contributing to the monopole

dynamics and discharging process allows an adiabatic approximation for these processes up to larger N. This allows the separation of the processes into different phenomena for an observer for a good first order approximation. The lifetimes for macroscopic N are projected to be over 10^{-11} s, which is significantly longer than the femtosecond timescales of ultrafast material sciences.

Bibliography

[1] Meinert, J.; Hofmann, R. Electroweak Parameters from Mixed SU(2) Yang–Mills Thermodynamics. Symmetry 2024, 16, 1587. [https://doi.org/10.3390/sym16121587].

[2] Michael Drewsen, Ion Coulomb crystals, Physica B: Condensed Matter, Volume 460, ISSN 09214526 Pages 105 - 113 [https://doi.org/10.1016/j.physb.2014.11.050]

[3] Tsui, YC., He, M., Hu, Y. et al., Direct observation of a magnetic-field-induced Wigner crystal [Nature 628, 287–292 (2024). https://doi.org/10.1038/s41586-024-07212-7]

[4] L. Świerkowski and D. Neilson, Enhancement of Wigner crystallization in multiple-quantum-well structures, [Phys. Rev. Lett. 67, 240 – Published 8 July, 1991, https://doi.org/10.1103/PhysRevLett.67.240]

[5] Richard Battye, Gary Gibbons, Paul Sutcliffe, Central Configurations in Three Dimensions [Proc.Roy.Soc.Lond.A459:911-943,2003, https://doi.org/10.48550/arXiv.hep-th/0201101]

[6] Thomas Hales, Mark Adams, Gertrud Bauer, Dat Tat Dang, John Harrison, Truong Le Hoang, Cezary Kaliszyk, Victor Magron, Sean McLaughlin, Thang Tat Nguyen, Truong Quang Nguyen, Tobias Nipkow, Steven Obua, Joseph Pleso, Jason Rute, Alexey Solovyev, An Hoai Thi Ta, Trung Nam Tran, Diep Thi Trieu, Josef Urban, Ky Khac Vu, Roland Zumkeller, A formal proof of the Kepler conjecture [HALES T, ADAMS M, BAUER G, et al. A FORMAL PROOF OF THE KEPLER CONJECTURE. Forum of Mathematics, Pi. 2017;5:e2. doi:10.1017/fmp.2017.1]

[7] R. W. Hasse, V. V. Avilov, Structure and Madelung energy of spherical Coulomb crystals [Phys. Rev. A 44, 4506, https://doi.org/10.1103/PhysRevA.44.4506]

[8] T. Erber, G. M. Hockney, Complex Systems: Equilibrium Configurations of N Equal Charges on a Sphere ($2 \leq N \geq 112$), Advances in Chemical Physics, Volume 98, 01 January 1997 [https://doi.org/10.1002/9780470141571.ch5]

[9] T. B. Mitchell and M. M. Schauer , Observation of Spherical Focus in an Electron Penning trap [Phys. Rev. Lett. 78, 58, https://doi.org/10.1103/PhysRevLett.78.58]

[10] Crimin, F., Garraway, B. M., & Verdú, J. (2017). The quantum theory of the Penning Trap. Journal of Modern Optics, 65(4), 427–440. [https://doi.org/10.1080/09500340.2017.1393570]

[11] Louis de Broglie, Translation by D. H. Delphenich. Review of the principles of classical mechanics - The Thermodynamics of the isolated particle, Neo-Classical Physics, THE GREAT PROBLEMS OF SCIENCE No. 17, 1964 [The Thermodynamics of the isolated particle]

[12] Faber, M. Conclusions Not Yet Drawn from the Unsolved 4/3-Problem—How to Get a Stable Classical Electron. Universe 2025, 11, 97. [https://doi.org/10.3390/universe11030097]

[13] Moosmann, Julian, Hofmann, Ralf. (2009). Charged Lepton Spectra from Hot-Spot Evaporation. ISRN High Energy Physics. 2012. 10.5402/2012/509793. [https://doi.org/10.5402/2012/509793]

[14] Hofmann, R.; Grandou, T. On Emergent Particles and Stable Neutral Plasma Balls in SU(2) Yang-Mills Thermodynamics. Universe 2022, 8, 117. [https://doi.org/10.3390/universe8020117]

[15] Clayton Bargsten, Reed Hollinger, Maria Gabriela Capeluto, Vural Kaymak, Alexander Pukhov, Shoujun Wang, Alex Rockwood, Yong Wang, David Keiss, Riccardo Tommasini, Richard London, Jaebum Park, Michel Busquet, Marcel Klapisch, Vyacheslav N. Shlyaptsev, Jorge J. Rocca Energy penetration into arrays of aligned nanowires irradiated with relativistic intensities: Scaling to terabar pressures. Sci. Adv.3,e1601558(2017). [DOI: 10.1126/sciadv.1601558]

[16] Sebastian Kilde Löfgren, Ricardo Méndez Fragoso, Jonathan Weidow, Jonas Enger The Mechanical Paul Trap: Introducing the Concept of Ion Trapping. Phys. Teach. 61, 762–765 (2023) [https://doi.org/10.1119/5.0106359]

[17] R H Hobart On the Instability of a Class of Unitary Field Models. 1963 Proc. Phys. Soc. 82 201 [R H Hobart 1963 Proc. Phys. Soc. 82 201]

[18] Bezdek, K., Blekherman, Greg, Connelly, R., Csikós, Balázs. (2001). The polyhedral Tammes problem. Archiv Der Mathematik - ARCH MATH. 76. 314-320. 10.1007/s000130050574. [April 2001, Archiv der Mathematik 76(4):314-320]

[19] Steven Ban, Matthew Bledsoe, Peter Chang, Garrett Wen Constructing a Paul Trap for Undergraduate Laboratories. Scholars at Harvard, May 2016. [constructing-paul-trap.pdf]

[20] Ronald J. Adler, Brendan Casey, Ovid C. Jacob; Vacuum catastrophe: An elementary exposition of the cosmological constant problem. Am. J. Phys. 1 July 1995; 63 (7): 620–626. [https://doi.org/10.1119/1.17850]

[21] Hofmann R., 2016, The thermodynamics of quantum Yang-Mills theory: Theory and applications, 2nd edition. World Scientific Publishing Co Pte Ltd, Singapore [https://doi.org/10.1142/9997]

[22] Forgács P., Volkov M. S., Phys. Rev. Lett. 92, 151802 – Published 12 April, 2004 Resonant Excitations of the 't Hooft–Polyakov Monopole [https://doi.org/10.1103/PhysRevLett.92.151802]

[23] E. Halley, Of the Infinity of the Sphere of Fix'd Stars, Phil. Trans. 31 (1720-1721) 22; Of the Order and Light of the Fix'd Stars, Phil. Trans. 31 (1720-1721) 24.[https://www.jstor.org/stable/i206896]

[24] H. Maehara, The problem of thirteen spheres — a proof for undergraduates, European Journal of Combinatorics, Volume 28, Issue 6, 2007, Pages 1770-1778 [https://doi.org/10.1016/j.ejc.2006.06.019]

[25] B. Williamson, An elementary treatise on the integral calculus, Longman and Green (1877). [An elementary treatise on the integral calculus]

[26] E.H. Lieb and H. Narnhofer, The thermodynamic limit from jellium, Journal of Statistical Physics 12 (1975) 291; Erratum in 14 (1976) 465. [https://doi.org/10.1007/BF01012066]

[27] Dmitri Diakonov, Nikolay Gromov, Victor Petrov, and Sergey Slizovskiy, Quantum weights of dyons and of instantons with nontrivial holonomy, Phys. Rev. D 70, 036003 – Published 17 August, 2004 [https://doi.org/10.1103/PhysRevD.70.036003]

[28] T Erber and G M Hockney 1991 J. Phys. A: Math. Gen. 24 L1369, Equilibrium configurations of N equal charges on a sphere [DOI 10.1088/0305-4470/24/23/008]

[29] R. Hofmann, Entropy 2017, 19(11), 575; The Isolated Electron: De Broglie's Hidden Thermodynamics, SU(2) Quantum Yang-Mills Theory, and a Strongly Perturbed BPS Monopole [https://doi.org/10.3390/e19110575

[30] Faber M. A Geometric Model in 3+1D Space-Time for Electrodynamic Phenomena. Universe. 2022; 8(2):73. [https://doi.org/10.3390/universe8020073]

[31] Freudenthal and B. L. van der Waerden, On an assertion of Euclid. (Dutch) Simon Stevin 25(1947), 115 - 121. Math Review 9, page 99c [https://pic.plover.com/papers/Freudenthal.pdf]

[32] Rajwade, A.R. (2001). The eight Deltahedra. In: Convex Polyhedra with Regularity Conditions and Hilbert's Third Problem. Texts and Readings in Mathematics. Hindustan Book Agency, Gurgaon. [https://doi.org/10.1007/978-93-86279-06-4-8]

[33] Marc Baus, Jean-Pierre Hansen, Statistical mechanics of simple coulomb systems Physics Reports Volume 59, Issue 1, March 1980, Pages 1-94 [https://doi.org/10.1016/0370-1573(80)90022-8]

[34] Wigner, E.P. (1997). On the Interaction of Electrons in Metals. In: Wightman, A.S. (eds) Part I: Physical Chemistry. Part II: Solid State Physics. The Collected Works of Eugene Paul Wigner, vol A / 4. Springer, Berlin, Heidelberg. [https://doi.org/10.1007/978-3-642-59033-7-36]

[35] Amore, P., Figueroa, V., Diaz, E. et al. Exploring the Energy Landscape of the Thomson Problem: Local Minima and Stationary States. J Stat Phys 192, 132 (2025). [https://doi.org/10.1007/s10955-025-03520-y]

[36] [https://github.com/aeffendie/adiabatic-approximation-monopole-crystals]

Appendices

A

Appendix

A.1. Code Excerpts

Numerical calculations in this thesis were made using *Mathematica*. Attached are annotated excerpts of the *Mathematica* notebooks. The code can be viewed in the git repository referenced in [**36**].

Listing A.1: Some function calls and definitions used in the calculations. Generally, computations are made in natural units, and the results optionally converted into SI units after the fact.

```
In[1]:=          (* Define Constants and dimensionless quantities *)
                 h = 1;
                 e = 12.96; (* Coupling at stabilizing temperature *)
                 qe = 4π/e Cos[30] (* Monopole charge for single electron *)
                 a0 = 0.622/(3.6 × 1000) (* Bohr radius in eV^-1 *)
                 R0[PN_] := PN^(1/3) a0
                 m0 = 0.511*10^7 (*Electron Mass in eV*);

                 (* Dimensionless distance of particle to droplet boundary *)
                 ϵ0[ϵ_, PN_] := -ϵ/R0[PN]

                 (* Dimensionless distance of observer charge to droplet center *)
                 o0[o_, PN_] := o/R0[PN]

                 (* Natural Units conversion constants *)
                 nuMeters = 805664 (* meters to eV^-1 *)
                 nuSeconds = 2.418 10^14 (* seconds to eV^-1 *)
                 nuHertz = 4.136 10^-15 (* Hertz to eV *)
```

```
19                nuKilogram = 5.61 10^35 (* kilogram to eV/c^2 *)
20
21                (* Penning trap Parameters in natural units *)
22                oPenning[PN_] := 0.003 nuMeters (*Distance of observer charge*)
23                QPenning = (15577.4/qe)/(0.003*5.07*10^6 )
```

Listing A.2: Implementation of the position functions s in two dimensions (s[θ_, r_, o_] and three dimensions (s3[θ_, ϕ_, r_, o_]. Each function is summarized to a monopole-antimonopole pair in the the functions n1 (two dimensions) and m1 (three dimensions). The factor R/r is a scaling for the charge, so that in later implementation, the full sum of position functions only needs to be multiplied by q_e and the observer charge as given by the Penning trap. Some naming conventions used in the code differ from those noted in the rest of the thesis. In this snippet, they are: $R = r_0$, $o = \frac{1}{o}$.

```
1  In[1]:=        (* Generic functions to describe the positions of the monopoles
       inside the droplet*)
2
3                 (* In 2D: Position of a single particle relative to droplet
                      center and position of observer charge *)
4                 s[θ_, r_, o_] := Sqrt[r^2 + o^2 - o*r*Cos[θ]]
5
6                 (* In 2D: Position of a monopole and its reflected charge
                      relative to droplet center and position of observer charge *)
                                                                    R
7                 n1[θ_, o_] := 1/(4π)(1/(s[θ, r, o]) - 1/(s[θ, b, o]))
8
9                 (* In 3D: Position of a single particle relative to droplet
                      center and position of observer charge *)
10                s3[θ_, ϕ_, r_, o_] := Sqrt[r^2 + o^2 - 2 r o Sin[ϕ] Cos[θ]]
11
12                (* In 3D: Position of a monopole and its reflected charge
                      relative to droplet center and position of observer charge *)
                                                                    R
13                m1[θ_, ϕ_, o_] := 1/(4π)(1/(s3[θ, ϕ, r, o]) - 1/(s3[θ, ϕ, b, o]))
```

Listing A.3: Computation and result for the $N = 2$ potential. The FullSimplify call is included for legibility and debugging purposes only. Some naming conventions used in the code differ from those noted in the rest of the thesis. In this snippet, they are: $R = r_0$, $o = \frac{1}{o}$. The inversion of o is primarily included for legibility reasons in the printed result.

```
1  In[1]:=        (* Write rotationally stiff configuration *)
2                 n2[θ_, o_] := n1[θ, o] + n1[θ + π, o]
3
4                 (* Perform multipole expansion. The Charge is omitted. *)
5                 intgr2[θ_, o_] := FullSimplify[Series[n2[θ, 1/o],
6                         {o, 0, 3}], o > 0
7                 ]
```

```
8
9                   (* Average over full rotation *)
10                  Integrate[intgr2[θ, o] * Sin[θ]/(4π),
11                          {θ, 0, π},
12                          {ϕ, 0, 2 π}
13                  ] /. r -> R - ϵ /. b -> R^2/(R - ϵ)
14  Out[3]:= (-3o^3 (-R^5/(R - ϵ)^2 + (R - ϵ)^3) - 8oϵ)/(16π(R - ϵ))
```

Listing A.4: Computation and result for the $N = 12$ potential. The FullSimplify call is included for legibility while debugging only. Some naming conventions used in the code differ from those noted in the rest of the thesis. In this snippet, they are: $R = r_0$, $o = \frac{1}{o}$. The inversion of o is primarily included for legibility reasons in the printed result

```
1   In[1]:= n12[θ_, ϕ_, o_] := m1[θ, ϕ, o] +
2                           m1[θ + 2π/3, ϕ + π/5, o] +
3                           m1[θ + 2π/3, ϕ + 3π/5, o] +
4                           m1[θ + 2π/3, ϕ + 5π/5, o] +
5                           m1[θ + 2π/3, ϕ + 7π/5, o] +
6                           m1[θ + 2π/3, ϕ + 9π/5, o] +
7                           m1[θ + 4π/3, ϕ, o] +
8                           m1[θ + 4π/3, ϕ + 2π/5, o] +
9                           m1[θ + 4π/3, ϕ + 4π/5, o] +
10                          m1[θ + 4π/3, ϕ + 6π/5, o] +
11                          m1[θ + 4π/3, ϕ + 8π/5, o] +
12                          m1[θ + π, ϕ, o]
13
14                  intgr12[θ_, ϕ_, o_] := FullSimplify[Series[n12[θ, ϕ, 1/o],
15                          {o, 0, 3}], o > 0
16                  ]
17                  Integrate[intgr12[θ, ϕ, o] * Sin[θ]/(4π),
18                          {θ, 0, π},
19                          {ϕ, 0, 2 π}
20                  ] /. r -> R - ϵ /. b -> R^2/(R - ϵ)
```

21

22 Out[3]:=
$$\frac{-9o^3\left(-\frac{R^5}{(R-\epsilon)^2}+(R-\epsilon)^3\right)-96o\epsilon}{32\pi(R-\epsilon)}$$

Listing A.5: Computation and result for the $N = 2$ potential where one of the particles experiences a displacement by $d\theta$ and $d\phi$. The FullSimplify call is included for legibility while debugging only. Some naming conventions used in the code differ from those noted in the rest of the thesis. In this snippet, they are: $R = r_0$, $o = \frac{1}{o}$. The inversion of o is primarily included for legibility reasons in the printed result.

```
1  In[1]:=          (* Stiff configuration with perturbation in angles θ, ϕ *)
2                   (* Multipole expansion and averaging over rotation follows.
                        Charges are omitted *)
3                   p2[θ_, o_] := m1[θ + dθ, ϕ + dϕ, o] +
4                           m1[θ + π, ϕ o]
5
6                   perturb2[θ_, o_] := FullSimplify[Series[p2[θ, ϕ, 1/o],
7                           {o, 0, 3}], o > 0
8                   ]
9
10                  Integrate[perturb2[θ, ϕ, 1/o] * Sin[θ]/(4π),
11                          {θ, 0, π},
12                          {ϕ, 0, 2 π}
13                  ] /. r -> R - ϵ /. b -> R^2/(R - ϵ)
14
```

15 Out[3]:=
$$\frac{o^3\left(\frac{R^5}{(R-\epsilon)^2}-(R-\epsilon)^3\right)-8o\epsilon-o^3\left(-\frac{R^5}{(R-\epsilon)^2}+(R-\epsilon)^3\right)Cos[d\theta]^2}{32\pi(R-\epsilon)}$$

Listing A.6: The derivative of the potential including an offset particle gives the factor of the spring constant in the term linear to $d\theta$. sk2 in the snippet is the copied result of the computation in Listing A.5 to save on computation time. Some naming conventions used in the code differ from those noted in the rest of the thesis. In this snippet, they are: $R = r_0$, $o = \frac{1}{o}$. The inversion of o is primarily included for legibility reasons in the printed result.

```
1  In[1]:=          D[Series[sk2[dθ, o], {dθ, 0, 2}], dθ]
2
```

3 Out[1]:=
$$\frac{o^3\left(-\frac{R^5}{(R-\epsilon)}+(R-\epsilon^3\right)d\theta}{8\pi(R-\epsilon)}+O[d\theta]^2$$

Listing A.7: Function definitions for the spring constants, this time including the charges. Because of the format of the results in Listing A.6, the full function is reimplemented in full for both the general case, and the irregular $N = 8$. The monopole's radial coordinate is chosen to be at $\frac{1}{3}r_0$. The call for the Abs function is included for convenience. Some naming conventions used in the code differ from those noted in the rest of the thesis. In this snippet, they are: $R = r_0$, $qe = q_e$, $QPenning = Q_{Penning}$, $PN = N$, $o = \frac{1}{o}$. The inversion of o is primarily included for legibility reasons in the printed result.

```
In[1]:=        (* Recurring Factor, included for legibility *)
               Rfactor[ϵ_, R_] := ((R - ϵ)^3 - R^5/(R - ϵ)^2)/(R - ϵ);

               (* The general case for the spring constant. Previously omitted
                   charges included here *)
               kgeneral[o_, PN_] := (qe * QPenning * Rfactor[(2R0[PN])/3, R0[PN]])/(8πo^3)

               (* The N=8 case for the spring constant. Previously omitted
                   charges included here *)
               k8[o_] := \cfrac{qe * QPenning * Rfactor[(2 R0[8])/3, R0[8]]}{16\
                   pi o^3}

               (* The general case for the oscillation frequency *)
               ωgeneral[o_, m_, PN_] := Sqrt[(Abs[kgeneral[o, PN]]/m)]

               (* The N=8 case for the oscillation frequency *)
               ω8[o_, m_] := Sqrt[(Abs[k8[o]]/m)]

               zeroPointEnergy[ω_] := 1/2 h*ω
               massEnergy[PN_] := PN*m0
```

Listing A.8: Solving the differential equation for $\epsilon(t)$. U2 is the result of Listing A.3 as a function to save computation time. Some naming conventions used in the code differ from those noted in the rest of the thesis. In this snippet, they are: $R = r_0$, $qe = q_e$, $QPenning = Q_{Penning}$, $o = \frac{1}{o}$. The inversion of o is primarily included for legibility reasons in the printed result.

```
In[1]:=        adif2[ϵ_, R_, o_] := D[(qe*QPenning)/R0[2] U2[R, o, ϵ],
                       ϵ] /. {o -> 1/(3*10^7), R -> 1}
               dif2[ϵ_] := adif2[ϵ, 1, 1/(3*10^7)] (*3*10^7*)
               tt2 = NDSolve[{eps2''[t] == dif2[eps2[t]] /m0, eps2[0] == 2/3,
                   eps2'[0] == 0}, eps2, {t, 0, 10^10}]
               Plot[eps2[x] /. tt2, {x, 0, 65000}]
               FindRoot[eps2[t] == 0 /. tt2, {t, 2*10^5, 0, 10^7}]
```

Listing A.9: Additional definitions used in the calculations in chapter 6. The computation utilizes many constants previously defined in natural units, but the Penning trap parameters in chapter 6 and **[9]** were given in SI, hence the heavy use of conversion constants in the formulas for the characteristic frequencies of the Penning trap and the damping constant.

```
In[1]:=         nuTesla = 692.50778 (* Tesla to eV^2 *)
                nuCoulomb = 5.33178 10^17(* Coulomb to natural units (
                    dimensionless) *)

                (* Penning trap Parameters in natural units *)
                oPenning[PN_] := 0.003*nuMeters (*Distance of observer charge*)

                (* Monopole charge and its reflected charge *)
                qTotal[R_, ϵ_] := qe + qe R/(R-ϵ)

                (* Motion in Penning trap, in SI units. *)
                ωc[PN_, B_] := Abs[B*qTotal[R0[PN], (2R0[PN])/3]/nuCoulomb]/(m0/nuKilogram)
                ωz[PN_, V_, d_] := Sqrt[qTotal[R0[PN], (2R0[PN])/3]/nuCoulomb/(d*m0/nuKilogram)*V]
                ωm[PN_, V_, d_, B_] := ωz[PN, V, d]^2/ωc[PN, B]

                (* Damping Time. Typically years, but Radiation Damping for 2
                    charged particles *)
                (* Use r0 = e^2/mc^3 *)

                (* Damping Constant, includes e^2/c^3 factor that is not noted
                    down here *)
                γc[PN_, B_] := ((4 ωc[PN, B]^2)/(3*2*m0/nuKilogram))
```

Listing A.10: Calculation of the voltage V_0 at which the ensemble in the Penning trap takes on the most spherical shape in SI units using the selected Penning trap parameters $B_{Penning} = 0.22$ T and $d_{Penning} = 3$ mm.

```
In[1]:=         BPenning = 0.22;
                dPenning = 0.003;
                VPenning = (qTotal[R0[12], (2R0[12])/3]/nuCoulomb BPenning^2 dPenning^2)/(8m0/nuKilogram)

Out[3]:=        6707.52
```

Listing A.11: Computation of the Penning frequencies for the extremes of single-shell configuration particle numbers. The dependency on the particle number cancels.

```
In[1]:=         ωc[2, BPenning]
                ωz[2, VPenning, dPenning]
                ωm[2, VPenning, dPenning, BPenning]

Out[1]:=        2.71011 × 10^10
```

```
Out[2]:=          5.2481 × 10^8
Out[3]:=          1.01629 × 10^7

 In[4]:=          ωc[12, BPenning]
                  ωz[12, VPenning, dPenning]
                  ωm[12, VPenning, dPenning, BPenning]

Out[4]:=          2.71011 × 10^10
Out[5]:=          5.2481 × 10^8
Out[6]:=          1.01629 × 10^7
```

Listing A.12: Computation and result for the $N = 13$ potential. The FullSimplify call is included for legibility while debugging only. Some naming conventions used in the code differ from those noted in the rest of the thesis. In this snippet, they are: $R = r_0$, $o = \frac{1}{o}$. The inversion of o is primarily included for legibility reasons in the printed result.

```
In[1]:= n13[θ_, ϕ_, o_] := m1[θ, ϕ, o] +
                        m1[θ + 2π/3, ϕ + π/5, o] +
                        m1[θ + 2π/3, ϕ + 3π/5, o] +
                        m1[θ + 2π/3, ϕ + 5π/5, o] +
                        m1[θ + 2π/3, ϕ + 7π/5, o] +
                        m1[θ + 2π/3, ϕ + 9π/5, o] +
                        m1[θ + 4π/3, ϕ, o] +
                        m1[θ + 4π/3, ϕ + 2π/5, o] +
                        m1[θ + 4π/3, ϕ + 4π/5, o] +
                        m1[θ + 4π/3, ϕ + 6π/5, o] +
                        m1[θ + 4π/3, ϕ + 8π/5, o] +
                        m1[θ + π, ϕ, o] + 1/o

                intgr13[θ_, ϕ_, o_] := FullSimplify[Series[n13[θ, ϕ, 1/o],
                        {o, 0, 3}], o > 0
                ]
                Integrate[intgr13[θ, ϕ, o] * Sin[θ]/(4π),
                        {θ, 0, π},
                        {ϕ, 0, 2 π}
                ] /. r -> R - ϵ /. b -> R^2/(R - ϵ)
```

21

22 Out[3]:=
$$\frac{-96oR+\frac{9o^3R^5}{(R-\epsilon)^2}+104o(R-\epsilon)-9o^3(R-\epsilon)^3}{32\pi(R-\epsilon)}$$

Listing A.13: Computation and result for the $N = 13$ potential where one of the particles in the outer shell experiences a displacement by $d\theta$ and $d\phi$. The FullSimplify call is included for legibility while debugging only. Some naming conventions used in the code differ from those noted in the rest of the thesis. In this snippet, they are: $R = r_0$, $o = \frac{1}{o}$. The inversion of o is primarily included for legibility reasons in the printed result.

1 In[1]:= p13[θ_, ϕ_, o_] := m1[θ + dθ, ϕ + dϕ, o] +

2 m1[θ + $\frac{2\pi}{3}$, ϕ + $\frac{\pi}{5}$, o] +

3 m1[θ + $\frac{2\pi}{3}$, ϕ + $\frac{3\pi}{5}$, o] +

4 m1[θ + $\frac{2\pi}{3}$, ϕ + $\frac{5\pi}{5}$, o] +

5 m1[θ + $\frac{2\pi}{3}$, ϕ + $\frac{7\pi}{5}$, o] +

6 m1[θ + $\frac{2\pi}{3}$, ϕ + $\frac{9\pi}{5}$, o] +

7 m1[θ + $\frac{4\pi}{3}$, ϕ, o] +

8 m1[θ + $\frac{4\pi}{3}$, ϕ + $\frac{2\pi}{5}$, o] +

9 m1[θ + $\frac{4\pi}{3}$, ϕ + $\frac{4\pi}{5}$, o] +

10 m1[θ + $\frac{4\pi}{3}$, ϕ + $\frac{6\pi}{5}$, o] +

11 m1[θ + $\frac{4\pi}{3}$, ϕ + $\frac{8\pi}{5}$, o] +

12 m1[θ + π, ϕ, o] + $\frac{1}{o}$

13

14 perturb13[θ_, ϕ_, o_] := FullSimplify[Series[p13[θ, ϕ, 1/o],

15 {o, 0, 3}], o > 0

16]

17 Integrate[perturb13[θ, ϕ, o] * $\frac{Sin[\theta]}{4\pi}$,

18 {θ, 0, π},

19 {ϕ, 0, 2 π}

20] /. r -> R - ϵ /. b -> $\frac{R^2}{R-\epsilon}$

21

22 Out[3]:=
$$-\frac{o(8(R(12-\frac{o^2R^4}{(R-\epsilon)^2}-13(R-\epsilon)+o^2(R-\epsilon)^3)+o^2(-\frac{R^5}{(R-\epsilon)^2}+(R-\epsilon)^3)Cos[2d\theta]}{32\pi(R-\epsilon)}$$

Listing A.14: Computation and result for the $N = 13$ potential where the center particles experiences a displacement by $d\theta$ and $d\phi$. The FullSimplify call is included for legibility while debugging only. Some naming conventions used in the code differ from those noted in the rest of the thesis. In this snippet, they are: $R = r_0$, $o = \frac{1}{o}$. The inversion of o is primarily included for legibility reasons in the printed result.

```
In[1]:= p13[θ_, ϕ_, o_] := m1[θ + dθ, ϕ + dϕ, o] +
                            m1[θ + 2π/3, ϕ + π/5, o] +
                            m1[θ + 2π/3, ϕ + 3π/5, o] +
                            m1[θ + 2π/3, ϕ + 5π/5, o] +
                            m1[θ + 2π/3, ϕ + 7π/5, o] +
                            m1[θ + 2π/3, ϕ + 9π/5, o] +
                            m1[θ + 4π/3, ϕ, o] +
                            m1[θ + 4π/3, ϕ + 2π/5, o] +
                            m1[θ + 4π/3, ϕ + 4π/5, o] +
                            m1[θ + 4π/3, ϕ + 6π/5, o] +
                            m1[θ + 4π/3, ϕ + 8π/5, o] +
                            m1[θ + π, ϕ, o] +
                            1/Sqrt[dr^2 + o^2 - 2dr oSin[ϕ + dϕ]Cos[θ + dθ]] -
                            R/dr/Sqrt[R^4/dr^2 + o^2 - 2oR^2/dr Sin[ϕ + dϕ]Cos[θ + dθ]]

                        perturb13[θ_, ϕ_, o_] := FullSimplify[Series[p13[θ, ϕ, 1/o],
                                {o, 0, 3}], o > 0
                        ]

                        Integrate[perturb13[θ, ϕ, o] * Sin[θ]/4π,
                                {θ, 0, π},
                                {ϕ, 0, 2 π}
                        ] /. r -> R - ϵ /. b -> R^2/(R - ϵ)

Out[3]=         -1/(32πdr^3(R - ϵ)) o(
                                dr^3(96R - 9o^2R^5/(R - ϵ)^2 - 104(R - ϵ) + 9o^2(R - ϵ)^3) +
                                dr^5o^2(R - ϵ) + 8dr^2R(R - ϵ) -
                                o^2R^5(R - ϵ) + o^2(dr^5 - R^5)(R - ϵ)Cos[2dθ])
```

A.2. Generated Graphs

During computation, several collections of graphs were generated, of which only one was presented in the main body of the thesis to serve as an example. This section contains all graphs for cases $N = 2$ through $N = 12$.

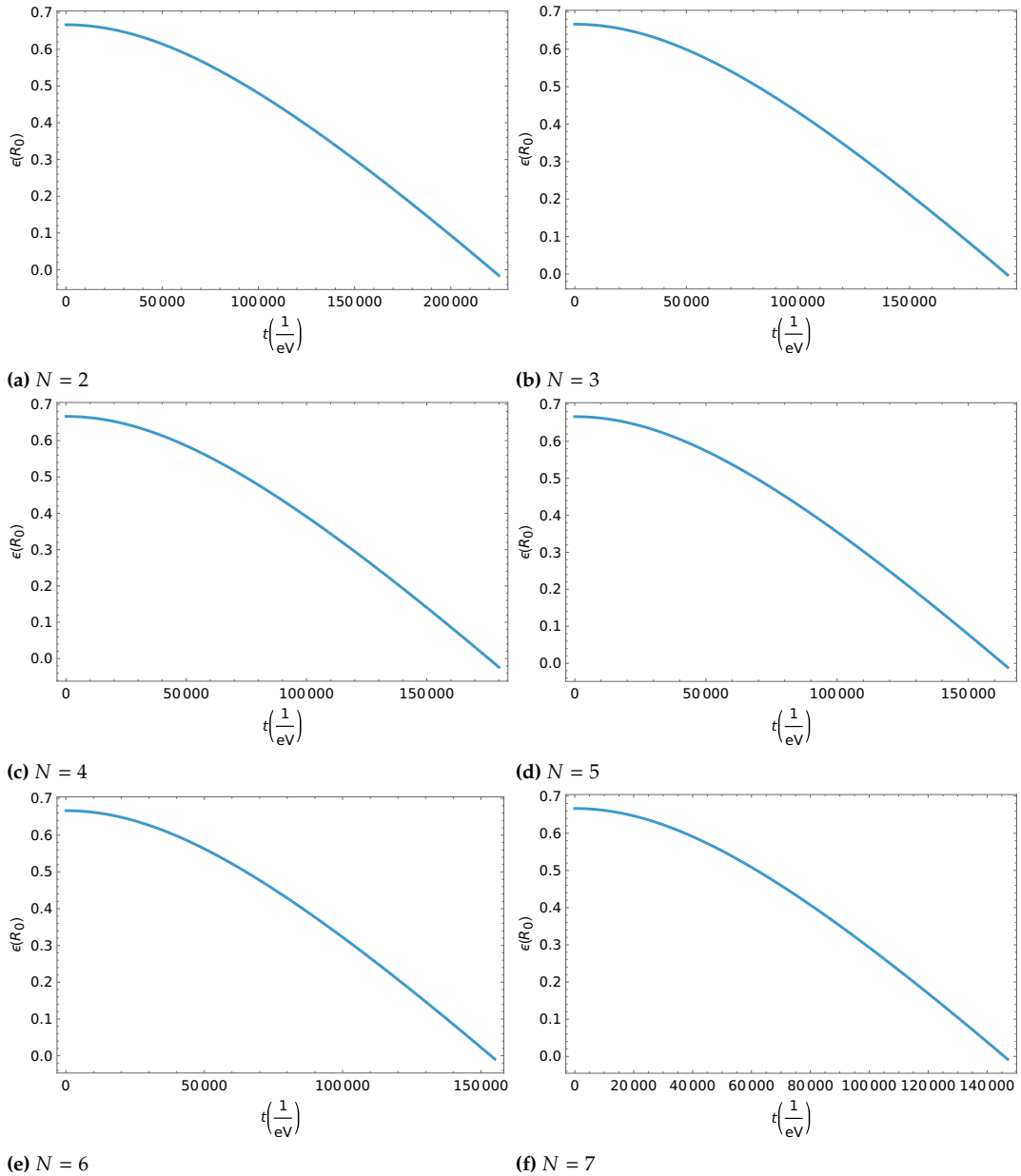

(a) $N = 2$ **(b)** $N = 3$

(c) $N = 4$ **(d)** $N = 5$

(e) $N = 6$ **(f)** $N = 7$

Figure A.1: Neutralisation times τ_{ne} as discussed in chapter 6 for $N = 2$ to $N = 7$.

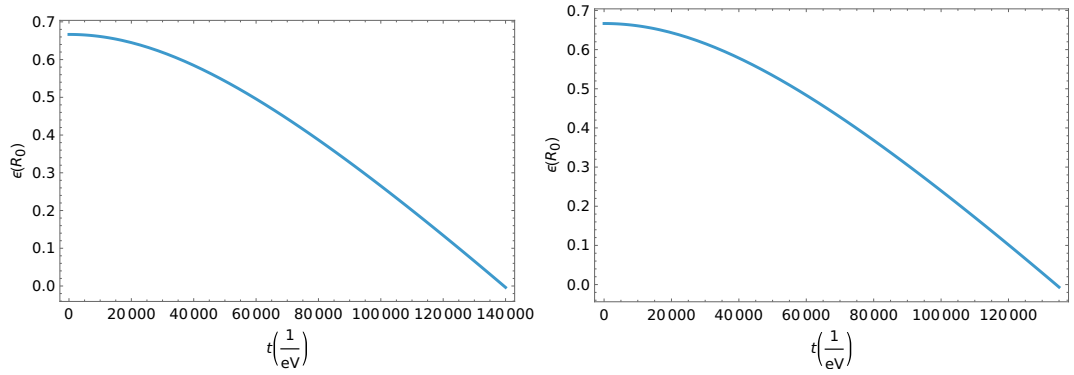

(a) $N = 8$

(b) $N = 9$

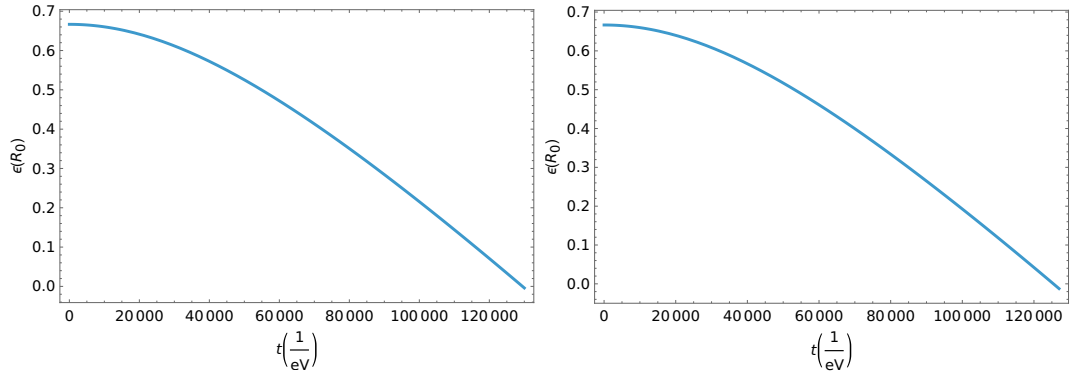

(c) $N = 10$

(d) $N = 11$

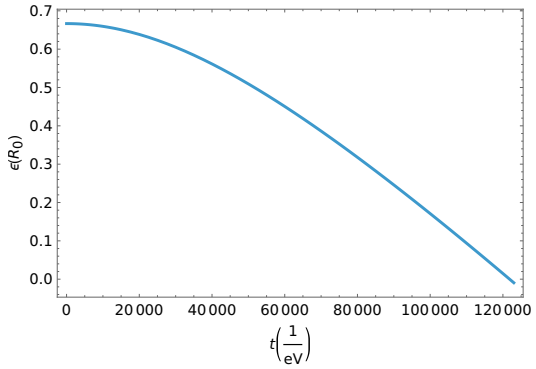

(e) $N = 12$

Figure A.2: Neutralisation times τ_{ne} as discussed in chapter 6 for $N = 8$ to $N = 12$.

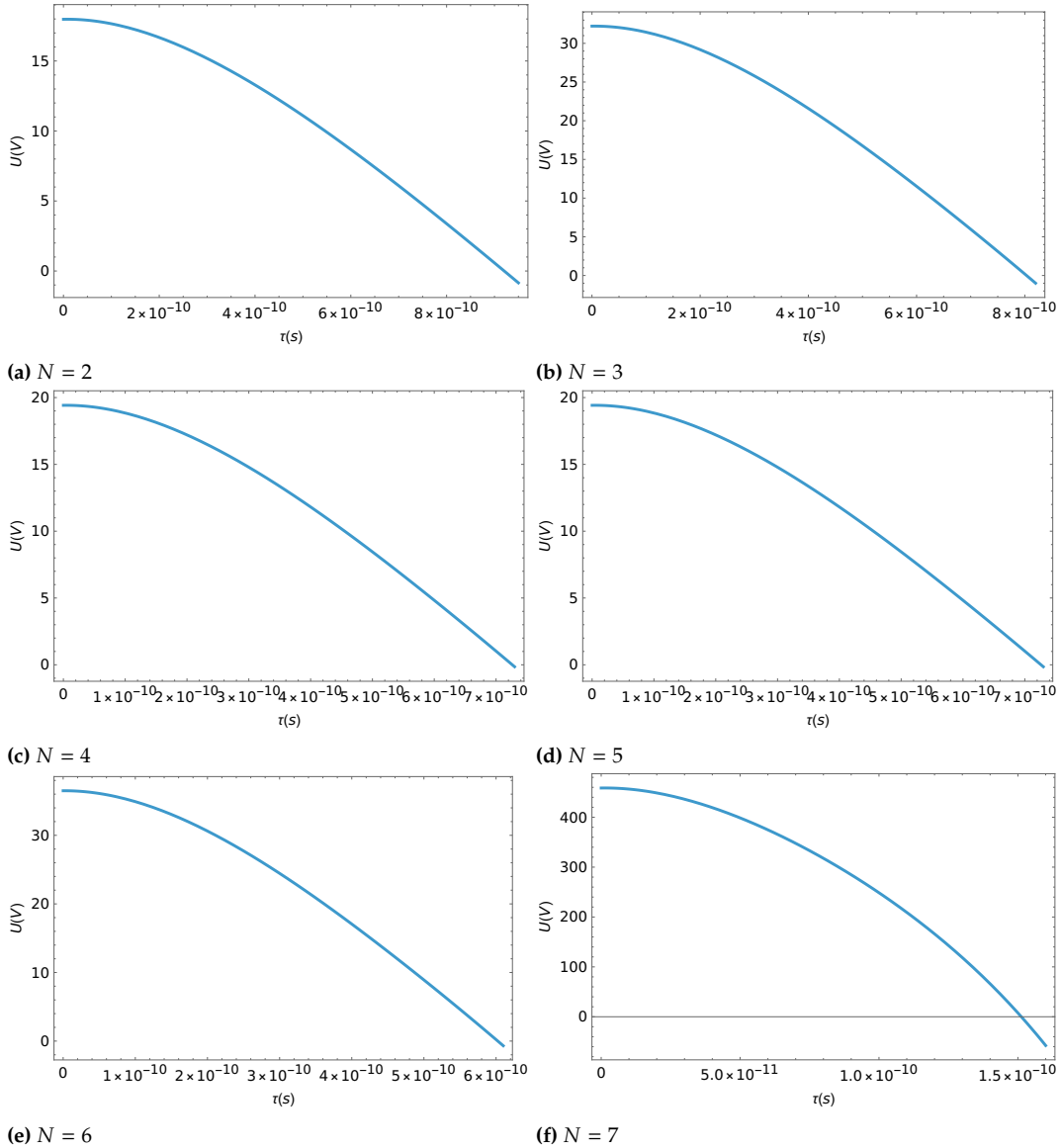

(a) $N = 2$ **(b)** $N = 3$

(c) $N = 4$ **(d)** $N = 5$

(e) $N = 6$ **(f)** $N = 7$

Figure A.3: Charge development as discussed in chapter 6 for $N = 2$ to $N = 7$.

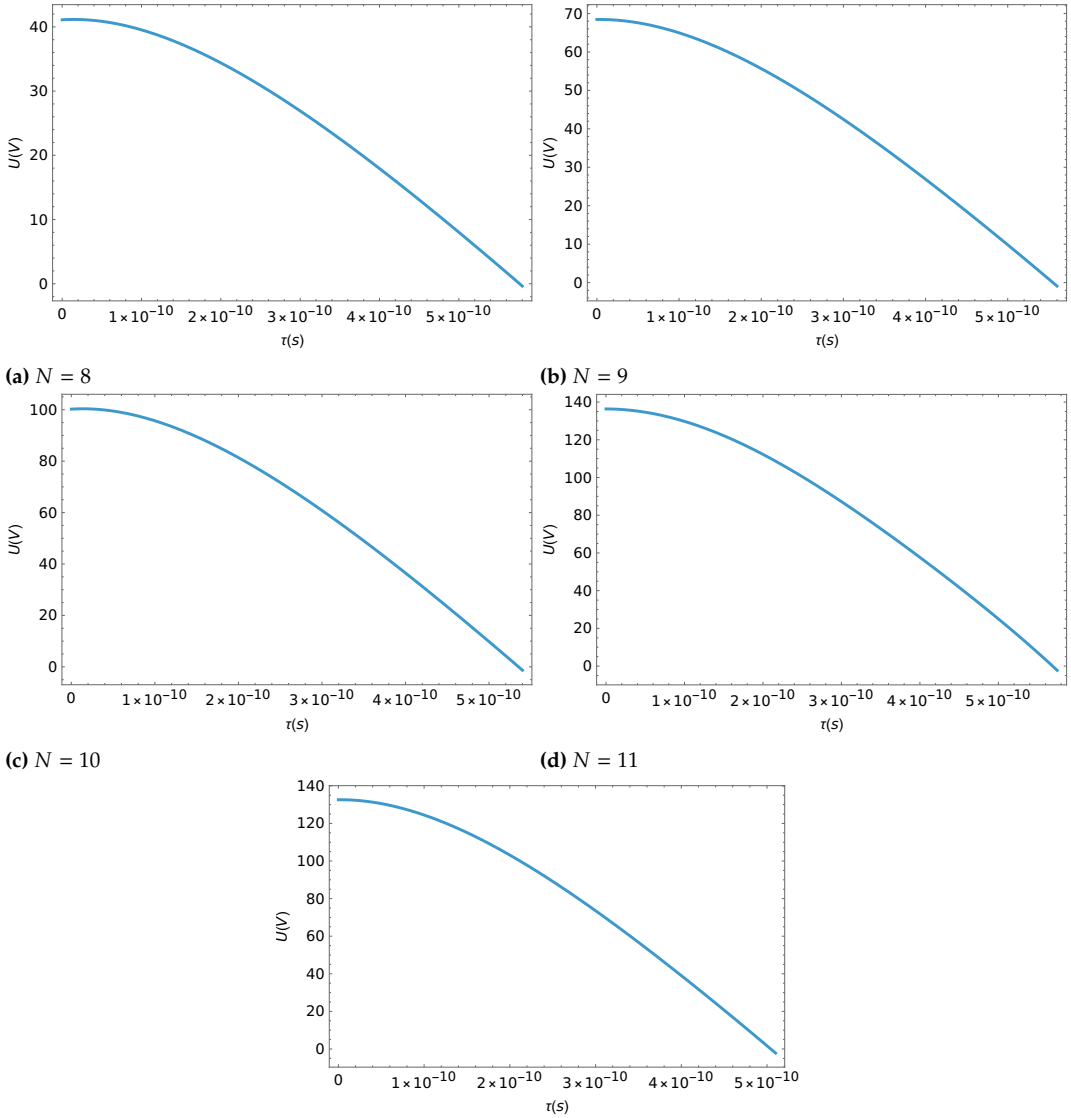

(a) $N = 8$ **(b)** $N = 9$

(c) $N = 10$ **(d)** $N = 11$

(e) $N = 12$

Figure A.4: Charge development as discussed in chapter 6 for $N = 8$ to $N = 12$.

A.3. Comparisons From Plasma Physics

A.3.1. Coulomb Crystals

In the field of non-neutral plasma physics, the stable configurations of free particles are considered crystals due to the crystalline structure of stable configurations. Configurations of Coulomb Crystals emerge from classical electrodynamics, and the results should be approximate with the monopole crystals (Figure 3.1). Coulomb-Crystals are typically metastable configurations of ions, held in an external field. Metastable configurations are pushed apart due to Coulomb repulsion created by the equal charges of each constituent ion. Most important for the specifics of the configuration is the ratio of mass and electric charge. If the ensemble consists of ions with different mass-charge ratios, they form overlapping, concentric Coulomb-Crystals interacting with one another [**2**].

At smaller numbers, the crystals consist of a shell-structure with each shell usually taking on the shape of a polyhedron. The number of particles occupying each shell conforms to a numerically determined magic number as determined in Figure 3.2. For large numbers, Coulomb-Crystal configurations have been observed to approach FCC. Coulomb-Crystals and their dynamics are descriptive for ions only. Separate dynamics, and slightly different geometry, are expected for similar phenomena using electrons. The realization of such *Wigner Crystals* outside strong external magnetic fields is a relatively recent development, due to the exact conditions required for meta-stability.

A.3.2. Comparison to Wigner Crystals

A similar phenomenon in spontaneous self-organization applied to electrons is that of the Wigner-Crystals, though these are so far explicitly two-dimensional objects. This thesis attempts to construct generally three-dimensional configurations of quantum objects of similar mass-scale, but direct comparisons between Wigner crystals and the few two-dimensional configurations could be of interest in the future.

At the basis of electron solids is the comparison between the potential energy acting on an electron, and its kinetic energy imparted to it through the ensemble's temperature. At low temperatures and densities, electron motion slows down far enough for their electric charge to influence their interactions and dynamics, causing them to crystallize into a quasi-solid. Strongly interacting electrons can break translation and orientation symmetry (i.e. the classical assumption that the action of the particle is independent of its position in space and the direction its momentum vector is directed), leading them to crystallize spontaneously into a

quasi-solid structure, tuned to the electron density.

The theoretical condition for Wigner Crystals is that the external potential energy outcompetes the electron's kinetic energy at a crystallized inter-cell distance. The original conception featured an electron gas in a periodic potential. The Coulomb-interactions at low particle density, the electron-electron correlation energies diminish as r_s is increased. The particle energy on a lattice depends on the Coulomb potential and kinetic energy. The Coulomb interaction in ions increases quickly with increasing density, eclipsing the kinetic energy, and localizing the ions. For 2D systems of electrons with $n_e = \frac{1}{\pi r_0^2}$, the mean potential energy per electron is $U_c = \frac{e^2}{r_0} = \frac{2}{r_s}[Ry], Ry = \frac{me^4}{w\hbar^2} = 13.6eV, r_s = \frac{r_0}{a_B}$. The kinetic energy for a single electron in a simple electron spectrum is written $K_e = \frac{\hbar^2}{2m_e r_0^2} = \frac{1}{r_s^2}[Ry]$. Relevant to the construction of Wigner Crystals is the order of the radius in each term comprising the electron's full energy. The r-dependency is r^{-1} of the potential, and r^{-2} of the kinetic energy, which eventually suppresses the kinetic term for $r_s >> 1$. Electrons in ground state of such 2D systems were hence postulated to form a perfect lattice, an *electron solid* [**34**]. As the dimensionality does not generally line up with that of the monopole crystals, the effects can be compared either at minimal particle numbers ($N \in \{2, 3\}$), or at very large numbers, where the monopole crystal structure approaches crystalline packing, which creates layers of perfect lattices. This assumes that at such particle numbers, the effects along an axis perpendicular to the Wigner crystal can be separated and treated independently of one another.

The first observation of such Wigner crystals was made in bilayer graphene in a large perpendicular magnetic field at very low temperatures (210 mK in experiments [**3**]). The system is imaged using scanning tunnelling microscopy (STM), the use of which hints at the necessity for significant potential wells or barriers, probing the electron's wavefunction directly, and hence extracting data as to whether the crystallized lattice is ordered and how the lattice constant changes with particle density, and whether it melts into other quantum phases. The data is in line with predicted behavior for Wigner crystals. A zero-point oscillation for an electron has also been observed, occupying a space on length scales of about 30% of the lattice constant for its crystal site. Whether this is related to the zero-order oscillation that was predicted for perturbed BPS monopoles in monopole crystals is not trivial to determine, but could be an interesting avenue to pursue in future considerations. Perhaps the naturally occuring oscillation frequency for the $N = 3$ case could be compared to that of the zero-point motion inside the Wigner crystal, seeing as this case exists in the same geometry as the Wigner crystal.

A.4. Relation to the Sphere-Packing Problem

At large particle numbers, the approach using shells with magic numbers will likely not suffice completely, as the system size is expected to grow much slower than the particle number, and the space between charged particles decreases. The magic numbers emerge primarily as a statement of stability within one shell, but when the inter-shell distance becomes smaller than the distance between shell-neighbors, different solutions emerge, approximating spherical FCC packing. Such solutions are often viable, but not unique to their minimal energy. Further insights on the in-shell configuration might be derived from solutions to the Sphere-Packing problem, once the particle-shell distribution has been approximated. It's not unlikely for configurations of large particle numbers to be somewhat spherically asymmetric as well, and hence inherit some traits of the irregular cases. As a consequence it likely doesn't matter that the particle number in each shell is exactly correct, as long as the ratio between particle numbers between shells is representative of the area available to each particle within it.

Algorithmic approaches for the Sphere-Packing Problem exist for relatively high numbers, so simulations (wrongly) assuming meta-stability could be run for large particle numbers applying the model described in this thesis. Whether the issue of meta-stability will be voided as more shells are added remains to be seen.

A.5. The Earnshaw Theorem as an Argument for the Choice of Quadrupole Trap

A.5.1. The Earnshaw Theorem

Earnshaw's Theorem states that a collection of point charges can't be maintained in stable stationary equilibrium configurations by the particle-particle interactions themselves. The theorem was devised first for electrostatics, but it functions similarly for magnetism, and gravitational forces. For soft magnets, materials that are easily magnetized and demagnetized, the theorem requires a slight extension.

This is not a contradiction with respect to the existence of solid matter and crystal structures, as the charges in matter are not isolated point charges, but rather distributed in matter. Other systems of isolated bodies usually feature accelerations, but this was disallowed by models of the atom that define electrons as isolated particles. The solution was provided by the quantum mechanical approach of expressing electrons as charge densities in some volume

within the particles, separated in energy state by the Pauli exclusion principle.

Underlying the proofs for different situations is that the Laplacian of each magnetic field component is also zero, which is shown by invoking magnetic field properties anchored in the Maxwell equations of electrodynamics. These posit that both the curl of and the divergence of magnetic fields vanish.

For fixed-orientation magnetic dipoles, the Earnshaw Theorem is written as $\Delta U = 0$. Write the energy U of the magnetic dipole M as $U = -M \cdot B$, which is linear in the Laplacian, and can be rearranged

$$\Delta U = -\partial_{x_i}^2 (M_{x_j} B_{x_j}) \tag{A.1}$$
$$= -M_{x_i} \Delta B_{x_i}, \tag{A.2}$$
$$\Delta B_{x_i} = 0, \tag{A.3}$$
$$\Rightarrow \Delta U = -M_{x_i} 0 = 0. \tag{A.4}$$

If the magnetic dipole is aligned with external field lines, one only needs to show that $U = -k|B|^2$. The constant k can be divided out. It then suffices to argue that $\Delta |B|^2 = 0$. Using the aforementioned statement that $\Delta B_{x_i} = 0$,

$$\Delta |B|^2 = 2(|\nabla B_{x_i}|^2 + B_{x_i} \Delta B_{x_i}) \tag{A.5}$$
$$= 2(|\nabla B_{x_i}|^2) \geq 0. \tag{A.6}$$

In paramagnetic materials, this indicates that its Laplacian of the energy is never positive, and there can't be any stable levitation. In diamagnetic materials, the Laplacian of the energy can't be negative, so a potential can't have points with instabilities in all directions.

A.5.2. Paul Trap Accuracy

Technically, a fully stationary monopole crystal would allow for an adiabatic approximation without consideration of the frequencies given by the full droplet's dynamics inside the Penning trap. However, the stationary type of quadrupole trap relies on a rapid change of field to create a potential minimum when averaged over time, applying its own adiabatic approximation as a trapping condition.

The concept of the trap is rooted in the classical approach based on Gauss' law $\nabla \cdot F = \nabla \cdot (-\nabla U) = -\Delta U = 0$, so the quadrupole potential will only be equipped with saddle-points, rather than actual minima. This presents an instability to be worked around, most easily by having it oscillate or rotate around the z-axis. This can be achieved by adding an oscillating voltage that has the potential alternate between two states. This results in a time-averaged potential with an effective minimum. A typical depiction describes this potential with a "Pringles shape" as seen in Figure A.5.

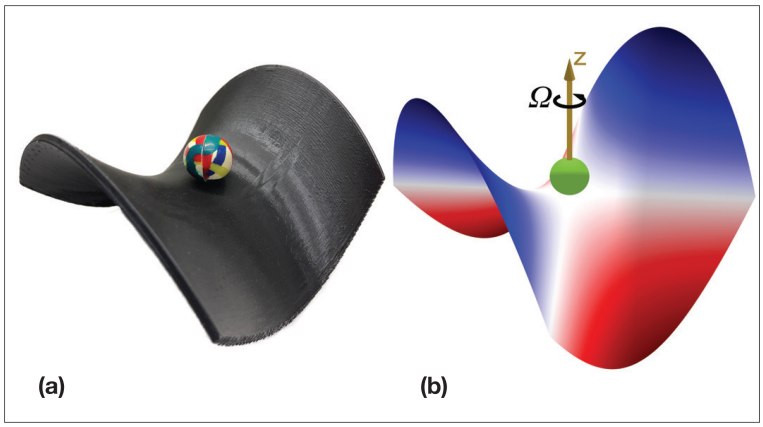

Figure A.5: *A depiction of the potential constructed in the Paul trap, sourced from* **[16]**, *Fig 1. The alternating current spins the potential around the z-axis, creating a relatively stable potential well for particles moving slowly enough. The oscillation frequency for the current directly competes with ambient acceleration. In contrast to the Penning trap, the size of the potential is also a direct effect of the applied fields, while the Penning trap's confinement is only dependent on the ratio between particle mass and charge. As a result, once the particle escapes the potential of a Paul trap, it is effectively lost. For the Penning trap, there is no effective potential that can be escaped, because of the particle velocity forcing it onto the cyclotronic trajectory which is the main mechanism of the confinement.*

As for the Penning trap, the typical Paul Trap setup consists of three electrodes, arranged in a line along the z-axis, and built rotationally symmetrical. The top and bottom electrodes are end-cap hyperbolic electrodes, the same distance away from the ring electrode oriented in the x-y plane between them (Figure A.6).

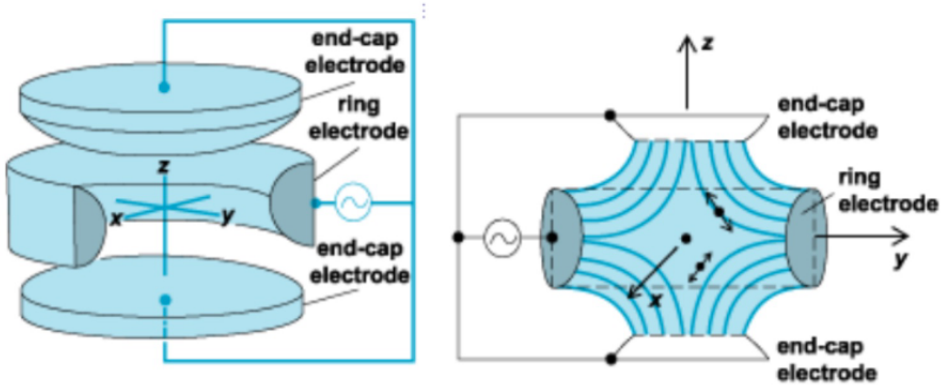

Figure A.6: *An image of Paul Trap electrodes as shown in [**19**], Figure 2*

Theoretically, a quadrupole potential produced by the electrodes has the form $U(r) = Q\phi = Q\frac{\phi_0}{2r_0^2}(ax^2 + by^2 + cz^2)$ where ϕ is Laplacian r_0 is the ring electrode radius, ϕ_0 is an external potential and Q is the particle charge. A non-trivial constraint emerges, by which $a + b + c = 0$. There is a 2D solution by setting $c = 0$ and $a = -b$, though this requires a construction with four rod electrodes with a hyperbolic surface turned inward, which is also usable as a mass spectrometer. It's not so interesting for our purposes. A 3D solution requires that the hyperbolic end-cap electrodes are dimensioned so that $r_0^2 = 2z_0^2$ where z_0 is the distance between the trap center end the end-cap electrodes. The constraint solutions are myriad, but a simple one would set $a = b, c = -(a + b)$. Setting $a = 1$, $\phi = \frac{\phi_0}{2r_0^2}(x^2 + y^2 - 2z^2)$ and the equation of motion is derived from this relation.

$$\ddot{r} + \frac{e}{mr_0^2}(U - V\cos(\Omega t)r) = 0, r \in \{x, y\}, \tag{A.7}$$

$$\ddot{z} + \frac{e}{mr_0^2}(U - V\cos(\Omega t)z) = 0, \tag{A.8}$$

$$a_z = -2a_r = -\frac{8eU}{mr_0^2\Omega^2}, q_z = -2q_r = -\frac{4eV}{mr_0^2\Omega^2}, \Omega t = 2\xi, \tag{A.9}$$

$$\Rightarrow \frac{d^2r}{d\xi^2} + (a_r - 2q_r\cos(2\xi))r = 0, \tag{A.10}$$

$$\frac{d^2z}{d\xi^2} + (a_z - 2q_z\cos(2\xi))z = 0. \tag{A.11}$$

The results are the Mathieu equations, which have stable and unstable solutions. The stable solution is of primary interest in the construction of the Paul trap.

$$u(\xi) = \alpha_1' \sum_n C_{2n} e^{(2n\pm\beta)i\xi} + \alpha_1'' \sum_n C_{2n} e^{-(2n\pm\beta)i\xi} \tag{A.12}$$

$$= \alpha' \sum_n C_{2n} \cos(2n \pm \beta)\xi + \alpha'' \sum_n C_{2n} \sin(2n \pm \beta)\xi, \tag{A.13}$$

$$\Rightarrow \omega_n t = (2n \pm \beta)\xi = \frac{(2n \pm \beta)\Omega t}{2}, \tag{A.14}$$

$$\Omega t = 2\xi. \tag{A.15}$$

Given the high energy density that provides the background for the monopole crystal droplet, the frequency ω_n, at which the voltage would need to oscillate, is far larger than would be sensible to attempt to construct, given that regular alternating current frequencies commonly move in GHz spectra. Until further development, the application of a Paul trap to confine a monopole crystal is unfeasible. As per the approximation in section 8.2, the lifetime of 10^{-19} s at the most, which would require an alternating current above 10^{20} Hz to make sure the monopole crystal's position is known throughout its lifetime, which is not a reasonable requirement for an experimental setup.

FB Physik: Eidesstattliche Erklärung für Abschlussarbeiten

Folgende Formulierung inkl. Unterschrift ist in Ihre Abschlussarbeit aufzunehmen.

Eidesstattliche Erklärung

Ich versichere, dass ich die ~~Bachelorarbeit~~/Masterarbeit selbstständig angefertigt und keine anderen als die angegebenen Hilfsmittel benutzt habe. Alle Stellen, die dem Wortlaut oder dem Sinn nach anderen Werken entnommen sind, habe ich in jedem einzelnen Fall unter genauer Angabe der Quelle deutlich als Entlehnung kenntlich gemacht. Ich versichere, diese Arbeit nicht bereits in gleicher oder ähnlicher Fassung in einem anderen Prüfungsverfahren eingereicht zu haben.

Sofern im Zuge der Erstellung der vorliegenden ~~Bachelorarbeit~~/Masterarbeit generative Künstliche Intelligenz (gKI) basierte elektronische Hilfsmittel verwendet wurden, versichere ich, dass meine eigene Leistung im Vordergrund stand und dass eine vollständige Dokumentation aller verwendeten Hilfsmittel gemäß der Guten wissenschaftlichen Praxis vorliegt. Ich trage die Verantwortung für eventuell durch die gKI generierte fehlerhafte oder verzerrte Inhalte, fehlerhafte Referenzen, Verstöße gegen das Datenschutz- und Urheberrecht oder Plagiate.

Ich bin damit/~~nicht damit~~* einverstanden, dass die ~~Bachelorarbeit~~/Masterarbeit* veröffentlicht wird.

Pinneberg, 30.11.25 [signature]

Ort, Datum Unterschrift

*nicht Zutreffendes streichen bzw. weglassen.

Physics Department: Affidavit for final theses

The following formulation including signature must be included in your thesis.

Statutory Declaration

I declare that I have authored the ~~Bachelor's~~/Master's thesis independently and have not used any aids other than those specified. I have clearly labelled all passages that are taken from other works in terms of wording or meaning as borrowed material, stating the exact source in each case. I confirm that I have not already submitted this thesis in the same or a similar version in another examination procedure.

If electronic aids based on generative artificial intelligence (gAI) were used in the course of the preparation of this ~~Bachelor's/~~Master's thesis, I confirm that my own work was the main focus and that complete documentation of all aids used is available in accordance with good scientific practice. I am responsible for any incorrect or distorted content, incorrect references, violations of data protection and copyright law or plagiarism generated by the gAI.

I agree/~~disagree~~* that the ~~Bachelor's~~/Master's thesis* may be published.

Münster, 30.11.25 _____

Place, date Signature

*Delete or omit as appropriate.